UNIVERSITÀ DEGLI STUDI DI PADOVA

DIPARTIMENTO DI INGEGNERIA DELL'INFORMAZIONE

MASTER THESIS IN ICT FOR INTERNET AND MULTIMEDIA

Optical Characterization and Analysis of Disordered Materials Based on Hollow Silicon Dioxide Microparticles for Passive Daytime Radiative Cooling

MASTER CANDIDATE

Sara Levorin

Student ID 2096409

SUPERVISOR

Prof. Maria-Guglielmina Pelizzo

University of Padova

CO-SUPERVISOR

Dr. Giuseppe Emanuele Lio

University of Florence

ACADEMIC YEAR
2023/2024

Abstract

Passive Daytime Radiative Cooling is an innovative sustainable technique that utilizes the principles of thermal radiation to achieve cooling without active energy consumption. Radiative Cooling (RC) devices exploit high reflectance of solar radiation and strong emission of longwave infrared thermal radiation through the atmospheric window ($8 - 13\mu$m), allowing the creation and design of surfaces able to achieve sub-ambient temperatures by passively dissipating excess heat into the cold sky, even under daylight conditions. This thesis investigates the optical properties and thermal performances of potential RC materials, focusing on disordered materials composed of hollow silicon dioxide (SiO_2) microparticles. The unique morphology of hollow SiO_2 microparticles provides peculiar scattering and emissivity characteristics, making them ideal candidates for enhancing PDRC efficiency. This research links material science, optics, and sustainability, offering an interesting and promising future for energy-efficient cooling solutions.

Sommario

Il raffreddamento radiativo passivo diurno (PDRC) è una tecnica innovativa e sostenibile che utilizza i principi della radiazione termica per ottenere un raffreddamento senza consumo di energia attiva. Il PDRC sfrutta l'elevata riflettanza della radiazione solare e la forte emissione di radiazione termica infrarossa a onde lunghe attraverso la finestra atmosferica ($8-13\mu$m), consentendo di creare e progettare superfici in grado di raggiungere temperature sub-ambientali dissipando passivamente il calore in eccesso nel cielo, anche in condizioni di luce diurna. Questa tesi indaga le proprietà ottiche e le prestazioni termiche di potenziali materiali PRC, concentrandosi su materiali disordinati composti da microparticelle cave di silica (SiO_2). La morfologia unica delle microparticelle cave di silica fornisce caratteristiche peculiari di diffusione ed emissività, rendendole candidate ideali per migliorare l'efficienza delle superfici radiative. Questa ricerca collega scienza dei materiali, ottica e sostenibilità, offrendo una prospettiva interessante e promettente per soluzioni di raffreddamento ad alta efficienza energetica.

Contents

List of Figures

xiv

List of Tables

List of Acronyms

RC Radiative Cooling

PDRC Passive Daytime Radiative Cooler

PRC Passive Radiative Cooling

UV Ultraviolet

UV-Vis Ultraviolet - Visible

NIR Near Infrared Region

IR Infrared Region

MIR Mid-Infrared Region

LWIR Long Wave Infrared

EM Electromagnetic

RC Radiative Cooling

H_2O Water

O_2 Oxygen

O_3 Ozone

CO_2 Carbon Dioxide

N_2 Nitrogen

Ar Argon

ASTM American Society for Testing and Materials

LIST OF TABLES

AM Air Mass

Si Silicon

TIR Total Internal Reflection

Al Aluminum

SiO$_2$ Silicon Dioxide

TiO$_2$ Titanium Dioxide

Al$_2$O$_3$ Aluminum Oxide

VO$_2$ Vanadium Dioxide

W Tungsten

Ag Silver

BaF$_2$ Barium Fluoride

PDMS Polydimethylsiloxane

SiC Silicon Carbide

Si$_3$N$_4$ Silicon Nitride

BN Boron Nitride

CaCO$_3$ Calcium Carbonate

BaSO$_4$ Barium Sulfate

PVDF-HFP PolyVinyliDene Fluoride-HexaFluoroPropylene

ZnO Zinc Oxide

VOCs Volatile Organic Compounds

NPF Nanoporous film

PP polypropylene

PE polyethylene

DRA Diffuse Reflectance Accessory

PMT Photo Multiplier Tube

InGaAs Indium Gallium Arsenide

FTIR Fourier-Transform Infrared Spectroscopy

ATR Attenuated Total Reflectance

Au gold

TE Transverse Electric

NTC Negative Temperature Coefficient

PID Proportional Integral Derivative

PVD Physical Vapour Deposition

PVC Polyvinyl chloride

NA Numerical Aperture

LED Light Emitting Diode

AFM Atomic Force Microscope

EPS Expanded Polystyrene

1

Introduction

The global energy demand has been dramatically increasing over the past years. Specifically, the energy demand for cooling and air conditioning is the one experiencing one of the fastest-growing energy consumption worldwide [1]. This is linked to the current climate crisis, population growth, industrial development, and the improvement of living standards in the developing economies.

The current technology for indoor heating, ventilation, and air conditioning (HVAC) are based on vapour compression techniques. These cooling methods accounts for $\sim$ 15% of the electrical consumption worldwide and to $\sim$ 10% of the greenhouse gas emission worldwide. Residential cooling is expected to increase up to 35% and to 61% by 2050 and 2100 [2], [3]. In fact, the stronger demand for cooling imposes further energy production, hence more fossil resources have to be consumed [4]. In addition, the use of refrigerants for cooling worsen even more the global warming effect. From 1990 to 2022 the Carbon Dioxide (CO_2) emissions due to space cooling has more than tripled, with significant implications for electricity grids and urban heat islands [5].

The growing awareness of the situation pushed the research and development of energy-efficient and environmentally friendly cooling technologies. Moreover, there are lots of initiatives that try to aid countries to find alternative and more sustainable solutions. Indeed, a number of European nations have actually pledged to achieve *net-zero emission* by 2050, aiming to make Europe the first climate-neutral continent. This includes tightening energy efficiency standards for buildings, promoting sustainable cooling techniques, and encourage the clean production of electric power.

1

To mitigate this huge environmental impact, the International Energy Agency promotes several alternatives to the standard ones adopted for cooling. Namely,
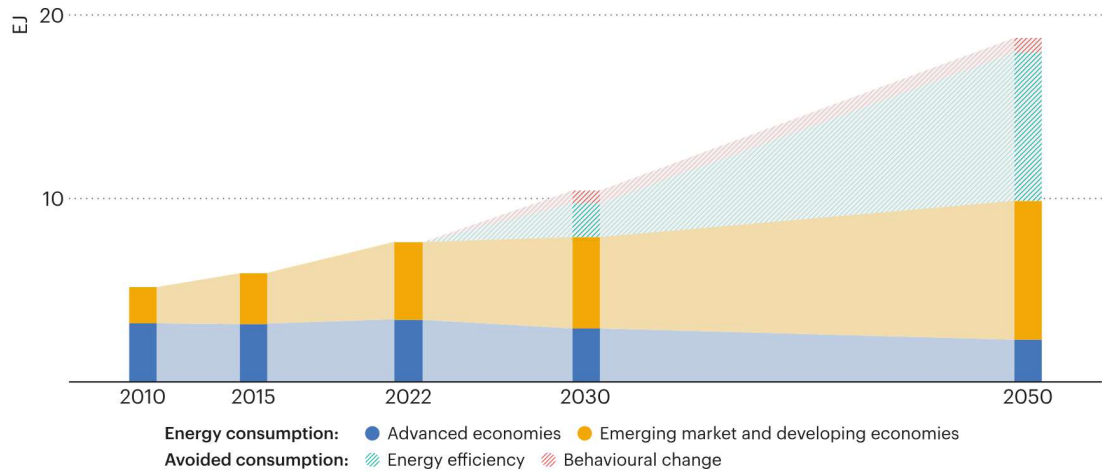
Figure 1.1: Space cooling energy consumption [1].

a passive cooling technique could make a huge impact on the energy menage and greenhouse gases production. Here Passive Radiative Cooling comes into play: based on physical principles intrinsic to any existing body, it can reduce buildings energy consumption for heat dissipation [6]. Passive radiative cooling for buildings focuses on the study and optimization of materials and designs for achieving a natural heat dissipation.

In this thesis lots of different RC architectures are presented, focusing then on a specific RC candidate that offers a solution that is both efficient and cost-effective. This work focuses on the combination of photonic disordered media and polymeric photonics for realizing Passive Daytime Radiative Cooler (PDRC) on a large scale. This solution exploits the combination of commercially available products, starting from a coating basis and then mixing different nano or microparticles.

This project was a collaboration between the University of Florence and the University of Padova. The optical and morphological characterization were performed in CNR-IFN LUXOR laboratory in Padova, whereas the samples preparation and the experimental measurements for evaluating the cooling performances were performed at the physics department at the University of Florence.

The thesis is organized as follows:

- **Chapter 1**: introduction.

- **Chapter 2**: the fundamentals of thermal radiation are presented, focusing then on the principles of radiometry.

- **Chapter 3**: it reports different ways in which cooling can be achieved, focusing on passive RC, its principles and performances measurement.

- **Chapter 4**: it gives deeper insights on the materials employed for PDRC surfaces realization. Paying specific attention to the principles and engineering of disordered photonic media as RC candidates.

- **Chapter 5**: it is dedicated to the presentation and description of the instruments and operational procedures employed for the experimental analysis of PDRC samples.

- **Chapter 6**: it reports all the experimental results obtained.

- **Chapter 7**: conclusions.

2

Fundamentals of thermal radiation

The study of light-matter interaction plays a crucial role in understanding the behaviour of both light and matter at macroscopic and microscopic levels. Such interaction plays a pivotal role in the field of photonics but it has also an interdisciplinary importance in other realms of science. The general understanding of such phenomena starts with with Maxwell's studies on the behaviour of light, then it was further developed by Einstein and culminating with the evolution of quantum theory starting with Max Planck [7].

Based on these foundational studies, both on electromagnetism and quantum mechanics, one of the most intriguing aspects of light is its wave-particle duality: light exhibits properties of both waves and particles, depending on the experimental context. Wave-particle duality has a central role to quantum mechanics and has deeply influenced the understanding of light-matter interactions, enriching the understanding of the microscopic world.

For achieving an adequate comprehension of radiative cooling mechanisms, both theories are fundamental. In this section the basis and the mathematical formulations required to grasp the functioning of such perocess are provided.

2.1 THERMAL RADIATION AND BLACKBODY

2.1.1 INTERACTIONS OF PHOTONS WITH MATTER

ENERGY LEVELS AND THEIR OCCUPATION

In general, the constituents of matter are always subject to thermal excitations, meaning that due to light absorption and/or emission, they are continuously moving among different energy levels, undergoing allowed transitions. Let's deepen on the energy levels distribution of matter, which exist as isolated atoms or interacting with other atoms creating molecules and solids. The dynamic of each of these non-relativistic particles of mass m is described by the *Schrödinger equation*

$$-\frac{\hbar^2}{2m}\nabla^2\Psi(\vec{r},t) + \mathbf{V}(\vec{r},t)\cdot\Psi(\vec{r},t) = -j\hbar\frac{\partial\Psi(\vec{r},t)}{\partial t} \tag{2.1}$$

where each non relativistic particle is subject to a potential $\mathbf{V}(\vec{r},t)$ and the actual behaviour of such particle is governed by the complex wavefunction $\Psi(\vec{r},t)$. For the specific scenario, of time independence of the potential, the energy levels E are obtained as the eigenvalues of the time independent *Schrödinger equation* (Appendix (7))

$$-\frac{\hbar^2}{2m}\nabla^2\psi(\vec{r}) + \mathbf{V}(\vec{r})\cdot\psi(\vec{r}) = E\cdot\psi(\vec{r}) \tag{2.2}$$

the levels may be discrete, as in the case of atoms, just specific energy levels are allowed, or appear as densely packed set of energy levels called bands, as for semiconductors. In this case the bands are called valence band, conduction band and they are divided by a range of forbidden frequencies called energy bandgap [8], [7].

As previously mentioned, each atom of a collection continuously undergoes random transitions among different energetic levels. The latter are described by the rules of statistical physics: the Boltzmann energy distribution yields the probability of finding an atom in the energy level E_m when the system is in equilibrium conditions at temperature T

$$P(E_m) \propto exp(-E_m/k_B T), \qquad m = 1, 2, 3, ... \tag{2.3}$$

with $k_B = 1.380649 \times 10^{-23}$J/K the Boltzmann constant and the coefficient of

proportionality is chosen so that $\sum_m P(E_m) = 1$. Considering (2.3) distribution
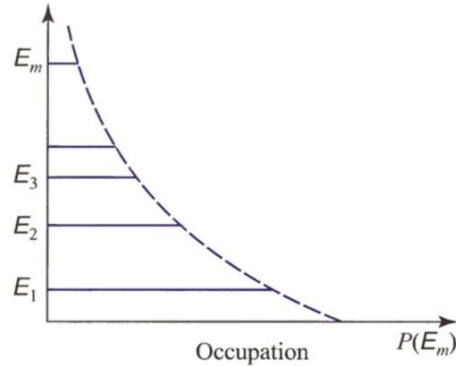
Figure 2.1: Boltzmann probability distribution exponentially decreasing as a function of E_m [7].

for a large number of atoms N and given N_m the number of atoms at energetic level E_m, then it holds that $N_m/N \approx P(E_m)$. Therefore, taking into consideration just two energy levels E_1 and E_2, with number of atoms N_1 and N_2, respectively, the population ratio is

$$\frac{N_2}{N_1} = \frac{g_2}{g_1} \cdot exp\left(-\frac{E_2 - E_1}{k_B T}\right) \tag{2.4}$$

with g_1 and g_2 are the degeneracy parameters, expressing the number of states corresponding to the population levels E_1 and E_2, respectively.
Equation (2.4) expresses the population average of a two level system. Then, one can deduce that in a more general scenario, under steady state conditions, the population at lower energetic level is always larger than the one at higher energetic level [7].

Physical Processes and Thermal Light

In this context, i.e. considering for simplicity a two levels system and an atom-photon interaction of a specific mode of frequency v_0 and energy $hv_0 = E_2 - E_1$, the physical processes initiating transitions among different energetic levels can be categorized as

- **Stimulated emission** an atom in a higher energy level passes to a lower one, under the influence of a photon with just the right frequency, so that the energy in excess will be released as a stimulated photon with the same

energy, phase and polarization of the stimulating one. This will result in *coherent radiation* and given n the mean number of photons per mode in the cavity, the probability density that the atom emits an additional photon is

$$P_{st} = n\frac{c}{V}\sigma(v) \tag{2.5}$$

with V the volume of an optical resonator where a certain number of modes live and $\sigma(v)$ is called *transition cross section*. The latter is a function centered in the resonance atomic frequency v_0.

- **Absorption** the atom passes form a lower to a higher energetic level by absorbing a photon whose energy matches exactly the energy difference of the two levels. The probability density that the atom absorbs one photon from a mode with a mean photon number n is

$$P_{ab} = n\frac{c}{V}\sigma(v) \tag{2.6}$$

- **Spontaneous emission** an atom passes spontaneously from a higher to a lower energy level. The energy difference hv between the two levels is released as a photon with random emission pattern, resulting in incoherent radiation. The probability density of spontaneous emission of a photon into a specific mode v is

$$p_{sp} = \frac{c}{V}\sigma(v) \tag{2.7}$$
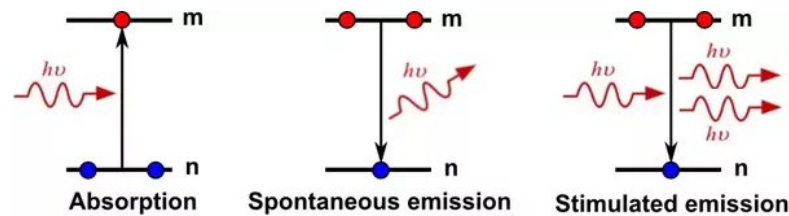
Figure 2.2: Physical processes of absorption, spontaneous emission and stimulated emission [9].

Since the total probability of absorption P_{ab} and stimulated emission P_{st} are the same, such probabilities will be both expressed with the quantity W_i. Moreover, the probability of spontaneous emission into *all* the modes is given by the probability of spontaneous emission (2.7) weighted by the modal density $M(v)$ for a 3D dimensional cavity (Appendix: (7)), then by defying the average cross section $\sigma^*(v)$, the total spontaneous emission probability is

$$P_{sp} = \int_0^\infty \left(\frac{c}{V}\sigma^*(v)\right)(VM(v))\,dv = \frac{8\pi S^*}{\lambda^2} \tag{2.8}$$

Finally, the *spontaneous lifetime* gets defined such that $1/t_{sp} \equiv P_{sp} = M(v_0)cS^*$,

therefore the spontaneous emission of *one* photon into *any* mode is

$$P_{sp} = \frac{1}{t_{sp}} \qquad (2.9)$$

Under conditions of thermal equilibrium and assuming that the atoms interacted with broadband radiation spectral energy density $\rho(v)$, radiation, known as *thermal light*, is emitted from any body. The latter is an electromagnetic radiation emitted from all matter that is at non-zero temperature in the wavelength range from 0.1 to $100\mu m$. Its properties are expressed via a macroscopic rate-equation by taking into account the three physical processes previously presented.

Let's take into account a 3D resonant cavity of unitary volume at temperature T, whose atoms have two energetic levels separated by an energy difference hv and it supports multimode polychromatic light. Let $N_1(t)$ and $N_2(t)$ the mean number of atoms per unit volume occupying respectively energy level 1 and 2 at time t. The three physical processes of *spontaneous emission*, *stimulated emission* and *absorption* coexist inside the cavity yielding the *rate equation*

$$\frac{dN_2}{dt} = -\frac{N_2}{t_{sp}} + n^* \frac{N_1}{t_{sp}} - n^* \frac{N_2}{t_{sp}} \qquad (2.10)$$

Moreover, the assumption of thermal equilibrium imposes that the number of atoms at level 2 in time stays constant, i.e. $dN_2/dt = 0$. Combining this with the statistical description of atomic population distribution given by Boltzmann (2.3), one can obtain

$$\frac{N_2}{N_1} = \frac{n^*}{1+n^*} = exp\left(-\frac{E_2 - E_1}{k_B T}\right) = exp\left(-\frac{hv}{k_B T}\right) \qquad (2.11)$$

Finally, the mean number of photons per mode of the cavity close to frequency v is obtained

$$n^* = \frac{1}{exp(hv/k_B T) - 1} \qquad (2.12)$$

2.1.2 THE BLACKBODY

Any body at temperature T emits electromagnetic radiation, yielding a spectrum that appears continuous. The features of the latter depend only on the reflective and absorbing properties of the body. When considering an idealized counterpart of the latter, one refers to a blackbody and it has the following properties

- It completely absorbs the incoming electromagnetic radiation at any wavelength and at any angle of incidence

- The emitted radiation is completely independent from any factor concerning the shape and composition of the blackbody

In other words, the definition of the blackbody as a perfect absorber, implies that it is also a perfect emitter, i.e. no body at the same temperature can emit more at any wavelength and into any direction. Moreover, experimentally one can show that the emitted radiation *only* depends on temperature T and not on any other parameters, such as shape, size and nature of the material.
The blackbody consists of a cavity, at temperature T, with a small hole where the radiation inside is at thermodynamic equilibrium. Its behaviour is described by the two experimental laws, being *Stefan-Boltzmann law*

$$I(T) = \int_0^\infty M_\lambda(\lambda)d\lambda = \sigma T^4 \tag{2.13}$$

and *Wien's law*

$$\lambda_{max}T = 2.8978 \times 10^{-3} \ m \cdot \text{K} \tag{2.14}$$

with $\sigma = 5.67 \times 10^{-8}$ Wm^{-2}K^{-4} the Stefan-Boltzmann constant. Starting from the observation of Equation (2.13), one can conclude that for increasing temperatures T, the irradiance increases and the peak wavelength λ_{max} shifts to shorter ones obeying Equation (2.14) [7], [10].

RAYLEIGH-JEANS LAW AND PLANCK'S LAW

Exploiting the knowledge given by classical physics and Boltzmann statistics, each resonant mode has mean energy

$$\langle E \rangle = k_B \cdot T \tag{2.15}$$

with k_B Boltzmann's constant. Therefore the energy of the whole system (positive octante of the sphere) is given by the multiplication of the average energy of each mode for the number of modes in the system

$$u(v) = M(v) \cdot \langle E \rangle = \frac{8\pi v^2}{c^3} k_B T \tag{2.16}$$

yielding the energy density per unit of frequency per unit of volume, also known as the *Rayleigh-Jeans Law*.

Comparing this result with the experimental output, one can notice that, apart for small frequencies, there is no match between the two behaviours. Classical laws of electromagnetism are not able to explain the behaviour of the blackbody, in fact the spectrum calculated with these models does not match the experimental one. For ultraviolet frequencies the theoretical derived curve rapidly diverges yielding an infinite energy for a finite system. This is called *ultraviolet catastrophe*.

The discovery following the photoelectric effect experiment (A. Einstein, 1905) was necessary for grasping the behaviour of the blackbody spectrum. Such experiment stated that light waves had also particle properties and that each light quanta had a specific energy [8].

Starting form this discovery, Planck later on proposed a quantisation of the cavity modes, assuming that the only certain energies multiple of a fundamental unit are valid

$$\langle E \rangle = n \cdot hv \tag{2.17}$$

with $n = 1, 2, 3, ...$

Knowing that the mean number of photons per mode at frequency v is expressed by Equation (2.12), one can retrieve the average energy for a radiation mode

$$\langle E \rangle = n^* \cdot hv = \frac{hv}{exp(hv/k_B T) - 1} \tag{2.18}$$

Under the light of this new hypothesis, solving Helmholtz equation inside a 3D box and exploiting $M(v)$ (Appendix: (7)) and imposing that the new mathematical expression has to coincide with (2.16) for low frequencies, then *Planck's law* is obtained

$$\rho(v) = M(v) \cdot \langle E \rangle = \frac{8\pi v^2}{c^3} \frac{hv}{exp(hv/k_B T) - 1} \quad [W m^{-2} \mu m^{-1}] \tag{2.19}$$

11

expressing the spectral energy density per unit of volume per unit of bandwidth, also known as the blackbody radiation spectrum.

In the classical limit for small frequencies, i.e. in the limit of small photon energy $h\nu << k_B T$, one can expand $h\nu/k_B T$ with Taylor $exp(h\nu/k_B T) - 1 \approx 1 + h\nu/k_B T + ... - 1$. Hence, $exp(h\nu/k_B T) - 1 = h\nu/k_B T$ and by replacing this in $\rho(\nu)$, *Rayleigh-Jeans formula* (2.16) is obtained.
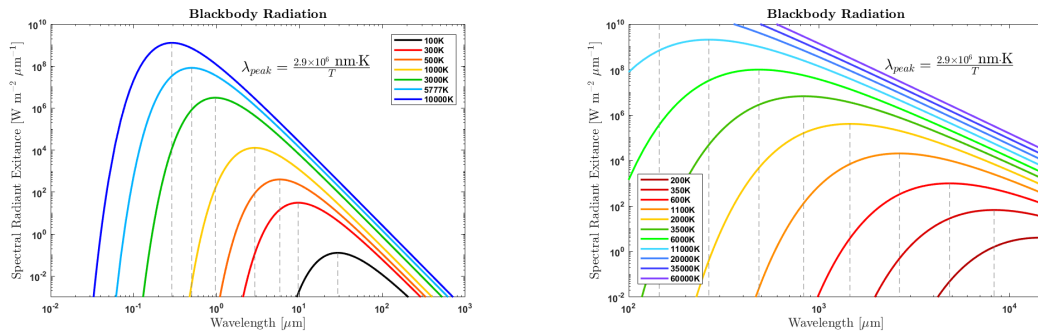
Figure 2.3: Blackbody radiation $\rho(\nu)$ on frequency in double-logarithmic coordinates for different temperatures T [11].
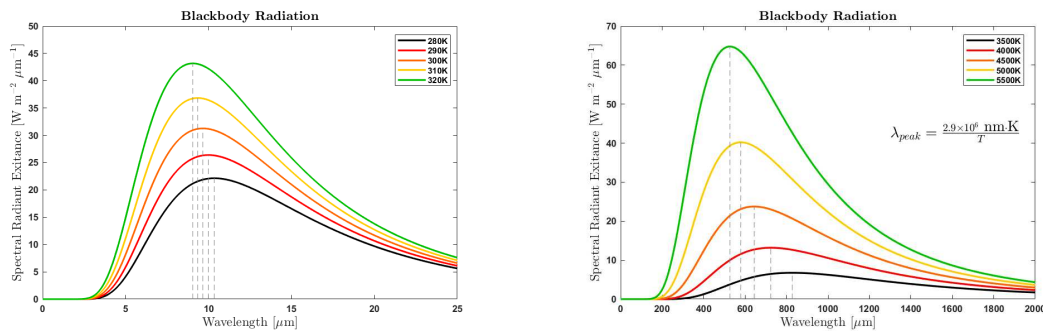
Figure 2.4: Blackbody radiation $\rho(\nu)$ on frequency in linear scale for different temperatures T [11].

By observing the experimental behaviour of the blackbody reported in Figures (2.3) and (2.4), one can confirm that the only parameter affecting the spectral composition of the blackbody radiation, is actually temperature T. As also stated by *Stefan-Boltzmann Law*, experiments state that the energy radiated by the body is directly proportional to temperature.

2.2 Fundamentals of Radiation in Absorbing and Emitting Media

2.2.1 Spectral Radiometry

Radiometry measures the energy or power of electromagnetic radiation, including the optical part of the spectrum, for a given geometry of propagation. Radiometric quantities can change across the electromagnetic spectrum, for this reason the following quantites will be expressed as function of the wavelength λ. For evaluating the behaviour of a system over a specific bandwidth, one has to take the integral of the interested quantity over the deemed wavelength range

$$A = \int_{\lambda_1}^{\lambda_2} a(\lambda)d\lambda \tag{2.20}$$

Hereinafter the fundamentals quantities in spectral radiometry are presented [12], after having introduced some essential geometrical concepts helping to the description of an accurate model for the radiative heat transfer scenario.

Solid Angle and *Foreshortening*

A *solid angle* is the 2D equivalent of a linear angle. It is expressed by the ratio between the elemental area dA of a spherical shell from a spherical center point of view and the square of the radius r of the sphere

$$d\bar{\omega} = \frac{dA}{r^2} \ [sr] \tag{2.21}$$

Solid angles are measured in *steradians* ($[sr]$): one steradian is defined as the solid angle subtended at the center of the sphere of radius one by a unit area on its surface. By construction, any closed surface of any shape subtends the maximum solid angle which is $\Omega = 4\pi$.

If the normal of the area dA is not parallel to the sphere radius, for the calculation of the subtended solid angle, one has to take into account the *foreshortening*. The latter consists in the reduction in the area of the surface seen from a specific point of view. Hence, let θ be the displacement between the normal to the surface and the radius of the sphere laying along just one direction, the projected

solid angle gets calculated as

$$\bar{\omega} = \frac{dA \cdot cos\theta}{r^2} \quad [sr] \tag{2.22}$$

moreover, if the tilt is bi-dimensional, the solid angle has to be computed considering the product of the cosines.

One can notice that the involved area is maximum when the radius and the normal to the surface are parallel and then it decreases until, at the limit, the projected area collapses in a line. From a physical point of view, considering a non-uniform directional radiation, the transferred power will be maximum only when the projected area perfectly coincides with the emitting surface.
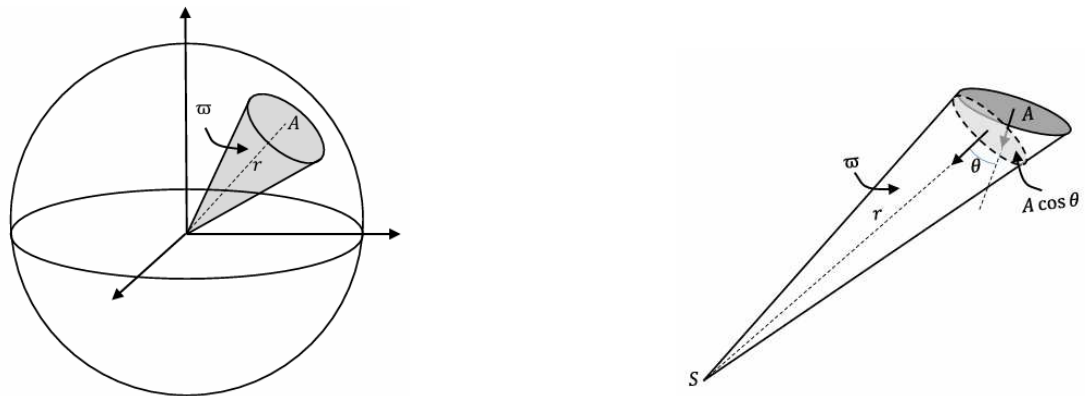
Figure 2.5: Solid angle and projected solid angle [9].

SPHERICAL COORDINATES SYSTEM

For a good representation of the heat transfer model, it is necessary to employ the *spherical coordinate system*. This system determines the position of a point in a 3D space based on a triplet of numbers: the distance of the latter from the origin r, the polar angle θ and the azimuthal angle ϕ. The polar angle is defined as the displacement between the radial line connecting the point to the origin of the reference system and the zenith, whereas the azimuthal angle ϕ is defined between the projection of the radial line on the xy plane and the positive x axis [13].

When setting up a model for heat transfer, two surfaces have to be individualized: one surface that emits the radiation, i.e. *giver*, and one that intercepts it, i.e. *taker*. To evaluate the power emitted by the giver, one has to rescale the total power emitted by the blackbody with the portion of area intercepting the radia-

tion. Then let's define the infinitesimal emitting area dA_1 and the infinitesimal receiving area dA_n, then the solid angle is defined as the angle subtended by the area dA_n at a point laying on dA_1. The position of dA_n with respect to dA_1 is defined by the spherical coordinates triplet (r, θ, ϕ) and the area is yielded by making infinitesimal adjustments to the two angles $d\theta$ and $d\phi$

$$dA_n = rsin\theta d\phi rd\theta \tag{2.23}$$

therefore the solid angle from Equation (2.21) becomes

$$d\bar{\omega} = \frac{dA_n}{r^2} = \frac{r^2 sin\theta d\phi d\theta}{r^2} = sin\theta d\phi d\theta \tag{2.24}$$

Since the focus is on the radiation emitted from a finite surface, one takes into consideration only the hemisphere above the emitting surface. Hence, the solid angle calculated for such hemisphere is

$$\bar{\Omega} = \int d\bar{\omega} = \int_0^{2\pi} \int_0^{\frac{\pi}{2}} sin\theta d\theta d\phi = 2\pi \ cos\theta|_0^{\pi/2} = 2\pi \ [sr] \tag{2.25}$$
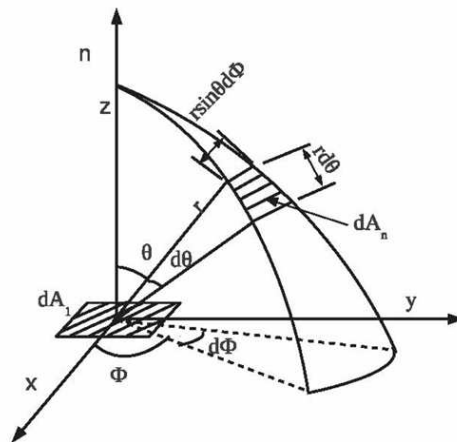
Figure 2.6: Solid angle subtended by the intercepting area related to the emitting area in spherical coordinates [14].

Spectral Radiant Power $\Phi_{e,\lambda}$

Let's define dQ_e the total energy of electromagnetic radiation that gets either emitted, received or reflected. Then the *spectral radiant power* (or spectral radiant flux) is defined as the total energy dQ_e per unit of time

$$\Phi_{e,\lambda} = \frac{dQ_e}{dt d\lambda} \ [Wm^{-1}] \tag{2.26}$$

Spectral Radiant Intensity $I_{e,\lambda}$

The electromagnetic power either emitted, received or reflected per unit of solid angle is called *spectral radiant intensity* and is defined as

$$I_{e,\lambda} = \frac{d\Phi_{e,\lambda}}{d\bar{\omega} d\lambda} \ [Wsr^{-1}m^{-1}] \tag{2.27}$$

Let's observe that such quantity highly depends on the direction and orientation of the electromagnetic source. In the specific case of an isotropic source and uniform omnidirectional emission, the total radiant power is

$$\Phi_{e,\lambda} = 4\pi \cdot I_{e,\lambda} \tag{2.28}$$

where the equivalence has been provided using the calculations performed in Section (2.2.1).

Spectral Radiant flux density M_λ **or** $E_{e,\lambda}$

The *radiant flux density* at a surface can be distinguished depending on the different point of view, then it takes the name of

- *Spectral Radiant exitance* M_λ when the electromagnetic radiation gets emitted from a surface
- *Spectral Irradiance* $E_{e,\lambda}$ when the radiation gets received by a surface

Concentrating on *spectral irradiance* for the sake of simplicity (a similar reasoning holds also for spectral radiant exitance), the received power per unit of area is

$$E_{e,\lambda} = \frac{d\Phi_{e,\lambda}}{dA d\lambda} \ [Wm^{-2}m^{-1}] \tag{2.29}$$

Let's consider an infinitesimal area dA at a certain distance r from the point source S. The latter is an isotropic source and the radiant power intercepted by

the elemental area is

$$d\Phi_{e,\lambda} = I_{e,\lambda}d\bar{\omega} \tag{2.30}$$

where $d\bar{\omega} = (dAcos\theta)/r^2$ is the underlying infinitesimal angle to the source with projected area $dAcos\theta$ and θ the angle between the surface normal of the surface and the direction from S to the area. Then the irradiance is

$$E_{e,\lambda} = \frac{d\Phi_{e,\lambda}}{dAd\lambda} = \frac{I_{e,\lambda}}{r^2}cos\theta \tag{2.31}$$

SPECTRAL RADIANCE $L_{e,\lambda}$

The radiation emitted by an *extended* source, may be referred to as *radiance*. The latter is, as well as the radiant intensity, a function of the observation direction defined by the solid angle $\bar{\omega}$. Hence, the spectral radiance, also known as spectral radiation intensity, gets defined as the radiant intensity emitted by an extended source per unit of foreshortened area per unit of solid angle in a given direction

$$L_{e,\lambda} = \frac{dI_{e,\lambda}}{d\lambda dAcos\theta} = \frac{d^2\Phi_{e,\lambda}}{d\lambda d\bar{\omega}dAcos\theta} \ [Wsr^{-1}m^{-2}m^{-1}] \tag{2.32}$$

This equation can also be expressed in terms of *radiant energy*, so that the measured quantity is the total energy, per unit of area, per unit of solid angle, per unit of wavelength. In general, the dependency on time is omitted in the representation, then

$$L_{e,\lambda} = \frac{d^2Q_{e,\lambda}}{d\lambda d\bar{\omega}dAcos\theta} \ [Wsr^{-1}m^{-2}m^{-1}] \tag{2.33}$$

Finally, let's notice that all these quantities, apart depending on the wavelength λ, they also depend on the direction of the outgoing or incoming radiation with respect to the *giver* and *taker* surface. Therefore such dependency will be shown by writing the quantity as function of the spherical coordinates θ and ϕ. For instance, the spectral radiation intensity is $L_{e,\lambda}$ gets expressed as $L_{e,\lambda}(\lambda, \theta, \phi)$. Moreover, let's notice that any of these quantities is deeply linked to the temperature T of the body, still for the sake of simplicity, the dependency to the temperature is not explicated in the parameters function of the spectral radiometric quantity, since it is assumed to be already taken into account in the energy term dQ_e [14].

Moreover, for all these quantities, when talking about incoming radiation, one can referred about the incident radiated power with different nature: it can be reflected, transmitted or emitted.

2.3 THERMAL PROPERTIES OF GRAY BODIES

As introduced at the beginning of Section (2.1.2), the blackbody was presented as the ideal counterpart of a real body. In fact, any body at a given temperature T emits electromagnetic radiation, but there does not exist a body neither absorbing nor emitting like a blackbody. The radiative properties and spectrum features of a real body depend on the reflective and absorbing properties of the materials, on the type of surfaces constituting the body, on the temperature of the body , the spectral composition of the impinging radiation and the angle of emission. Hereinafter, after having introduced some quantitative definitions for the blackbody, one can finally define some parameters that will quantify how different the behaviour of a real body is from the one of a blackbody.

2.3.1 FUNDAMENTALS OF ELECTROMAGNETIC WAVE PROPAGATION

To provide a comprehensive quantitative description of the blackbody behaviour and facilitate the comparisons with other body's behaviours, a brief introduction to electromagnetic wave propagation is presented. Numerical analysis is achieved via optical parameters of *reflectivity* ρ, *trasmissivity* τ and *absorptivity* α.

Maxwell's Equations are a set of four equations constituting the foundations for explaining the relation between electric **E** and magnetic field **B**. They are at the same time necessary and sufficient for describing electromagnetism, as well as the interaction between radiation and matter. The laws are *Gauss's Law*,

Gauss's Law for Magnetism, *Faraday's Law* and *Maxwell-Ampère's Law*

$$\vec{\nabla} \cdot \mathbf{E} = \frac{\rho}{\epsilon_0} \qquad\qquad \vec{\nabla} \cdot \mathbf{B} = 0 \qquad\qquad (2.34)$$

$$\vec{\nabla} \times \mathbf{E} = -\frac{\partial \mathbf{B}}{\partial t} \qquad\qquad \vec{\nabla} \times \mathbf{B} = \mu_0 \mathbf{J} + \mu_0 \epsilon_0 \frac{\partial \mathbf{E}}{\partial t} \qquad\qquad (2.35)$$

where ρ is the total electric charge density in a point in space, $\epsilon_0 = 8.854 \times 10^{-12}$ $[Fm^{-1}]$ the vacuum permittivity, $\mu_0 = 4\pi \times 10^{-7}$ $[NA^{-2}]$ the vacuum permeability and $\mathbf{J}$ the current density [10].

From these laws, the *wave equations* for the electric and magnetic field are obtained

$$\nabla^2 \mathbf{E} - \frac{1}{c^2} \frac{\partial^2 \mathbf{E}}{\partial t^2} = 0 \qquad\qquad \nabla^2 \mathbf{B} - \frac{1}{c^2} \frac{\partial^2 \mathbf{B}}{\partial t^2} = 0 \qquad\qquad (2.36)$$

with $c = \frac{c_0}{n}$ is the speed of light in a homogeneous transparent medium with refractive index n. Furthermore, $c0 = 1/\sqrt{\epsilon_0 \mu_0}$ the speed of light in vacuum. In general, when an electromagnetic wave travels in a medium, its speed is scaled with the refractive index n of the material which depends on the relative dielectric constant of the medium $\epsilon_r = \epsilon/\epsilon_0$.

One possible solution to the Equation (2.36) is the plane wave solution

$$\mathbf{E}(\mathbf{r}, t) = \mathbf{E_0} e^{i(\mathbf{k} \cdot \mathbf{r} - \omega t)} \qquad\qquad \mathbf{B}(\mathbf{r}, t) = \mathbf{B_0} e^{i(\mathbf{k} \cdot \mathbf{r} - \omega t)} \qquad\qquad (2.37)$$

with $\mathbf{E_0}$ and $\mathbf{B_0}$ constant vectors, $\mathbf{k}$ wave vector whose module (also known as wavenumber) is $|\mathbf{k}| = k = \omega\sqrt{\mu\epsilon} = k_0 n = \frac{\omega n}{c}$.

A fundamental property of electromagnetic waves is *polarization*, which offers a deeper insight in the interaction of the radiation with matter. *Polarization* is the position of the tip of the electric field vector $\mathbf{E}$ in the xy plane, i.e. the plane perpendicular to the propagation axis (z axis), at a position $\mathbf{r}$ at time t [15], [16]. In general, the incoming electromagnetic radiation is naturally unpolarized and any incoming wave can be represented as the superposition of two linearly polarized components on two orthogonal planes. Let's define *incidence plane*, the one where the impinging wave lays, hence the two polarization planes taken into consideration will be the incidence plane, identified with the symbol ∥, and one orthogonal to the latter, identified with ⊥ [10]. Therefore, a general electric

field of a wave is expressed as

$$\mathbf{E} = E_{\parallel}\mathbf{u}_{\parallel} + E_{\perp}\mathbf{u}_{\perp} \tag{2.38}$$

SNELL'S LAW AND FRESNEL'S COEFFICIENTS

When the radiation impinges at an interface, part of it will be reflected, a part transmitted and a part absorbed by the material. These properties are linked to the refractive index n of the material, which in the most general case, is a complex quantity

$$\bar{n} = n - ik \tag{2.39}$$

where k is called *extinction coefficient* and it is responsible for the attenuation of the radiation as it propagates inside the material $\bar{n}$. In addition, this quantity also depends on the wavelength $n(\lambda)$, but this dependence will not be included, as it is beyond the scope of the current discussion.
For a non-absorbing perfect dielctric material, the refractive index is a real quantity ($k = 0$). Then, let's consider the propagation of a plane Electromagnetic (EM) wave in such a medium and assume that the latter impinges on a planar interface between another medium with refractive index n_t and the n_i. The plane wave impinges with an angle θ_i at the interface, then the reflected wave will have a direction defined by the angle θ_r and the refracted wave θ_t
 These angles are related via *Snell's law* for reflection and refraction, stating,
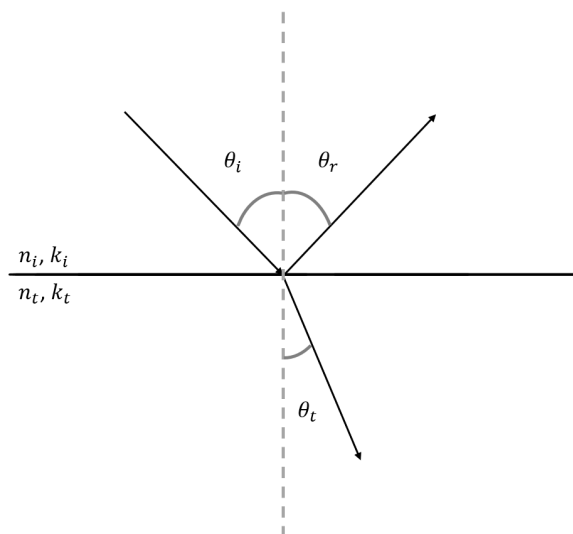
Figure 2.7: Impinging electromagnetic wave at the interface between two media.

20

respectively

$$\theta_i = \theta_r \qquad\qquad sin\theta_i n_i = sin\theta_t n_t \qquad\qquad (2.40)$$

These relations still do not provide any information on how the power of the impinging radiation gets spreaded between reflected, refracted and absorbed. It is necessary to introduce the *Fresnel coefficients* for quantifying such components. Now let's take into consideration the geometry previously described for the presentation of the Snell's law and a generic electric field as in Equation (2.38). Moreover, for any incident EM wave on a surface, Maxwell's equations impose some boundary conditions to be satisfied: in absence of charges ($\rho = 0$) and currents ($\mathbf{J} = 0$) at the interface between the medium n_i and n_t, the parallel components of the electric and magnetic field are continuous at the interface

$$(E_i + E_r)_{\|} = E_{t\|} \qquad\qquad (H_i + H_r)_{\|} = H_{t\|} \qquad\qquad (2.41)$$

Thus, the Fresnel's coefficients necessary for the computation of the reflected and transmitted components of the incoming wave are four: $r_{\|}$, $r_{\perp}$, $t_{\|}$ and $t_{\perp}$. Those quantities can be expressed in different forms depending on the necessity and the scenario in which they are used. Let's report them as functions of just the angle of incidence θ_i and refraction θ_t

$$r_{\|} = -\frac{sin(\theta_i - \theta_t)}{sin(\theta_i + \theta_t)} \qquad\qquad r_{\perp} = \frac{tg(\theta_i - \theta_t)}{tg(\theta_i + \theta_t)} \qquad\qquad (2.42)$$

$$t_{\|} = \frac{2sin\theta_t cos\theta_i}{sin(\theta_i + \theta_t)} \qquad\qquad t_{\perp} = \frac{2sin\theta_t cos\theta_i}{sin(\theta_i + \theta_t)cos(\theta_i - \theta_t)} \qquad\qquad (2.43)$$

SURFACES TOPOGRAPHY

Fresnel's coefficients yield a quantitative description of how light gets partially reflected and refracted at the interface between two media. Still, for a full characterisation of such interaction one has to take into account also the boundary features [12].

- **Specular surface** the directions of the reflected and refracted rays are determined by Snell's Law (2.40)

- **Glossy surface** the reflection is "almost specular": light will be scattered about the ideal specular reflection direction. The spreading of the scattered component is related to the surface properties

- **Diffusive surface** the angle that the direction of the reflected beam forms with the normal to the surface is random and uniformly distributed about the surface normal hemisphere (Rayleigh criterion)
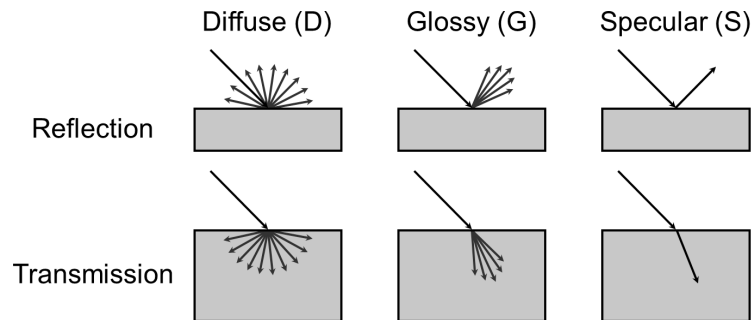
Figure 2.8: Reflection and transmission for diffusive, glossy and specular surfaces.

Let's notice that the Fresnel's coefficients (2.42) are calculated for a perfectly specular surface, therefore they can be directly applied only in this specific scenario. For the other two cases, the calculations for reflectivity and transmissivity get more complicated, since one has to take into account that the interactions are highly surface-dependent.

For completeness, it is right to specify that each of the quantities previously mentioned, i.e. *reflectivity ρ*, *trasmissivity τ*, *absorptivity α* and *emissivity ϵ*, are all functions of the wavelength via the refractive index of the material. Moreover, thanks to the scenario depicted in Section (2.2.1), it is worth it to remark that all these properties depend from their related solid angles, therefore from (θ_i, ϕ_i), (θ_r, ϕ_r), (θ_t, ϕ_t) and (θ_e, ϕ_e), where the latter is the emission angle.
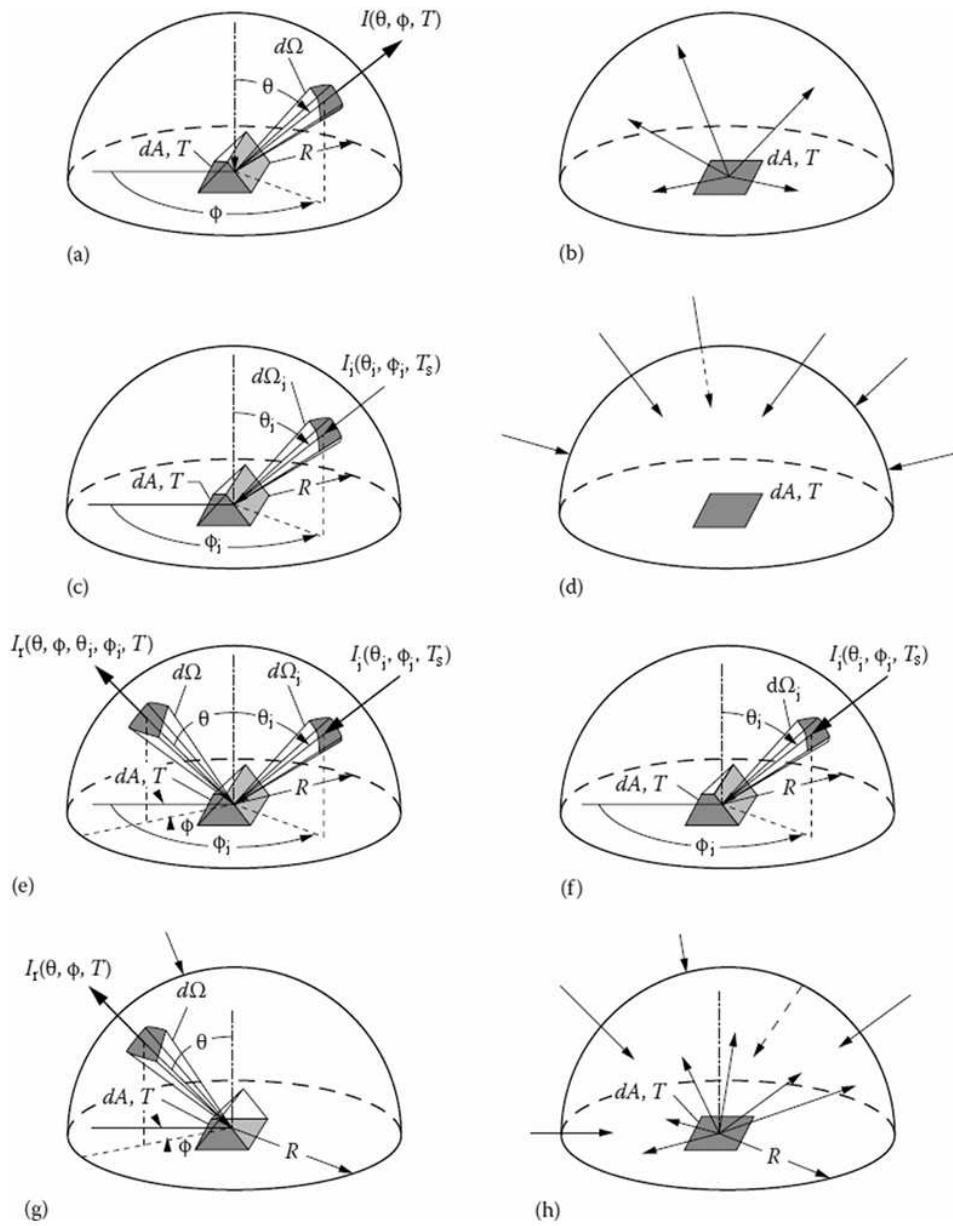
Figure 2.9: Representation of directional and hemispherical radiative properties [16].

Spectral Hemispherical Reflectivity $\rho_\lambda(\lambda, \theta_i, \phi_i)$

In the most basic formulation, the reflectivity is the ratio between the reflected and incident power. For being more precise, after having described the scenario and the necessary parameters for the full understanding of the behaviour of a EM wave at the interface, let's define the *specular* reflectivity of an incident unpolarized plane wave at angle θ_i

$$\rho_{\lambda,s}(\theta_i) = \frac{\rho_{\lambda,s,\|}(\theta_i) + \rho_{\lambda,s,\perp}(\theta_i)}{2} = \frac{1}{2}\left(\frac{tg^2(\theta_i - \theta_t)}{tg^2(\theta_i + \theta_t)} + \frac{sin^2(\theta_i - \theta_t)}{sin^2(\theta_i + \theta_t)}\right) = \quad (2.44)$$

$$= \frac{1}{2}\frac{sin^2(\theta_i - \theta_t)}{sin^2(\theta_i + \theta_t)}\left(1 + \frac{cos^2(\theta_i - \theta_t)}{cos^2(\theta_i + \theta_t)}\right) \quad (2.45)$$

with

$$\rho_{\lambda,s,\|}(\theta_i) = r_\|^2 = \left(-\frac{sin(\theta_i - \theta_t)}{sin(\theta_i + \theta_t)}\right)^2 \quad \rho_{\lambda,s,\perp}(\theta_i) = r_\perp^2 = \left(\frac{tg(\theta_i - \theta_t)}{tg(\theta_i + \theta_t)}\right)^2 \quad (2.46)$$

the reflection coefficients on the two polarization planes $\|$ and $\perp$, respectively. Let's notice that in Equation (2.44) the reflectivity is obtained as the average of two components. This is linked to the fact that the incoming light is unpolarized, therefore the angle that the electric field forms with the incidence polarization plane is equiprobable [10], [16].

Spectral Hemispherical Emissivity $\epsilon_\lambda(\lambda, \theta_e, \phi_e)$

The quantity of *emissivity* ϵ expresses quantitatively how different a real body is from the blackbody at the same temperature T. Usually, the spectral exitance M_λ (2.2.1) of the specimen and the blackbody get compared over various narrow wavelength intervals. Thus, in general, ϵ is not a constant, for this reason the quantity that will be later on introduced is a *spectral* one [9], [16].
Unlike the blackbody that shows an isotropic behaviour for the radiation emission, real bodies emitted radiation depend on the direction. In the radiative cooling scenario, one does not care about the directionality of the emitted radiation, rather, one focuses on the intensity. For this reason the directional spectral emissivity gets averaged by integration over the positive hemispherical envelope over the studied surface.
For making a comparison, one has to calculate the *spectral radiance* $I_{b,\lambda}$ and the

hemispherical spectral emissive power $E_{b,\lambda}$ of the blackbody. Then,

$$E_{b,\lambda}(\lambda, T) = \int_0^{2\pi} \int_0^{\pi/2} L_{b,\lambda}(\lambda, T) cos\theta sin\theta d\theta d\phi = \pi \cdot L_{b,\lambda}(\lambda, T) \qquad (2.47)$$

Let's notice that given the isotropic property of the radiation emitted by the blackbody, the dependency from the solid angle coordinates is omitted. On the other hand, the same reasoning cannot be applied when considering a specimen different from a perfect emitter, which has a spectral radiance defined as $L_\lambda(\lambda, T, \theta, \phi)$

$$E_\lambda(\lambda, T) = \int_0^{2\pi} \int_0^{\pi/2} L_\lambda(\lambda, T, \theta, \phi) cos\theta sin\theta d\theta d\phi = \qquad (2.48)$$

$$= L_{b,\lambda} \int_0^{2\pi} \int_0^{\pi/2} \epsilon_\lambda(\lambda, T, \theta, \phi) cos\theta sin\theta d\theta d\phi \qquad (2.49)$$

where the integrated function $\epsilon_\lambda(\lambda, T, \theta, \phi)$ is the *directional spectral emissivity* which is defined as

$$\epsilon_\lambda(\lambda, T, \theta, \phi) = \frac{L_\lambda(\lambda, T, \theta, \phi)}{L_{b,\lambda}(\lambda, T)} \qquad (2.50)$$

at this point exploiting Equation (2.47)

$$\epsilon_\lambda(\lambda, T) = \frac{1}{\pi} \int_0^{2\pi} \int_0^{\pi/2} \epsilon_\lambda(\lambda, T, \theta, \phi) cos\theta sin\theta d\theta d\phi \qquad (2.51)$$

ABSORPTIVITY

Absorptivity is defined as the ratio between the energy absorbed by the body and the impinging one. This reaction to EM incoming wave is complex to be modelled, as it depends not only on the surface temperature, but also on the direction and wavelength of the incoming radiation [14], [16].
When the radiation impinges on the boundary, it can be reflected, absorbed or transmitted. According to the power conservation, it must hold that

$$P_{incident} = P_{reflected} + P_{transmitted} + P_{absorbed} \qquad (2.52)$$

after having normalized for the incident power $P_{incident}$

$$1 = \rho + \tau + \alpha \qquad (2.53)$$

where the parameters in the equation are the *total* quantities, hence they have being integrated over the whole spectrum of wavelength.

An other simplification that can be made and it matches perfectly with the surfaces that have been employed for studying passive radiative cooling, consists in considering *opaque* surfaces where there is no transmitted radiation, i.e. $\tau = 0$. Then the equation simplifies

$$1 = \rho + \alpha \tag{2.54}$$

Therefore, the absorptivity can be calculated as $\alpha = 1 - \rho$.

Kirchhoff's law

Absorptivity may be defined from a radiative point of view, therfore taking also into account the incident radiation on the object. Exploiting this different definition, *Kirchhoff's Law* has been experimentally verified:

$$\alpha(\lambda, T, \theta_i, \phi_i) = \epsilon(\lambda, T, \theta_i, \phi_i) \tag{2.55}$$

This states that emissivity and absorptivity of an object are equal when the system is in a state of thermal equilibrium.

3

Fundamentals of Passive Radiative Cooling Surfaces

This Chapter covers the fundamentals of Passive Radiative cooling (PRC) surfaces, focusing on the principles, atmospheric transmission, solar spectrum, and the distinction between active and passive cooling performances.

3.1 COOLING TECHNIQUES

3.1.1 ATMOSPHERIC TRANSMISSION

In the evaluation of RC surfaces performances, one has to properly estimate the behaviour related to the emissivity of the radiative cooler. The scope of this section is to introduce a deeply influencing factor in the aforementioned estimation, whereas in Section (3.2) the mathematical model for the surface emission will be presented.

In the design of the RC system, one has to take into consideration that the power that is emitted by the surface, it will be radiated to the outer space, hence being absorbed by the atmosphere. The latter is composed by different gas molecules such as Water (H_2O) vapor, Oxygen (O_2), Ozone (O_3), Nitrogen (N_2), CO_2, Argon (Ar) and, other minor absorbers. The energy exchange between the earth and the outer space gets heavily influenced by their presence. In

fact, those constituents will interact with the incoming solar radiation and will affect it. For instance, O_3 is the main responsible for the absorption of harmful Ultraviolet (UV) radiation, whereas H_2O absorbs specific wavelengths in the IR region of the spectrum.

The primary focus in RC studies is the atmospheric transmission windows,
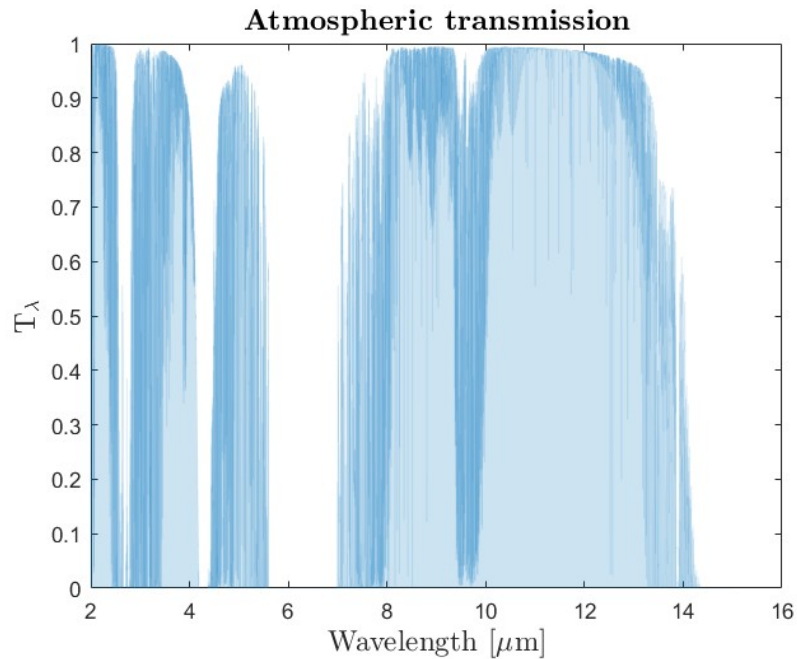
Figure 3.1: IR atmospheric transmission spectra at the zenith angle [17].

shown in Figure(3.1). In fact, due to its composition, the atmosphere will be transparent for certain wavelength bands and these are exactly the ones exploited in the engineering and choice of structures and materials for radiative cooling applications. Thus, for avoiding overheating of the atmospheric radiation, the RC system should emit strongly in the transparency windows of the atmosphere. Luckily, the maximum of the spectral radiance of a black body at temperature $T = 300K$ falls in the Long Wave Infrared (LWIR) transmission region of the spectrum, as observed in Figure (3.2).

For further assessment of RC performances, one has to evaluate the atmosphere emissivity. As mentioned before, the atmosphere radiate and scatter energy in an omnidirectional manner. However, without loss of generality, in this work the atmosphere is described as a hemisphere over the RC surface. The atmospheric spectral transmittance, as well as the atmospheric emissivity,
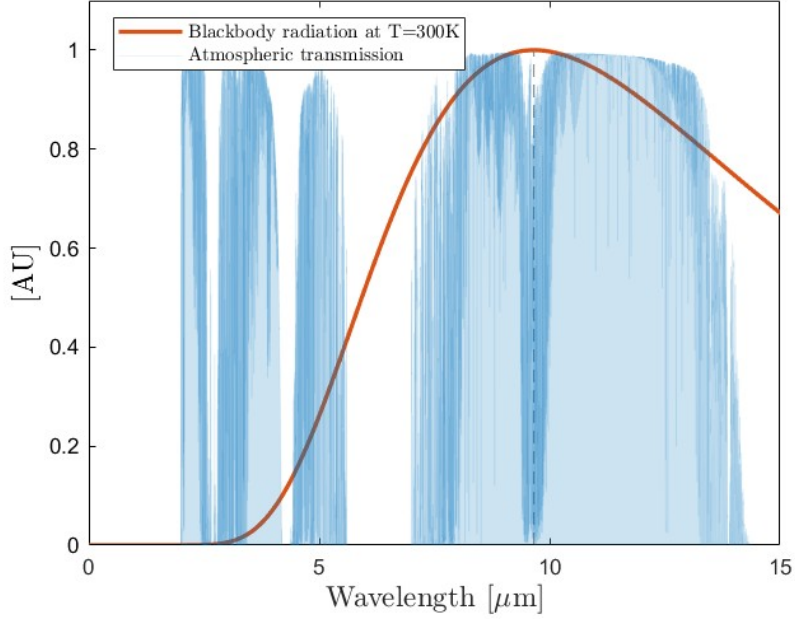
Figure 3.2: Overlap between the blackbody radiation at room temperature (T = 300K) and the atmospheric transmission.

depends on different factors, such as the temperature, the zenith angle θ, the cloud cover latitude, and air humidity. The latter constitute a crucial factor in the cooling power of RC devices, because water vapour absorbs infrared radiation [18], [19]. The spectral atmospheric emissivity is related to the spectral atmospheric transmission T_λ as follows

$$\epsilon_\lambda^{atm}(\lambda, \theta) = 1 - T_\lambda^{1/cos\theta} \tag{3.1}$$

In this form it is immediate to notice the explicit dependency of the spectral emissivty to the zenith angle. In Figure (3.3), one can observe that the emission decrease approaching the zenith ($\theta = 0°$) and tend to one for $\theta = 90°$.
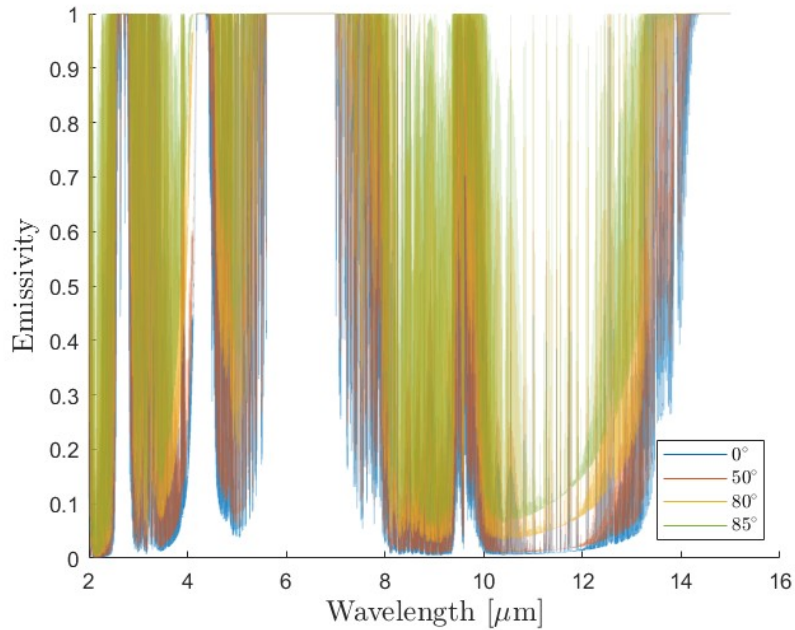
Figure 3.3: Atmospheric emissivity for different zenith angles.

3.1.2 SOLAR SPECTRUM

The solar spectrum refers to the distribution of electromagnetic radiation emitted by the sun which is distributed over a wide range of wavelengths, from Ultraviolet - Visible (UV-Vis) band to IR bands. The sunlight that reaches the earth passes through the atmosphere and gets attenuated due to the specific composition of the earth atmosphere, which is described in Section (3.1.1). The gas molecules present in the atmosphere are responsible for the absorption and scatter of the incoming solar radiation. The sun is modeled as a perfect emitter, i.e. a blackbody, nevertheless its spectral radiance after reaching the ground shows characteristic dips and absorption bands in the spectrum directly related to the behaviour of specific constituents present in the surrounding atmosphere [20], [21].

The American Society for Testing and Materials (ASTM) provided a reference for allowing an effective and reliable way to make measurements related to solar irradiance. The standard ASTM-G173 offers three different reference solar spectra (Figure (3.4)): the extraterrestrial solar spectral irradiance describes the radiation outside the earth atmosphere, i.e. Air Mass (AM) 0, the direct AM1.5 spectra represents the direct solar radiation not taking into account the atmo-
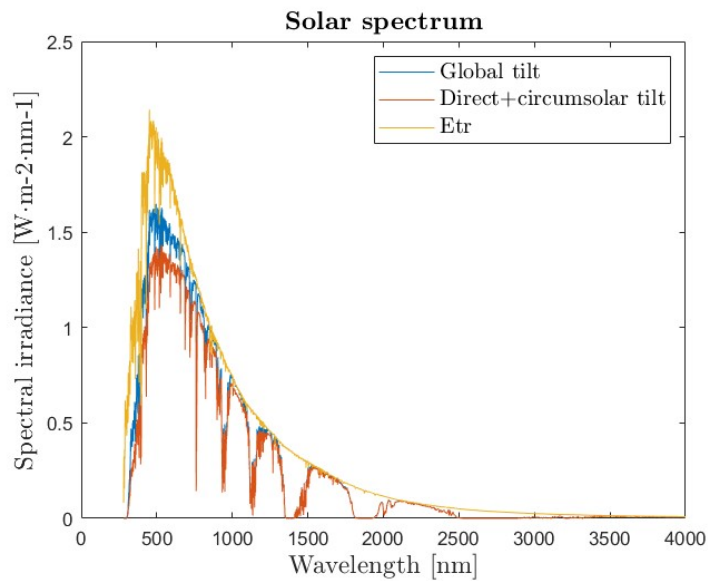
Figure 3.4: ASTM-G173 reference spectra: extraterrestrial solar irradiance (yellow line), irrandiances of the sun on ground level (orange and blue lines) [20].

spheric scattering, containing also a circumsolar component for a 5.8° field of view centered on the sun and, the global tilted hemispherical AM1.5 spectral solar irradiance describes the received radiation on a 37° tilted sun-facing surface [20].

The total integrated irradiances, i.e. the solar irradiation fluxes, for direct and hemispherical tilted spectra, for cloudless sky days, are $900.1\text{W} \cdot \text{m}^{-2}$ and $1000.4\text{W} \cdot \text{m}^{-2}$, respectively, with a diffuse component ranging typically between $50 - 100\text{W} \cdot \text{m}^{-2}$ [20], [22].

3.1.3 ACTIVE COOLING

Active cooling involves the use of mechanical or electrical systems to dissipate heat from either a device or environment. The principles behind active cooling are based on thermodynamics, namely the *Second Law of Thermodynamics*. Some of the most common active cooling mechanisms are forced convection processes or the ones based on the vapor-compression cycle. The most widely used is the first one, where a fluid, which can be either air or a fluid, is circulated over a hot surface to transfer heat away [13]. Active cooling technologies offer a satisfying cooling efficiency, but on the other hand, they can be expensive mechanisms, particularly difficult to implement in large-scale scenarios. Moreover, they can

be intensively energy demanding, increasing the overall electricity consumption and further environmental impact.

3.1.4 PASSIVE COOLING

Passive cooling is a design strategy that reduces heat gain and enhances heat dissipation without relying on mechanical systems but only on natural physical processes. Those are both non-radiative heat transfer mechanisms, such conduction and convection, or also radiative ones. Among the different techniques, there are some making use of the thermal mass, in fact materials present in the urban environment, such as concrete, absorb the heat during the day and releases it during cooler periods, hence at night. Moreover, other passive cooling strategies include natural ventilation and shading devices. Passive cooling strategies are based as well on thermodynamics laws and they can significantly reduce the energy demanding for heat dissipation, positively contributing to the reduction of the ecological footprint [23].

3.1.5 RADIATIVE COOLING

RC is the dissipation of heat of an object via the emission of thermal energy to the outer space which can be modeled as a perfect absorber at $T = 3K$. As seen in Section (2.1.2), most of the energy of the blackbody spectrum at ambient temperature, i.e. $T = 300K$, lays within the atmospheric window ($8 - 13\mu$m) [18]. This phenomenon occurs when the surface temperature is higher than the surrounding environment, allowing heat to be radiated away into the cold universe through the LWIR atmospheric window ($8 - 13\mu$m). In Chapter (4) all the different materials and structures exploited for achieving and/or enhancing RC performances will be thoroughly presented and described. This technique has various advantages, from its versatility to its scalability, cost-effectiveness and integration with other cooling techniques.

NIGHTTIME AND DAYTIME RADIATIVE COOLING

Passive radiative cooling can be classified into two different categories depending on their operating mechanisms: Nighttime Passive Radiative Cooling and Daytime Passive Radiative Cooling. The systems and devices operating

during nocturnal times are already widely spread and developed. One of the first application has been proposed by A.K. Head in 1959 [24], introducing the concept of selective emitter emitting mainly in the LWIR window. He anticipated the later on discoveries about the performances difference between a selective and a broadband emitter, stating that the cooling offered by a selective surface is better than a blackbody radiator which emits over the full band [25]. During the night, radiative cooling can lower the temperature of surfaces below the ambient temperature, providing a passive cooling effect. It is obvious that the wider the difference between coating temperature T_c and ambient one T_{amb}, the greater the cooling advantage is.

In recent years, daytime radiative cooling has gained attention, in fact peak of the incoming heat occurs during the day due to the direct intense solar irradiance. Therefore, in order to reach sub-ambient temperatures under these adverse conditions, special systems and structures have been developed. They are engineered to reflect the sunlight in $0.3 - 2.5 \mu$m while emitting thermal radiation, achieving cooling even under direct solar irradiance [6].

Daytime passive radiative cooling is hard to implement because of the lack of spectrally selective materials. In Chapter (4) different solutions in terms of structures and material design will be presented for achieving daytime RC. The first, that experimentally proved passive radiative cooling below ambient air temperature under direct sunlight, was A.P. Raman in 2014 [26]. Thanks to this deeply significant discovery, lot of interest was matured towards PDRCs, leading to the development of devices based on photonic materials, such as one-dimensional photonic films, metamaterials and multilayers.

3.2   FUNDAMENTALS OF RADIATIVE COOLING

This work will focus on passive daytime radiative cooling solutions, therefore let's present the fundamentals of RC under conditions of direct solar irradiance. During the daytime, the cooling performances of the system are quantified via the net cooling power, whose expression is presented in Eq. (3.2). As one can observe, also from Figure (3.5), the cooling advantage is a combination of solar and atmospheric radiation, surface thermal emission and heat loss induced by nonradiative phenomena [27].

Let's define the energy balance model of PDRCs as follows

Figure 3.5: Graphical representation of the energy exchange between a radiative cooling surface, the outer space and the sun [2].

$$P_{net} = P_{rad}(T) - P_{atm}(T_{amb}) - P_{sun}(T) - P_{cc} \tag{3.2}$$

with P_{rad} the radiative power of the coating, P_{atm} the absorbed energy related to the downward radiation energy emitted from the atmosphere, P_{sun} the absorbed power from solar irradiation and P_{cc} is the total power loss related to all non-radiative heat transfer processes, such as conduction and convection ones between the surrounding environment and the radiative cooler.
Conduction and convection phenomena are related to the environmental stimuli on the RC device. The first is mainly linked to the energy transferred by surrounding materials, whereas convection depends on the wind speed over the surface.

Let's focus on the meaning of each of the previously mentioned quantities, exploiting the theory extensively described in Chapter (2). A functionally ideal RC system should maximise the net cooling power P_{net}, hence the energy released by the surface must be maximised, simultaneously minimising the incoming energy absorbed by the coating. This, in terms of optical properties of the device, translates in an ideal behaviour consisting in 100% reflectance over the solar spectrum ($0.3 - 2.5\mu$m) to avoid the heating caused by the incoming solar irradiance, and in a maximisation of the emissivity, which ideally should be 1 over the LWIR atmospheric transmission window ($8 - 13\mu$m), so that heat can be effectively radiated to the outer space. Finally, the emittance over the other infrared bands of the spectrum ($2.5 - 8\mu$m and $> 13\mu$m) should be ideally zero for avoiding a further increase of the temperature of the atmospheric irradiation to a one greater of the temperature of the coating. This latter effect can be safely ignored when designing RC surfaces since the temperature difference

between the coating and the atmosphere is small in most of the cases. Therefore, the most influencing traits to take into account when engineering a RC structure must be the solar spectrum reflectance and the thermal LWIR emittance [28].

Radiative Power P_{rad}

The radiative power is expressed as a function of the coating temperature T_c as follows

$$P_{rad}(T_c) = A \int cos\theta \, d\Omega \int_0^\infty I_{b,\lambda}(T_c)\epsilon_\lambda(\Omega, \lambda) \, d\lambda \qquad (3.3)$$

with Ω the solid angle over the RC surface (for an explicit formulation see Eq. (2.25)), A is the passive radiative cooler surface area, $I_{b,\lambda}(T_c)$ the spectral radiation power of the ideal blackbody at temperature T_c, and $\epsilon_\lambda(\Omega, \lambda)$ is the spectral emissivity ratio of the RC coating.

The radiative power P_{rad} gets absorbed by the atmosphere and the outer space. The latter can be modeled as an ideal black body which has a temperature of $T = 3K$ degrees, hence given its low temperature its power radiation can be safely neglected. The same cannot be said about the power radiation of the atmosphere, which has a similar temperature of the one of the coating. As one can observe from Figure (2.4), most of the spectral radiant exitance of a blackbody with temperatures in between 0 and 50°C falls in the LWIR atmospheric transmission window. Therefore, to confirm what has been previously stated, to increase the cooling power of the RC surface and improve the overall performances of the system, the surface must be designed to show the highest possible emissivity in the LWIR window. Let's observe that according to Wien's Law (2.14), P_{rad} may be increased for higher temperature of the coatings.

Absorbed Power from Atmospheric Irradiation P_{atm}

The absorbed power from atmospheric irradiation is expressed as a function of the ambient temperature T_{amb} as follows

$$P_{atm}(T_{amb}) = A \int cos\theta \, d\Omega \int_0^\infty I_{bb}(\lambda, T_c)\epsilon(\Omega, \lambda)\epsilon_\lambda^{atm}(\Omega, \lambda) \, d\lambda \qquad (3.4)$$

with $\epsilon_\lambda^{atm}(\Omega, \lambda)$ is the spectral atmospheric emittance introduced in Section(3.1.1). In the previous years, for standardizing the evaluation of the net cooling power,

it has been chosen to assume $T_c = T_{amb}$. Hence, any coating temperature greater than the ambient one leads to an improvement of the overall performances of the RC system. This simplification descends from the fact that at $T_c = T_{amb}$ the radiative power emitted over the LWIR window and the absorbed power from atmospheric radiation almost coincide. Then, when estimating the emissivity of the coating, one is actually evaluating the behaviour of the RC system over the Mid-Infrared Region (MIR).

Absorbed Power from Solar Irradiation $\mathbf{P_{sun}}$

The absorbed power from solar irradiation is expressed as follows

$$P_{sun} = A \int E_{e,\lambda}^{sun}(\lambda)\epsilon_\lambda(\theta,\lambda)\, d\lambda \qquad (3.5)$$

with $E_{e,\lambda}^{sun}(\lambda)$ the solar direct spectral irradiation presented in Section (3.1.2) and $\epsilon_\lambda(\theta,\lambda)$ is the spectral hemispherical emissivity of the RC coating.

Solar irradiation is the main impairment to RC performances. Indeed, as introduced in Section (3.1.2), the mean solar radiation is about $1000\text{W} \cdot \text{m}^{-2}$ and typical RC coatings cooling performances are about $\approx 150\text{W} \cdot \text{m}^{-2}$ during daytime. This is the reason why for achieving high performances in passive daytime radiative cooling a surface reflectance of at least 90% in the solar spectrum must be guaranteed.

Nonradiative energy transfer $\mathbf{P_{cc}}$

$$P_{cc} = Ah(T_{amb} - T_c) \qquad (3.6)$$

with h the total heat transfer coefficient which takes into account the heat transfer caused by convection and conduction phenomena. Several solutions to minimize nonradiative heat transfer have been studied and developed in the past years. To avoid conduction heat transfer the coating is usually placed on a thermal insulation substrate directly in contact with the environment atmosphere. Moreover, for limiting the increase of the temperature of the RC coating due to convection, a thermal shield is employed [28].Finally, let's observe that usually, for unobstructed surroundings, the angle dependency of the spectral emissivity

can be dropped, since the variation related to such angle is almost null.

SELECTIVE EMITTER

Combining the knowledge about the atmospheric transmission with the requirements for an effective and optimal RC surface, one may model an optimal emissive behaviour for the cooling system. As introduced in the previous section, one would at best engineer a RC structure with a strong thermal LWIR emittance. However, most of the materials employed for radiative cooling do not exhibit a selective behaviour, but a broadband one. The problem related to a non-selective emitter lays in the fact that it absorbs the atmospheric thermal radiation over almost all the IR spectrum, accordingly to the atmospheric transmission, whenever the coating temperature is smaller than the atmospheric one. This deeply compromise the cooling performances of the RC system. In addi-
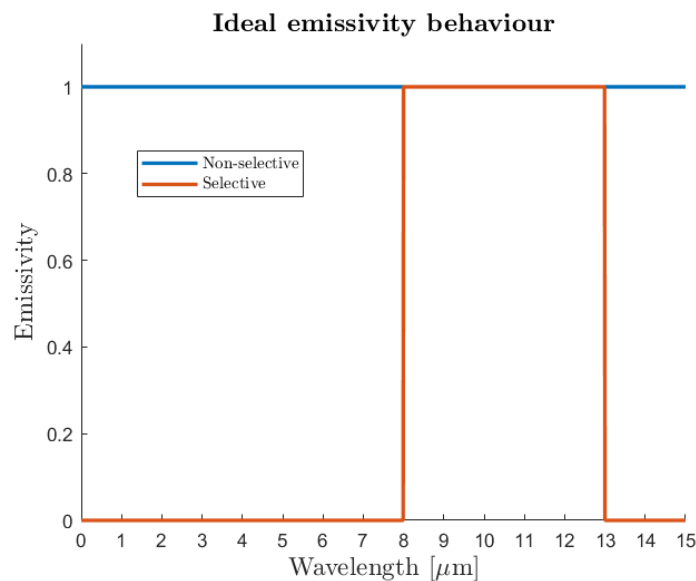
Figure 3.6: Ideal selective and non-selective emissivity in the IR spectrum.

tion, usually RC researches, included this analysis, assume to work with surfaces horizontally placed and facing the sky with an unobstructed view. However, for the sake of completeness, since one of the main application for these passive radiative cooling surfaces is to coat buildings, it is of crucial importance taking into account also the orientation of the surface. Indeed most area of the latter will be vertically oriented, hence, apart seeing part of the sky, at least half of the field of view will subtend the terrestrial features surrounding the building.

The terrestrial irradiance drastically vary during the seasons and it can reduce or even reverse the RC behaviour of the coating during summers and overcool the surfaces during winters [19].

An ideal selective LWIR emitter, reported in Figure (3.6), is expressed as

$$\epsilon_\lambda(\lambda, \theta) = \begin{cases} 1 & 8\mu m \leq \lambda \leq 13\mu m \\ 0 & \text{otherwise} \end{cases} \tag{3.7}$$

Therefore, selective LWIR emitters yield a greater cooling in comparison with broadband ones, allowing an higher temperature drop. In conclusion, let's notice that in equilibrium conditions, i.e. $T_c = T_{amb}$, the performances of selective and non-selective RC surfaces are a lot similar [28].

4

Material designs for PRC surfaces

This chapter explores various material designs for Passive Radiative Cooling (PRC) surfaces, focusing on their spectral selectivity for obtaining daytime cooling. The examination of different type of PRC solutions are presented, such as colored, transparent, and mirror types—RC devices, highlighting their functionalities and applications. Additionally, more advanced approaches are discussed, like adaptive and disordered photonic media, emphasizing polymer-based coatings for scalable and cost-effective solutions.

Radiative cooling presents itself as a natural phenomenon, in spite of that the features required for achieving passive radiative cooling, specifically during the daytime, impose the material to have strong reflection ability in the solar spectrum ($250 - 2500$nm) and intense infrared emissivity in the atmospheric window ($8 - 13\mu$m). Such spectral selectivity cannot be obtained by using bare natural materials, but different structures and designs have to be engineered. Thanks to new manufacturing processes of surfaces both at micro and nano-scale, it is possible to achieve great performances combining disordered media and polymeric photonics realizing PRC materials on a large scale [25].

Radiative coolers can be categorized based on their visual appearance, in fact these surfaces can have multiple functionalities and they can be employed for different purposes. This means that apart from guaranteeing heat dissipation in the atmospheric window, one can tailor their behaviour in the visible part of the spectrum depending on the final employment. Radiative coolers can be *colored*,

transparent or *mirror* type.

Apart from the obvious goal of trying to enhance the cooling performances of the involved surfaces, one cannot ignore their visual appearances, since, in this case, their final use is covering the exterior of buildings. It is important to
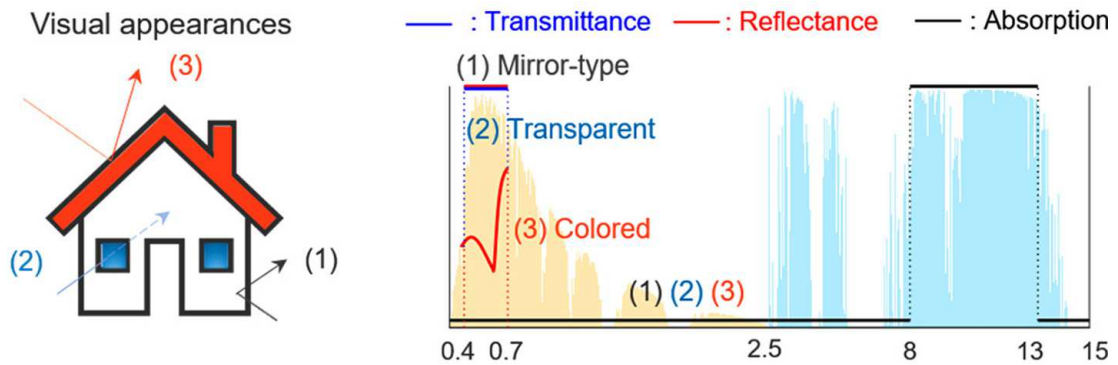
Figure 4.1: Visual appearances of different types of RC surfaces: (1) *mirror* type, (2) *transparent* type and *colored* type [2].

notice that any coloration given to the surface hinders the cooling performances of the latter, due to the selective absorbance in the visible part of the spectrum. Colored radiative coolers can be obtained with different mechanisms, involving the use of classical color pigments, combining together the properties of metals and inorganic materials, exploiting total internal reflection or using periodic photonic structures that obey to Braag's Law [29].

Traditional dyes absorb the whole visible light spectrum except for the scattered and/or reflected wavelength that characterizes the specific color of the coating. It has been shown that photoluminescent dyes can achieve both coloration and good passive radiative cooling performances, absorbing a certain band of light and causing photoexcitation. Hence, the excess energy that will be released from the surface, it will actually characterize the color of the device.

An other possible solution involves the selective behaviour obtained combining the absorption offered by inorganic materials and the reflection of metals. For instance, by designing the architecture of a nanostructure of Silicon (Si), one can obtain colored PDRCs. However, controlling the geometric parameters of dielectric metasurfaces is not an easy process and it involves costly manufacturing methods, which sets a limit to the overall scalability of these devices. One can also design colored PDRCs as a multi-layer structure, seeing the structure as a Fabry-Perot cavity, hence the selective absorption varies depending on the

thickness of the dielectric and the metals.

Surfaces, whose colored appearance is based on Total Internal Reflection (TIR), exploit the refractive index discrepancies at the interface between different materials constituting the structure of the coating. Such optical phenomenon can selectively reflect specific wavelengths, by adjusting the critical angles and the refractive index differences.

Finally, colored RC devices are also obtained through the use of periodic structures obeying *Braag's Law*:

$$k = \frac{\pi}{\Lambda} \tag{4.1}$$

with Λ the lattice distance. Such law states that whenever the frequency of the impinging light e^{jkx} satisfies the Braag's condition, then the radiation cannot propagate inside the structure, hence it will be reflected [15]. These structures can be engineered by precisely controlling the the lattice spacing and tuning the index of the material. Their optical properties consist in the selective reflection of certain wavelengths of light through the careful manipulation of the structural parameters and material composition [2], [28].

As mentioned multiple times at this point, RC devices offer a wide range of
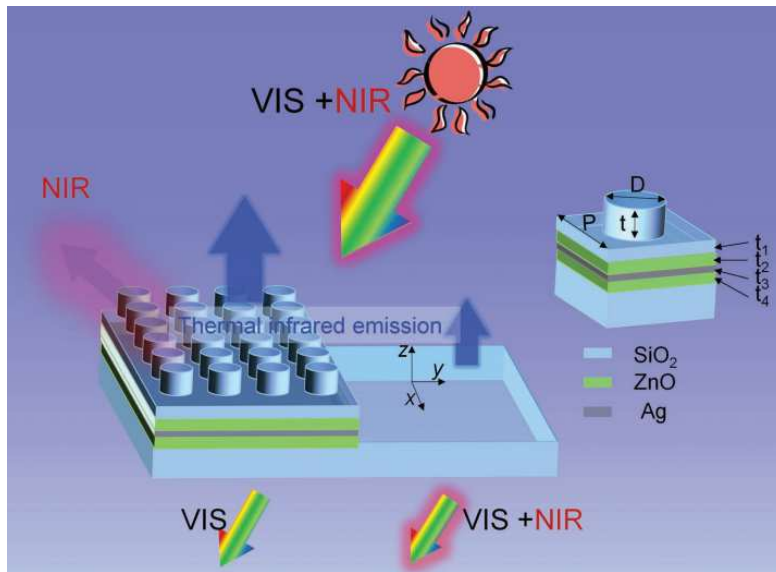
Figure 4.2: Schematic of a transparent RC device with a 2D grating structure on top; on the right a single unit is shown where $D = 5.40\mu$m is the diameter of the pillar, $t = 2.51\mu$m the height of the pillar, $P = 7.80\mu$m the period and t_1, t_2, t_3 and t_4 are the thicknesses of SiO_2, ZnO, Ag and ZnO, respectively [30].

functionalities besides their thermal management. An additional advantage supplied by a specific category of RC devices is transparency in the visible part

of the spectrum. Therefore, such coatings have the ability to maintain their optical clarity transmitting the range of visible wavelengths and simultaneously emitting thermal radiation. The applications are wide, from residential or commercial buildings and vehicles windows to solar cells.

For achieving high visible transmission, Near Infrared Region (NIR) reflection and MIR emission, simultaneously, one has to combine a NIR reflecting filter and a transparent MIR emitting structure. An interesting example is given in [30], where a dielectric-metal-dielectric (D/M/D) film of ZnO/Ag/ZnO is combined with a 2D SiO_2 photonic structure for enhancing MIR emission (Figure (4.2)). Such synthetical cooling structure is prepared through really expensive techniques of magnetron sputtering deposition and photolithography. Let's notice that thanks to the intrinsic high precision of the lastly mentioned method, the top surface is considered smooth. Indeed, the roughness on top of each pillar is 6.2nm which is way smaller than the impinging wavelength, hence, thanks to Rayleigh criterion, a smooth surface assumption is reasonable. This structure yielded 77% visible light transmittance, 57% NIR solar radiation reflected and 91% thermal infrared radiation emitted, offering a potential solution for passive daytime radiative cooling for transparent applications.

Finally, *mirror*-type RC devices aim to reduce as much as possible the absorbed power from solar irradiation, maximizing the cooling power Eq. (3.2). This is achieved guaranteeing high reflectance in the visible and NIR of the spectrum.

As discussed in the previous sections, the design adopted by RC devices consists in reflecting solar irradiation and achieving high emissivity of mid-infrared radiation through the LWIR atmospheric window. Moreover, as extensively presented in Section (2.1.2), any body with a temperature different from the absolute zero will continuously emit thermal radiation, implying that the system considered will undergo spontaneous radiative cooling. Such behaviour is actually beneficial for reducing the energy consumption over hot summers, however this is not desired in winter. In fact, this may lead to overcooling during winters, causing an unwanted increase in the the heating energy demands. As solution to such issue, dynamic switchable RC coatings have been developed. Adaptive RC has a wider range of applicability compared to passive RC, indeed, the spectral emissivity of the coating is manipulated thanks to the device response to external stimuli. The dynamic switchability of coatings can be caused by

temperature variation, external energy input or mechanical stress application. The optical properties of phase-changing materials vary by changing the critical temperature T_{ct}: the coating operates in cooling mode whenever $T_c > T_{ct}$ and in heating mode when $T_c < T_{ct}$, with T_c the temperature of the coating. Some typical phase-change materials employed in adaptive RC are VO_2 and any perovskite structure. The latter show metal-to-insulator transitions for high temperatures, making them not properly suitable for on-earth RC applications, but combined with their lightness and resistance to oxidation and high temperatures, perovskite structures are optimal candidates for space applications.

Coatings designed with VO_2 are much more appealing, in fact they show a thermally induced insulator-to-metal phase transition at the temperature of $T_{ct} := T_{IMT} = 68°C$. These coatings are designed for maximizing the emission in the atmospheric transmission window. In fact, they achieve adaptive radiative cooling without compromising the solar spectrum reflectance and without the requirement of any external energy input. Moreover, the transition temperature can be reduced close to ambient temperature by engineering a structure based on VO_2 doped with Tungsten (W).

For instance, in [31] they propose a metasurface with a base of Ag as reflector,
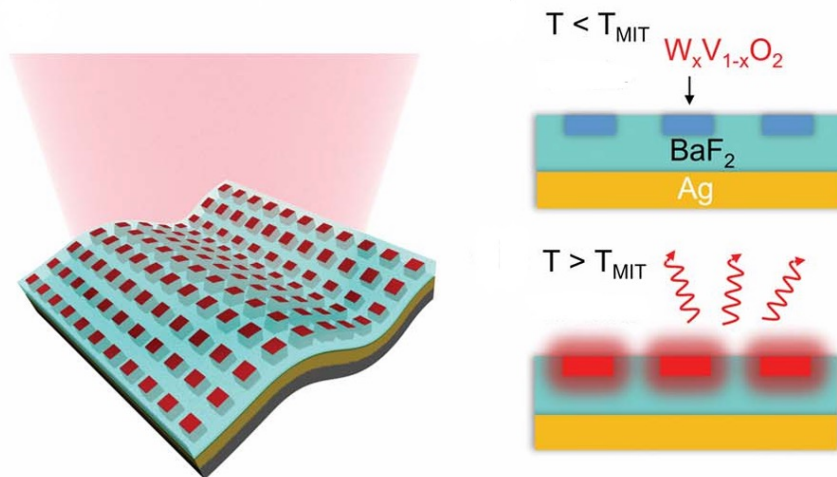
Figure 4.3: Schematic of the metasurface, material composition and operational modes of a W-doped VO_2 coating [31].

Barium Fluoride (BaF_2) as dielectric and a two dimensional array of W-doped VO_2 lithographically patterned on the coating, obtaining a transition temperature of $T_{IMT} = 22°C$. In the insulating state the infrared radiation gets reflected back by the metal base at the bottom of the structure, but as the temperature of

the environment grows above the critical one, the metasurface starts behaving like a metal enhancing the infrared emissivity of the coating, achieving values from 0.2 to 0.9. Unfortunately, this approach for adaptive RC has major downsides, such as the use of metasurfaces that cause a huge impairing in the development of these solutions caused by the high prices of manufacturing. Secondly, VO_2 performances are reduced by the material oxidation in air, making it a not really suitable candidate for the applications discussed so far.

Given the stretchability of polymers, such as PDMS, another method for varying the optical properties of the material is by applying an external mechanical force. The solution proposed in [32] consists of a reconfigurable nanophotonic structure made of a PDMS matrix embedded with three different types of nanoparticles (Silicon Carbide (SiC), Silicon Nitride (Si_3N_4) and Boron Nitride (BN)) on top of a one dimensional grating of Ag. By deforming this
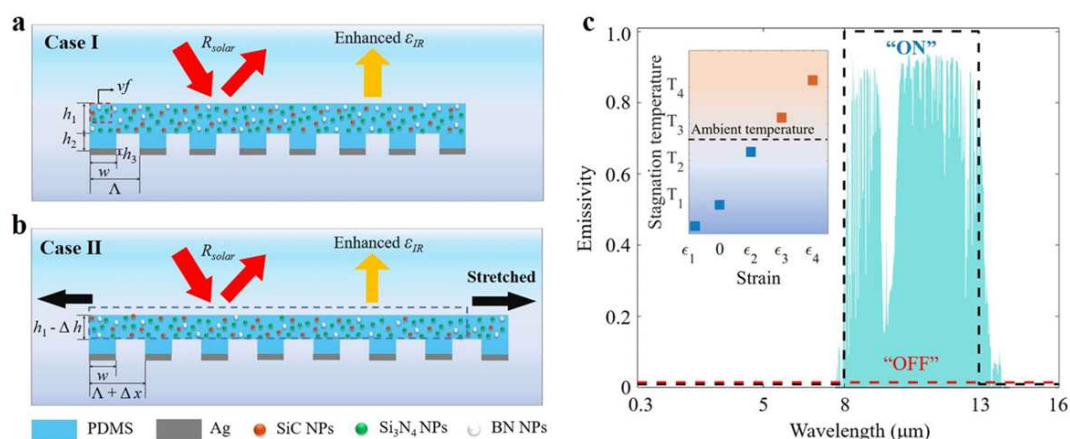
Figure 4.4: PDMS film embedded with nanoparticles on top of a one-dimensional Ag grating: (a) unstrained structure, (b) the structure subject to an external mechanical force causing its deformation and (c) schematic representation of the emissivity in the two RC operational modes and finally the inset displays different stagnation temperatures for different applied strains [32].

structure a variation in the optical response of the material is obtained. The nanophotonic device subject to different strains varies both the thickness of the PDMS film and the period of the Ag grating. Thus, the dynamic tuning of the RC performances of the structure, caused by its mechanical deformation, leads to reversible and continuous "ON" and "OFF" modes in LWIR window, leaving almost unchanged the solar spectrum reflectance offered by the Ag coating [28].

4.1 Disordered Photonic Media

All the different possible solutions for RC proposed so far, are all limited by the hard manufacturing process, hence hard to implement on a large scale. Luckily, there exists a really powerful tool which is a common characteristic of almost all real materials, which is the *disorder*. It has been proven during the years that this feature could offer highly efficient and cost-effective PDRC heat dissipation solutions [25].
Disordered photonic structures are characterized by randomly distributed dielectric particles. By specifically controlling the type and particle size of the disordered nanofillers, one can separately adjust the solar spectrum reflectance and the infrared emissivity of the sample.

The high solar reflectance that has to be reached by these photonic structures is achieved by multiple scattering of the incoming sunlight. Scattering phenomena can be obtained by introducing a number of interfaces with dielectric contrast, such as pores or dielectric particles, in a polymer matrix with a different refractive index. For avoiding the absorbance of solar irradiation, the fillers suitable for this employment should have an higher band gap than the mean energy of solar photons [33], nevertheless an higher refractive index is favorable for increasing the scattering of individual particles. As presented in Chapter (2), the energy of a photon is computed $E = hc/\lambda$, therefore the energy of sunlight constituents will range from $0.49 - 4.13$eV.
Particles with a wider bandgap posses a lower refractive index, as one can also observe form Figure (4.5). For what concerns particles such as SiO_2, Aluminum Oxide (Al_2O_3), and Barium Sulfate ($BaSO_4$), they do not have a sufficiently high contrast with the polymer matrix, which it has in general a refractive index of ≈ 1.5. The consequences linked to these features will be further explored in the following sub-section (4.1). Whereas, on the other hand, high refractive index materials, such as, Titanium Dioxide (TiO_2), yield huge reflectivity in the visible and near infrared, but due to their small bandgap lots of UV radiation gets absorbed. Therefore, there is a tradeoff in the choice of the material and also of the concentration of the scaterrers: commonly the fillers that are used the most are the ones having a photonic bandgap near to the upper limit of the energy of the solar photons, i.e. 4.13eV.
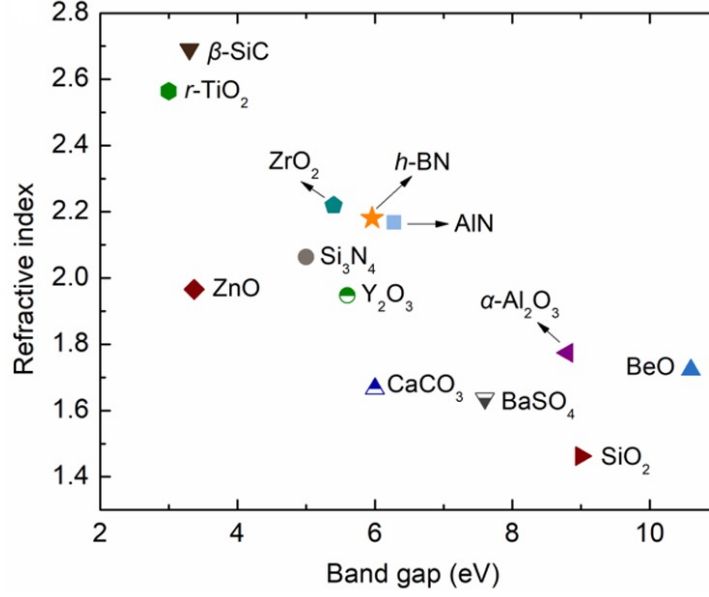
Figure 4.5: Refractive index as function of the bandgap of some dielectric microparticles [34].

The materials used for spectral selective cooling leverage on their phonon modes in the MIR spectrum to achieve selective thermal emission. Moreover, choosing low molecular weight compounds and uniform coatings helps optimize this process for effective cooling [35]. The potential candidate materials show a behaviour similar to a plasmonic metal, whose behaviour is modelled by the Drude model, this means that they display high reflectance as uniform layers, but they are characterized by sharp resonances as nanoparticles. The strong reflection lays within a wavelength region known as *Reststrahlen band*, bounded by the transverse, ω_{TO}, and longitudinal, ω_{LO}, optical phonon frequencies. Inside this range, the dielectric permittivity of the material is negative, yielding a strong reflectivity.

$$\epsilon(\omega) = \frac{(\epsilon(0) - \epsilon(\infty))\omega_{TO}^2}{\omega_{TO}^2 - \omega^2 + 2i\omega\Gamma_{ph}} \tag{4.2}$$

where $\epsilon(0)$ is the long wavelength permittivity, i.e. the response of the material to a slowly varying or static electric field, $\epsilon(\infty)$ is the short wavelength permittivity, i.e. the response of the medium to higher frequencies, where only fast electronic polarizations are effective, and Γ_{ph} the phonon scattering rate [36]. Against this background, materials exhibiting Reststrahlen bands, posses a permittivity that changes significantly between the ω_{TO} and ω_{LO}: below the transverse phonon

frequency (long wavelength), the permittivity is high, whilst, as the frequency approaches the longitudinal phonon frequency (short wavelength), the permittivity drops sharply, often becoming negative, leading to strong reflectivity in the Reststrahlen region.

Within the Reststrahlen band one can excite surface phonons on nanoparticles, whose resonance peak will occur at $\omega = \omega_{res}$ given by

$$\omega_{res}^2 = \frac{\omega_{TO}^2(2\epsilon_h) + \omega_{LO}^2\epsilon(\infty)}{2\epsilon_h + \epsilon(\infty)} \tag{4.3}$$

where ϵ_h is the dielectric permittivity of the material where the particle is embedded. If this resonance is localized within the atmospheric transmission window, the nanoparticle is a good candidate for radiative cooling. Hence, RC materials, where the selective emission is in the thermal range helps materials cool by radiating heat to the cold sky.

One of the most promising disordered PDRC solution, both in terms of performances, applicability and inexpensiveness, is given by dielectric microsphere coatings prepared by painting [37]. High emissivity can be reached by tuning the fill rate and the radius, i.e. the dipole resonance in the infrared, of the microparticles [28]. Such constituents can be easily embedded within polymer foils or thin IR transmitting films, yielding the desired absorption profile. For
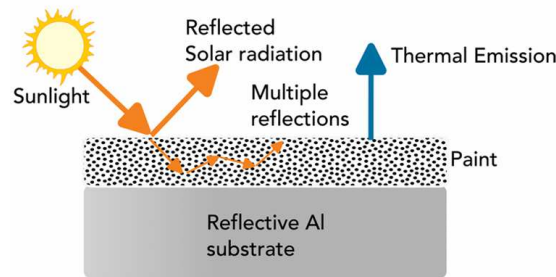
Figure 4.6: Schematic of a the painted sample where the coating contains radiative and reflective fillers deposited on top of an Al substrate [38].

better characterize these type of coatings, let's try to focus on the fundamental parameters of PDRC surfaces. One of the most important parameter of paint is gloss and it is influenced by the distribution and concentration of pigments in the paint film. Paint films normally have a degree of surface roughness which is related to the flow and leveling of the paint and the presence of pigments.

Rough surfaces are generally modeled as random structures, in fact they generate uncoherent scattering waves, even for coherent sources.

Since the surface roughness of paint is notably affected by the degree of pigment dispersion, for a given pigment loading, it has a significant effect on gloss levels in most paint. Moreover, one cannot neglect the presence of coalescence of particles in paint, which results in a growth in the mean particle size of pigments and hence growth in surface roughness.

Recent studies have proposed polymer-based PDRC coatings and paints because of their potential large-scale production and low cost of manufacturing. Photonic polymeric structures are engineered to achieve selective reflectance and thermal emittance, by designing the type and size of the randomly distributed fillers.

RADIATIVE NANOFILLERS

A polymeric matrix embedded with nanoparticles shows emission bands in the IR region that overlap with the atmospheric transmittance window LWIR. This is due to the vibrational transitions of functional groups of the polymers such as C-F (Carbon-Fluorine bond) and C-O (Carbon-Oxygen bond) [39]. Such PDRC coatings may reach good average emittance in the LWIR because of the intrinsic absorption ability of the polymers. However, near-perfect emittance cannot be reached, because of the inevitable interface reflection between air and polymer. An ideal emittance is $\bar{\epsilon}_\lambda = 0.99$ and it may be achieved by modifying the morphology of the surface with some patterns and/or other structures, e.g. grating patterns [28]. For avoiding the involving of such expensive structures, similar performances can be obtained by porous surface polymer coatings, which couple the effect of microspheres and microstructured surfaces. Those solutions can be easily painted and can achieve high average emissivity $\bar{\epsilon}_\lambda = 0.97$ at room temperature [40].

Moreover, the optical properties of the polymer may also be designed by choosing as nanofiller SiO_2 microspheres, which increase the reflectance of the solar spectrum leaving unchanged the emissive properties [41].

The main downsides of using dielectric microparticles are the lack of flexibility and water-repellence [28].

REFLECTIVE NANOFILLERS

The simplest method for reaching high reflectance in the solar spectrum is to use an highly reflective metal substrate, e.g. Al or Ag. Therefore, taking into account also the high selective emittance that has to be met, PDRC can be obtained by coating polymers or dielectric materials on top of metal reflectors. A further improvement of the solar reflectance can be reached by exploiting scattering phenomena, namely Mie scattering [15]. Mie scattering is a form of elastic scattering, i.e. the frequency of the scattered radiation is the same of the impinging one, for which the light gets scattered by particles that have a diameter similar to or larger than the wavelength of the incident light. The scattering efficiency of the surface is linked, accordingly to Mie theory, to the contrast between the refractive index of the impinging medium and the surrounding one. Additionally, the size and shape of these particles play crucial roles. In fact, a higher difference in refractive indices leads to more effective scattering of light. Similarly, the specific morphology and particle size determine how light is scattered, with certain sizes and shapes enhancing the scattering process [25].

Therefore, randomly stacking dielectric microspheres, e.g. SiO_2, Calcium

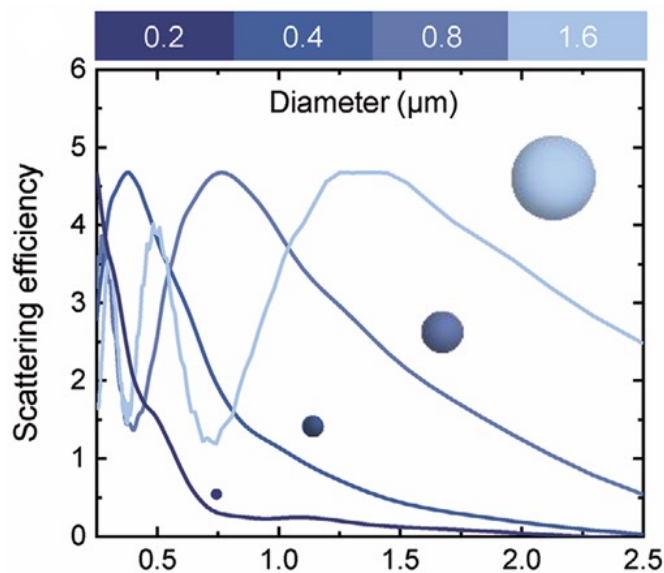Figure 4.7: Scattering efficiency for spheric scatterers with different sizes [34].

Carbonate ($CaCO_3$), TiO_2, or polymer microspheres, such as PolyVinyliDene Fluoride-HexaFluoroPropylene (PVDF-HFP), can yield PDRCs that can achieve high solar reflectance [42]. However, for reaching a reflectance above 90% in the solar spectrum, a large thickness of the coating is necessary, this is due to

the similar refractive index between polymer and dielectric scatterers. Finally, the concentration and the size of the particles have deep consequences on the optical properties of the coating. In fact, it has been shown that larger particles and a wider distribution can translate the reflection zone towards NIR [43].

5

Materials and methods

5.1 Samples manufacturing process

For the first part of the measurement campaign, the samples are divided into two categories: the first set has been deposited on a substrate of raw Al on which a film of Al (50nm), one of SiO_2 (20nm) and one of TiO_2 (20nm) have been deposited via Physical Vapour Deposition (PVD). The resulting substrate gets referred as V95 and it is provided as reference substrate on the second-last top rights position in Figure (5.1), covered with a protective bluish layer.

The second set of samples were created by using a substrate of Al with just one coat of Al deposited via PVD. Let's notice that due to the intrinsic nature of the material there has been a natural growth of Al_2O_3 on the top surface. The resulting substrate gets referred as S90 and it is provided as reference substrate on top rights in Figure (5.1) with a protective yellowish layer.

Physical Vapour Deposition

One of the most common thin-film fabrication processes is PVD. It is a process for depositing optical thin films in which atoms or molecules of a material are vaporized in a vacuum chamber from a solid source and condensed one by one onto the surface of a substrate. The result is an extremely pure thin film with a thickness ranging from 0.1 to 100nm, produced with the deposition tech-

nique that has the lowest environmental impact. One of the main advantages of this production technique is that the deposited layers are resistant and durable. Additionally, coatings deposited with the PVD technique have a high tolerance for high temperatures and are extremely impact-resistant.
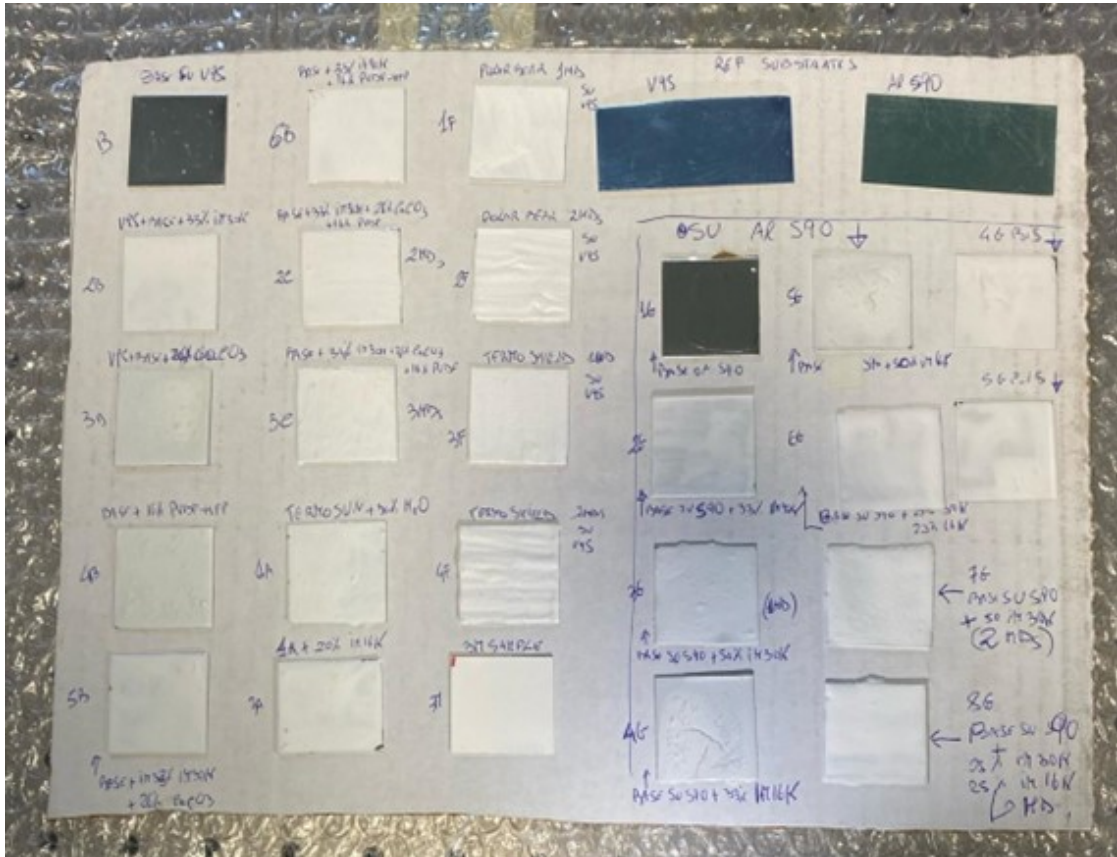

Figure 5.1: First set of samples.

The lists of samples deposited on the substrates V95 and S90 are reported in Table (5.1) and in Table (5.2), respectively.

For the paint formulation a commercial water-based colorless acrylic paint (*Exterieur* by ThermoShield) with low Volatile Organic Compounds (VOCs) $\leq$ 3g L^{-1} containing TiO_2, ZnO, kaolin, $CaCO_3$, silicates and water [44] was manually mixed with different scatterers and water. The proposed scatterers are $CaCO_3$, $BaSO_4$, PVDF-HFP in powder form, IM30K and IM16K SiO_2 microparticles by 3M [45], [46]. In Table (5.1) and (5.2) the chosen concentration for each specific scatterers is reported. Combining these different components allow to create a lightweight mixture able to reach high reflectance values over the UV-Vis and

NIR bands thanks to the SiO_2 bubbles and other scatterers and increase the emissivity of the acrylic base and the scatterers alone. In fact, the choice to include into the paint formulation the PVDF-HFP was done in order to increase the selective emittance in the LWIR. Moreover, let's notice that the PVDF-HFP has been added to the paint formulation in its powder form. This allows to avoid the use of its solvent, which is commonly Acetone or Toluene, producing a paint with zero VOCs, accordingly to the new EU rules about environment. Then, the prepared paint was applied using a brush on two different substrates V95 and S90. Moreover, as one can notice, the painting has been applied more than once in specific samples in order to increase the thickness of the latter, i.e. 2C, 3C, 2F, 7G, 8G.

IM30K AND IM16K SiO$_2$ MICROPARTICLES

IM30K and IM16K 3M SiO_2 microparticles are glass spheres with a diameter of around $20\mu m$ and an air cavity inside. 3M glass bubbles help to reduce the weight of the material, reducing its thermal expansion and contribute to material and cost savings. Among the key differences between IM30K and IM16K there is their density: both of them are lightweight, but IM30K is slightly less dense, offering a maximum weight reduction when necessary. Secondly, IM30K bubbles tolerate higher pressure environments in comparison to IM16K, therefore in terms of applications, in general, IM30K microparticles are more suitable for high-performance scenarios.

Moreover, their particular conformation allows getting high scattering in the visible part of the spectrum ($380 - 750$nm) and as a consequence the glass bubbles possess also a high and broad emissivity in the IR spectrum [45], [46].

Table 5.1: List of samples deposited on substrate V95.

V95 substrate samples	
B	Acrylic base
2B	Base+33% w/V glass bubbles (3M) IM30K type
3B	Base+26% w/V of CaCO3 powder
4B	Base+16% w/V of PVDF-HFP
5B	Base+33% w/V glass bubbles (3M) IM30K type+26% w/V of CaCO3 powder
6B	Base+33% w/V glass bubbles (3M) IM30K type+16% w/V of PVDF-HFP
2C	Base+33% w/V glass bubbles (3M) IM30K type+26% w/V of CaCO3 powder+16% w/V of PVDF-HFP (two coats of paints)
3C	Base+33% w/V glass bubbles (3M) IM30K type+26% w/V of CaCO3 powder+16% w/V of PVDF-HFP (three coats of paints)
1A	Commercial white paint already incorporating glass bubbles
3A	1A+20% w/V glass bubbles (3M) IM16K type
1F	Polar BEAR (commercial water-based cooling paint) one coat of paint
2F	Polar BEAR (commercial water-based cooling paint) two coat of paint
3F	Thermoshield (commercial solvent-based cooling paint) one coat of paint
4F	Thermoshield (commercial solvent-based cooling paint) two coats of paint
3M	TBD composition

Table 5.2: List of samples deposited on substrate S90.

S90 substrate samples	
1G	Acrylic base
2G	Base+33% w/V glass bubbles (3M) IM30K type
3G	Base+50% w/V glass bubbles (3M) IM30K type
4G, 4G$_{BIS}$	Base+33% w/V glass bubbles (3M) IM16K type
5G, 5G$_{BIS}$	Base+50% w/V glass bubbles (3M) IM16K type
6G	Base+25% w/V glass bubbles (3M) IM30K type+25% w/V glass bubbles (3M) IM16K type (one coat of paint)
7G	Base+50% w/V glass bubbles (3M) IM30K type (two coats of paint)
8G	Base+25% w/V glass bubbles (3M) IM30K type+25% w/V glass bubbles (3M) IM16K type (two coats of paint)

The second measurement campaign was performed on another set of samples, that have been specifically manufactured on the results obtained from the first campaign. In fact, the ones showing better performances in the UV-Vis and NIR part of the spectrum were selected for this second part of the experimental process. These samples were composed of commercial water-based colorless acrylic paint (*Exterieur* by ThermoShield) with low VOCs $\leq$ 3g L^{-1} containing TiO$_2$, ZnO, kaolin, CaCO$_3$, silicates and water [44], 25% IM30K SiO$_2$ microparticles by 3M [45] and 25% of water. Let's notice that the painting here has been repeated up to four times, as one can observe from what reported in Table (5.3). Moreover, before drying, a NPF was incorporated into the sample. This film is a 16μm microporous trilayer membrane composed of polypropylene (PP), polyethylene (PE), and polypropylene (PP) (PP-PE-PP film), which is called *Celgard-C210* [47]. The thin film was applied over the wet paint using a roller, smoothing its surface and flattening the typical texture left by the brush, as one will observe in the morphological characterization in Section (6.2).

Table 5.3: List of samples deposited on substrate V95 and S90 for increasing amount of paint coats.

| V95 and S90 substrates samples with different # of coats of paint	
V95-3F	Base+Thermoshield+25% w/V glass bubbles (3M) IM30K type (one coat of paint)
V95-3F-1C	Base+Thermoshield+25% w/V glass bubbles (3M) IM30K type (one coat of paint)+Celgard
V95-3F-2C	Base+Thermoshield+25% w/V glass bubbles (3M) IM30K type (two coat of paint)+Celgard
V95-3F-3C	Base+Thermoshield+25% w/V glass bubbles (3M) IM30K type (three coat of paint)+Celgard
V95-3F-4C	Base+Thermoshield+25% w/V glass bubbles (3M) IM30K type (four coat of paint)+Celgard
S90-3F	Base+Thermoshield+25% w/V glass bubbles (3M) IM30K type (one coat of paint)
S90-3F-1C	Base+Thermoshield+25% w/V glass bubbles (3M) IM30K type (one coat of paint)+Celgard
S90-3F-2C	Base+Thermoshield+25% w/V glass bubbles (3M) IM30K type (two coat of paint)+Celgard
S90-3F-3C	Base+Thermoshield+25% w/V glass bubbles (3M) IM30K type (three coat of paint)+Celgard
S90-3F-4C	Base+Thermoshield+25% w/V glass bubbles (3M) IM30K type (four coat of paint)+Celgard

Figure 5.2: NPF called Celgard-C210.
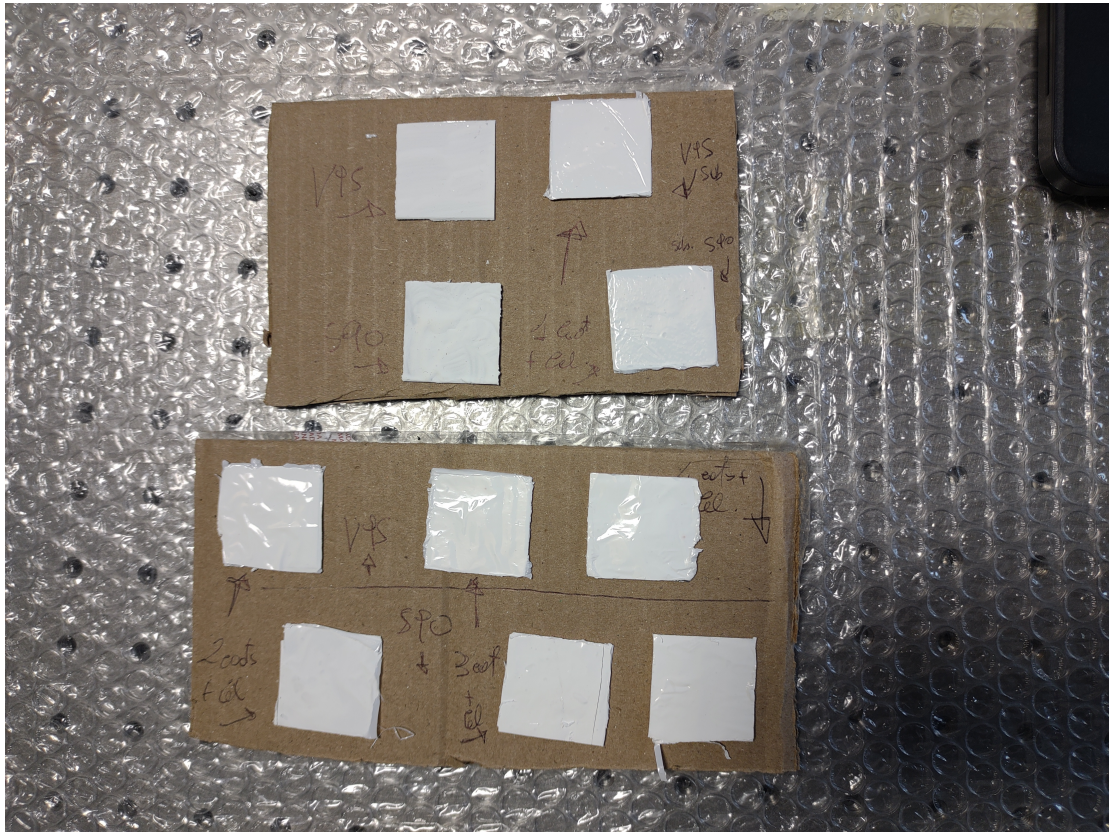
Figure 5.3: Second set of samples.

5.2   OPTICAL CHARACTERIZATION

5.2.1   CARY 5000

The spectrophotometer and the related software program used for analysing the samples is the *Varian Cary 5000*, which can measure from UV-Vis to the NIR, and the *Scan* software. The system consists of a double out-of-plane Littrow monochromator with a collimator section. The beam splitting system consists of a chopper which deviates part of the beam to the front and part to the rear of the device with a rotating frequency of 30 Hz. One of the two beams is used as reference and one for the measurement, this procedure is called double beam compensation. The spectrophotometer is equipped with three light sources: a Tungsten halogen lamp for the visible, a deuterium arc UV lamp and a mercury lamp for automatic calibration. The spectrophotometer has a wavelength accuracy of ±0.1nm in the UV-Vis and of ±0.4nm in the NIR [48], [49]. A picture of the device is shown in Figure (5.4).
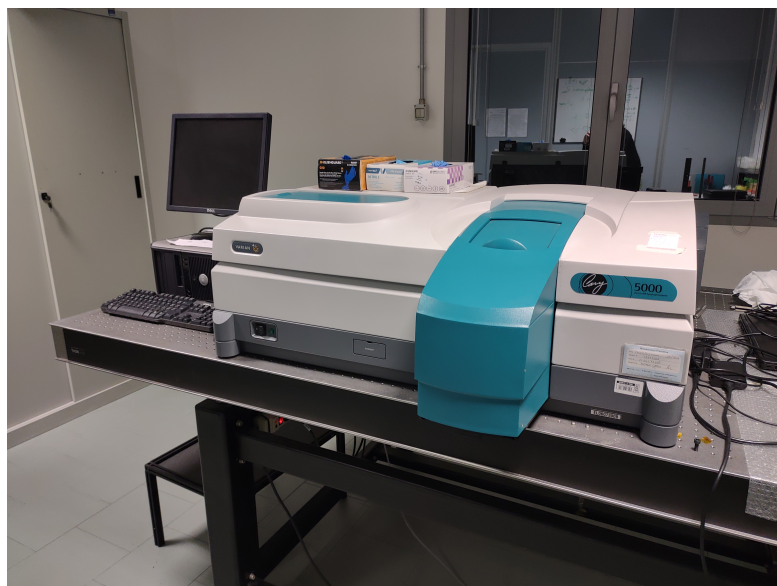

Figure 5.4: *Varian Cary 5000*.

FUNDAMENTALS OF SPECTROSCOPY

In optics, spectrophotometers usually consist of a diffraction grating, which is able to fully characterize the spectral response of the medium. The diffraction

grating can be a reflective surface with parallel grooves repeating periodically in one direction with a specific grating period Λ. Such structure diffracts the incoming radiation in different beams propagating with distinct angular directions. Let's consider an impinging plane wave with wavelength $\lambda \ll \Lambda$, travelling with an incoming angle θ_i with respect to the propagation axis normal to the grating surface, the incident plane wave gets converted into several plane waves at angles θ_q satisfying the *grating equation*

$$sin\theta_q = sin\theta_i + q\frac{\lambda}{\Lambda} \tag{5.1}$$

hence, it is immediate to notice that the diffracted angles θ_q depend on the frequency of the impinging radiation [7].

A reflection grating is called a monochromator when it works as a narrowband filter: starting from a polychromatic, the output can be tuned to a specific wavelength λ. In the case of *Varian Cary 5000*, a double monochromator with a Littrow configuration gets employed. This specific setup implies to choose the first grating orientation so that the incident and diffracted angles are equal. Using a double monochromator helps reducing stray light and increasing the signal-to-noise ratio [50].

For measuring the hemispherical reflectance (specular reflectance + diffuse reflectance) of the samples, a DRA, also known as integrating sphere, has been used. Such device is hollow and its internal surface has been designed as a non-selective diffuse reflector, so that combined with its specific geometry, the majority of the reflected radiation gets collected by the detector. Moreover, the integrating sphere offers options to both include or exclude the specular reflectance component of light, then it is possible to choose between total reflectance and diffuse only reflectance. The reflectance of the DRA over the entire spectrum is of 98%. Finally, the detector is positioned inside the sphere on the top of it and the impinging angle is of 3°20'deg/d. In the UV-Vis portion of the spectrum the detector employed is a Photo Multiplier Tube (PMT) whereas in the NIR region a Indium Gallium Arsenide (InGaAs) detector is used. A schematic representation of the apparatus is shown in Figure [5.5]. The measure is performed at normal incidence by mounting the sample on the outer wall of the sphere, positioned so that the highest portion of the total reflected radiation gets collected. The spectrophotometer measurements are yielded with a 2%
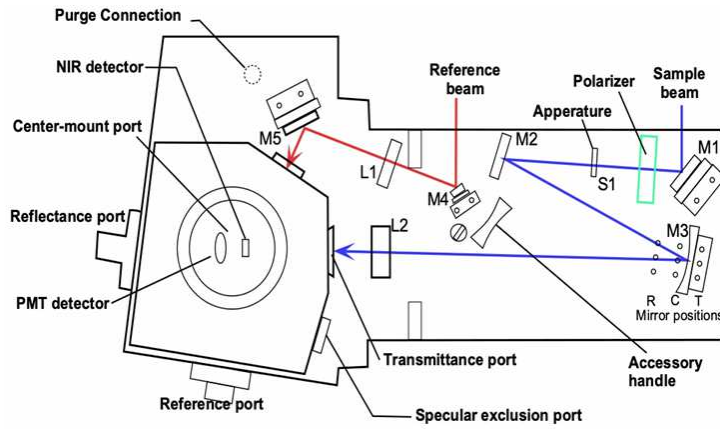
precision accuracy [48].

Figure 5.5: DRA optics and beam path [51].

OPERATION PROCEDURE

The machine has been turned on for over 90 minutes before starting with the preliminary acquisition of the baseline, in order to guarantee stability of the internal light source components. Once the spectrophotometer was ready, the operational steps that were performed are summarized below.

- **Scan → setup**:

  - Setting the *wavelength range* from 250nm to 2650nm and the *Y-mode*: %R
  - *Options → slit height*: reduced
  - *Baseline →* baseline correction
  - *Auto store →* storage off

- **Scan → baseline acquisition**:

  Before taking the measurements of the samples, one has to run the 100%R baseline correction. Then after positioning the reference sample, the baseline gets collected.

- **Scan → Start**:

  Mounting the sample and measuring the spectrum. The yielded quantity is

  $$\frac{R_S}{R_{100\%Baseline}} \tag{5.2}$$

60

expressing the ratio between the sample beam and the reference beam with and without the sample. For each sample more than one acquisition was taken, by rotating the sample of more or less 45° for each measurement in order to check the uniformity of the surface. All the reflectance curves taken were saved and finally post processed with MATLAB.

From the `.csv` file obtained for each sample, the columns with the reflectance acquisitions get extracted, as well as the wavelength range vector. In order to ensure statistical reliability and reduce the noise of the acquisitions, the different reflectance curves related to the same sample have been averaged. Then after having removed the reflectance of the reference sample, the absolute reflectance of each of the sample is obtained. Moreover, a further correction has been applied to the reflectance curve: when the machine arrives at 800nm, the optics changes causing possibly spurious artifacts in the curve.

Afterwards, the solar-weighted hemispherical reflectance was calculated by normalizing the absolute reflectivity of each of the samples for the solar spectrum, according to the international standard *ASTM-G173* [20]. Let's define $\rho_{\lambda,h}(\lambda, \theta, h)$ the average hemispherical reflectance spectrum measured for each of the samples, where accordingly to the theory introduced in Chapter (2), ϕ has been substituted by h to highlight the fact that the quantity depends on the positive hemisphere for the calculations. Moreover, let's introduce other necessary quantities, such as $E_{e,\lambda}^{sun}(\lambda)$ the solar irradiance spectrum (Section (3.1.2)) for $\Delta\lambda$ the wavelength intervals, $\theta = 90°$ is the incidence angle and the wavelength interval used for the solar spectrum integration is $\Delta\lambda = 1$nm, therefore an interpolation of the provided ASTM-G173 standard has been made in order not to discard any of the data that was collected. For measuring the optical performances of the samples, the average of the solar-weighted hemispherical reflectance $\rho_\lambda([SW, Vis], \theta, h)$ has been calculated for the entire solar spectrum, denoted as SW, ranging between 280nm to 2650nm and in the visible part of the spectrum, denoted as Vis, ranging from 380nm to 750nm. This quantity was calculated as follows

$$\rho_\lambda([SW, Vis], \theta, h) = \frac{\sum_{\lambda,h} \rho_\lambda(\lambda, \theta, h) \cdot E_{e,\lambda}^{sun}(\lambda) \cdot \Delta\lambda}{\sum_\lambda E_{e,\lambda}^{sun}(\lambda) \cdot \Delta\lambda} \tag{5.3}$$

61

5.2.2 Cary 630 FTIR

For completing the characterization of the samples over the IR region of the spectrum going from $2.5\mu m$ to $\sim 15\mu m$, corresponding to $4000cm^{-1}$ to $650cm^{-1}$, a FTIR apparatus equipped with an ATR tool has been used (Figure (5.6)).
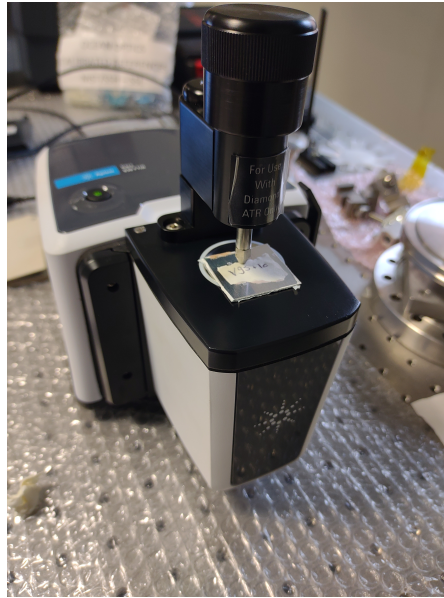

Figure 5.6: *Cary 630 FTIR* spectrometer with ATR tool.

The Fourier-transform infrared spectroscopy derives its name from the Fourier transform process necessary to convert the collected interferogram into the final spectrum. An interferometer generates an interferogram by varying the path length of one beam relative to another. Then the data collected gets mathematically transformed using the Fourier transform to produce the actual spectrum, yielding the sample absorption characteristics across the IR region.

This ATR tool exploits the physical properties of light at the interface between two media with different refractive indices. As light propagates from a optically denser medium with refractive index n_1 to one with lower density with refractive index n_2, i.e. $n_1 > n_2$, it undergoes total internal reflection at the interface between the two media. Such phenomenon takes place only if the impinging angle is at least the *critical angle*, which is defined as

$$\theta_c = sin^{-1}\left(\frac{n_1}{n_2}\right) \tag{5.4}$$

where, in this specific case of study, n_1 refers to the ATR module and n_2 to

the sample. This condition implies the generation of an evanescent wave at the interface. This means that the active power of the impinging beam is not transmitted but it gets completely reflected in the medium of incidence and the intensity of the evanescent field in the sample is non-zero but decays rapidly along the z-axis [7]. Assuming the incident wave to be a Transverse Electric (TE) wave, the magnitude of the electric field in the transmission medium is expressed as:

$$E = E_0 \cdot e^{-\gamma z} \tag{5.5}$$

where E_0 is the intensity of the impinging radiation, γ is the evanescent wave decay coefficient and z is the distance from the interface between the two media. Moreover, it has been shown that most of the organic compounds show weak absorption effects [52], hence under these assumptions the reflectivity gets expressed as

$$R = \frac{|E|^2}{|E_0|^2} = \frac{I}{I_0} = |r|^2 = 1 \tag{5.6}$$

Furthermore, the transmission gets defined as

$$T = e^{-\alpha \cdot d} \tag{5.7}$$

with α the absorption coefficient and d is the sample thickness. Exploiting this expression, one can rewrite the reflectivity of a weakly absorbing medium as

$$R = e^{-\alpha \cdot d_e} \approx 1 - A \tag{5.8}$$

with d_e being defined as an *effective* thickness at which the same absorbance A from transmissions is obtained for internal reflection [53].

Specifically, the tool used is the *Single Reflection Di-ATR module*: the single-reflection diamond ($n_1 = 2.4$ at $1000 cm^{-1}$) has a 1mm diameter sampling surface with $200 \mu m$ active area which slightly protrudes above the metal mounting plate and it provides approximately $2 \mu m$ depth penetration for infrared energy at $1700 cm^{-1}$.

OPERATION PROCEDURE

After mounting the ATR module and opening the dedicated software (*Agilent MicroLab PC Software*), the specific method of acquisition is selected: "ATR absorbance". The preliminary setting of the background is performed, acquiring
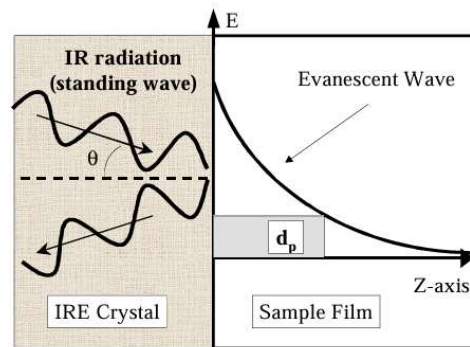
Figure 5.7: ATR functioning principle: generating an evanescent wave at sample-Di interface due to total internal reflection (d_p expresses the penetration depth at which the the transmitted electric field decays to $1/e$) [53].

the baseline profile of a reference sample, which it has been chosen to be gold (Au) since its behaviour is well known. In this way, it is possible to factor out any anomalies occurring both in the background and sample spectrum. Afterwards, the spectra of the samples were acquired, by ensuring each time that the surface of the FTIR-ATR was clean by using some acetone with a non-abrasive wipe. The best contact between the diamond and the sample has to ensured for the previously described reflection theory to hold. In fact, if the sample is not well positioned, an air gap may form, introducing another interface between the ATR module and the sample, invalidating the collected spectra. For this reason the ATR module is equipped with a clamping mechanism helping achieving the closest contact between diamond and sample applying a constant pressure for all the acquisitions. For each sample, three measurements were taken by rotating it of 45° each time.

The acquisitions were yielded in `.asp` files containing just the absorbance values of the samples. Hence, the x-axis of the plot has to be manually generated in MATLAB. Moreover, for ensuring statistical reliability and reduce the noise of the acquisitions, the curves related to the same sample have been averaged.

5.3 Morphological Characterization

5.3.1 Zeiss Optical Microscope

The images of the surfaces of the samples have been acquired with the *Zeiss AXIO Lab A1* optical microscope exploiting two different magnifications: 50x and 100x, offering a Numerical Aperture (NA) of 0.75 and 0.8, respectively. Moreover, the system comes with an adjustable Light Emitting Diode (LED) illumination, providing consistent and even lighting across the sample surface for achieving high-quality images.

Figure 5.8: *Zeiss AXIO LabA1* Optical microscope.

Operation Procedure

After opening the dedicated software, *AXIO Vision*, one sample at a time gets positioned on the mounting plate and, after being focused, thanks to the X-Y Mechanical Stage, one can look for the most appropriate zone by moving the sample with a range of 75mm×30mm. For each of the samples, eight pictures have been acquired (four for each magnification) and the specific focus depths will be reported in the next chapter. The instrument allowed the observation of

the surfaces at different focus depths, highlighting the various features of the samples.

5.3.2 AFM NX-10

AFM NX10 uses a micro-machined cantilever with a sharp tip to measure a sample's surface [54]. The functioning of such metrology instrument lays in the attractive and repulsive forces between the measured sample and the tip of the cantilever.

When the tip is in air, a laser will hit the center of the quadrant photodetector.
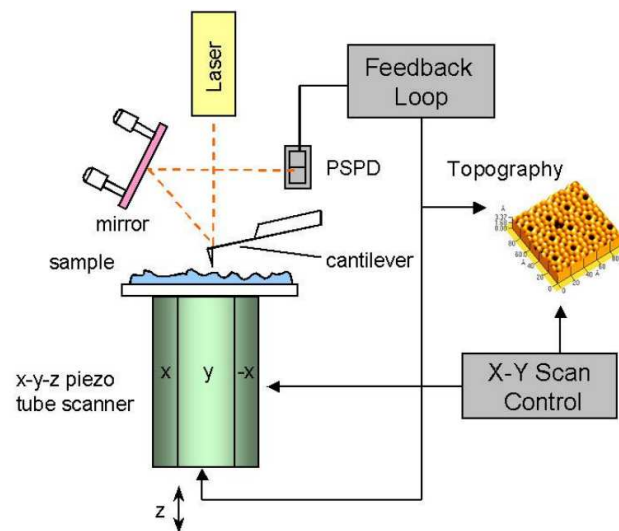
Figure 5.9: Diagram of basic functioning of AFM NX10 scanning [54].

If the tip encounters a feature on the surface, it deflects and the laser will move on such quadrant. The tube-shaped piezo scanner controls the tip and adjusts its vertical position so that the laser is always in the center of the photodetector, hence keeping a constant distance between the tip and the sample surface. By keeping track of the motor height position one can extract the topography of the surface.

OPERATION PROCEDURE

The AFM was operated in *Non-Contact* mode, i.e. the tip does not touch the surface but oscillates at a very small distance to the sample detecting Van Der Waals forces, over a scan area of the sample of $70\mu m \times 70\mu m$. The post processing of the captured image was performed using *Gwyddion* software.
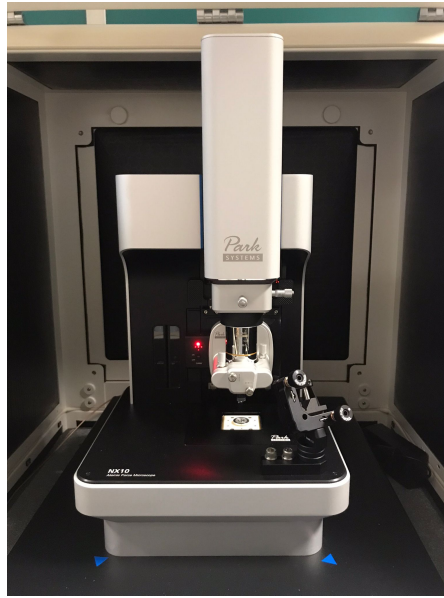
Figure 5.10: Atomic Force Microscope *Park NX-10*.

5.3.3 Tesa Digit-Cal

The samples of which the thicknesses have been measured are V95 and S90, the two substrate coated by ThermoShield (1 coat), i.e. 3F and 4F, the case with ThermoShield and IM30K glass bubbles (1 coat), i.e. V95+3F and S90+3F, and subsequently the other samples on both substrates with the different numbers of paint (ThermoShield and glass bubbles) coats and the Celgard layer on top. The thickness of the samples has been measured with a caliber *Tesa Digit-Cal 05.30080* which has a resolution of 0.01mm and an accuracy of ±0.02mm.

67

5.4 TEMPERATURE AND COOLING POWER MONITORING APPARATUS

The experimental setup for outdoor measurement was completely built by the staff of the University of Florence, hereinafter one can observe the apparatus and the corresponding scheme in Figure (5.11).
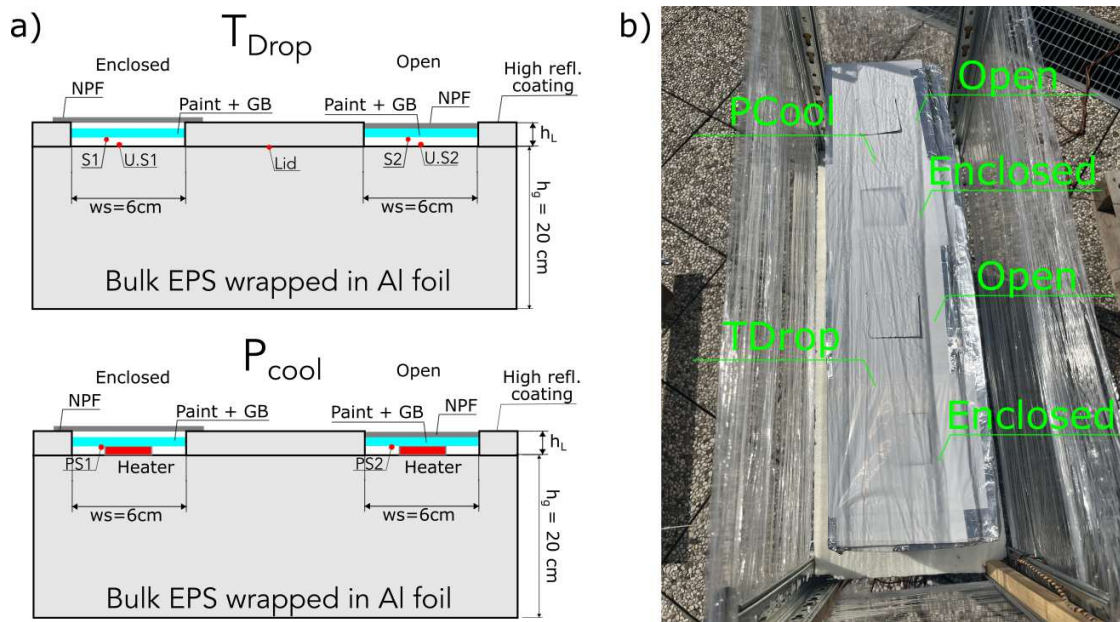
Figure 5.11: a) Outdoor experimental setup identifying the test areas and conditions. b) Schematic of a section of the sample holder.

The board employed in the experimental setup consists of a T_{drop} shield that allows measuring the temperature for multiple samples via Negative Temperature Coefficient (NTC) thermocouples model 103JT-025 of 10kΩ [55]. Moreover, the ambient temperature T_{amb} and relative humidity is measured using a DHT22 sensor [56]. The accuracy of these sensor modules is ±0.5°C for the temperature and ±2% for the relative humidity. The solar irradiance and the apparent sky temperature are measured using a BH1750 light sensor [57] and an IR sensor [58], respectively. The cooling power P_{cool} shield is equipped with NTC probes as well and a Proportional Integral Derivative (PID) system which menages the warm-up of the samples to the setting point temperature, that usually is the ambient temperature T_{amb}, through the control of a resistive heater.

The apparatus, which is sketched in Figure (5.11), will be described in the following lines. The temperature sensors are placed inside the sample holder which is

covered in Al foil to prevent radiative heating and its base is made of Expanded Polystyrene (EPS) of dimensions $20\text{cm} \times 14\text{cm} \times 75cm$ (height × width × length) for guaranteeing thermal insulation from the surrounded area. Four $6\text{cm} \times 6\text{cm}$ samples are placed in the sample holder, equidistant from one an other. They are kept into place thanks to a lid made of EPS of height 0.5cm, four holes to let the samples be in contact with the environment and covered of highly diffused reflective tape by 3M.

Moreover, the whole apparatus is surrounded by PE walls to helping prevent further radiative heating related to direct wind. Finally, the ambient temperature T_{amb} gets monitored by placing one of the three NTC inside a professional Polyvinyl chloride (PVC) Stevenson Screen (*Davis 7714 passive radiation shield* [59]) [38].

The board allows to measure simultaneously T_{drop} and P_{cool} by using a pair of
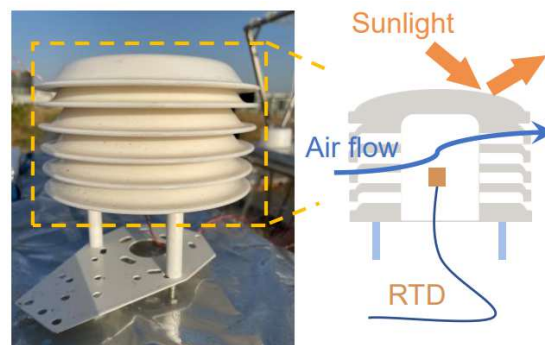
Figure 5.12: Picture and schematic illustration of a Stevenson screen [34].

identical samples in parallel, allowing the comparison of the behaviours of the different samples employed for passive radiative cooling [60], [38]. Moreover, the for better accuracy and regulation of the measured quantities related to temperature and solar irradiance, reference data are used. The latter are from the weather station operated by the LaMMA consortium (Laboratory di Monitoraggio e Modellistica Ambientale) between the National Research Council of Italy (CNR) and the Tuscany region [61].

Stevenson Screen

A Stevenson screen is a meteorological screen designed to protect instruments from precipitation, direct solar radiation and radiated or reflected heat sources, while allowing free air circulation. This device creates a controlled

environment that closely mirrors the external air conditions. It is usually employed to house different instruments that measure temperature and humidity, helping maximizing the accuracy of sensor readings [59].

OPERATION PROCEDURE

The outdoor measurements were performed on the samples with three coats of paints on V95 substrate, i.e. V95-3F-3C. Two different variations have been compared: the first one being the sample with the PP-PE-PP layer directly put on top of the sample and for the second one the Celgard layer has been put on top of the coating as a separate convection shield.

Two configurations were used for T_{drop} and P_{cool} measurements. The first one, labeled as *S1*, the Celgard layer has been used as external convection shield, placed on top of the slot of the sample, for protecting the latter from external air. In the second configuration, labeled as *S2*, the Celgard was directly applied to the painted samples (as described in Section(5.1)), hence the air is free to flow in and around the surface slot. The NTCs for temperature measuring were placed both underneath and directly in contact with the substrates, whereas for the measuring of P_{cool} the NTCs and the heaters are placed directly in contact with the samples.

Let's notice that additional NTCs were added to control that the EPS sample holder will not overheat during the process, since it could interfere with the spontaneous cooling of the samples.

6
Results and Discussion

6.1 Optical Characterization

The samples have been optically characterized by means of the instruments presented in Chapter (5), namely the spectrophotometer for the characterization in the range between 250nm to the NIR at 2500nm (Section (5.2.1)), and the FTIR-ATR for the IR part of the spectrum from 2.5μm to 15μm (Section (5.2.2)).

The characterization of the first set of samples (Table (5.1) and (5.2)) was crucial for the development of the second part of the experiments. In fact, the candidates displaying a better performance in terms of solar spectrum reflectance, were selected for constituting a second set of optimized samples (Table (5.3)).
Therefore, knowing the required performances of an effective PDRC coating presented in Chapter (3), the aim that has been set for the first campaign of measurements, was to individualise the samples having a reflectance in the visible part of the spectrum (280nm to 2500nm) strictly above 90%.

In the following tables, namely Table (6.1), Table (6.2) and Table (6.3), the solar-weighted hemispherical reflectance $\rho(SW, \theta, h)$ and the solar-weighted hemispherical reflectance in the visible part of the spectrum $\rho(Vis, \theta, h)$ are reported in the second and third columns. Those quantities are calculated exploting Eq. (5.3)

Among all the samples, the ones that have an average hemispherical reflectance above 90%, apart from the bare substrates V95 and S90, are for the majority the ones deposited on V95 substrate. That is not a suprise since the multilayer structure engineered for this substrate should have yielded an average hemispherical reflectance in the visible part of the spectrum of about 95%, this being confirmed by the experimental results reported in Table (6.1). The same reasoning can be applied to the design of the S90 substrate, which was specifically designed to reflect in average 90% of the incoming visible light. The value obtained experimentally and reported in Table (6.2) is slightly below 90% probably due to the performances degradation due to the oxidation of Al.

Table 6.1: Average hemispherical reflectance $\rho([SW, Vis], \theta, h)$ for samples on V95 substrate.

Sample	$\rho(SW, \theta, h)$	$\rho(Vis, \theta, h)$
V95	91.8073%	95.2568%
B	88.7263%	90.7192%
2B	81.2266%	82.3154%
3B	74.6815%	77.4670%
4B	75.4298%	77.2613%
5B	83.9106%	84.9523%
6B	85.7071%	87.0816%
2C	86.0210%	87.0027%
3C	86.1604%	87.1422%
1A	84.5150%	86.8883%
3A	87.2518%	88.7362%
1F	84.2723%	88.8770%
2F	85.7179%	89.8940%
3F	87.8334%	91.3546%
4F	88.4978%	91.8804%
3M	92.0928%	94.3530%

Table 6.2: Average hemispherical reflectance $\rho([SW, Vis], \theta, h)$ for samples on S90 substrate.

Sample	$\rho(SW, \theta, h)$	$\rho(Vis, \theta, h)$
S90	88.1817%	89.4624%
1G	86.3761%	85.1805%
2G	80.7354%	79.6397%
3G	85.9439%	86.3386%
4G, 4G$_{BIS}$	78.681%, 80.7446%	78.7067%, 80.3743%
5G, 5G$_{BIS}$	81.369%, 77.7184%	81.0867%, 75.6267%
6G	81.9781%	81.2657%
7G	86.9561%	87.6560%
8G	89.5029%	90.7009%

Table 6.3: Average hemispherical reflectances $\rho([SW, Vis], \theta, h)$.

Sample	$\rho(SW, \theta, h)$	$\rho(Vis, \theta, h)$
V95-3F	88.2238%	88.9489%
V95-3F-1C	92.4574%	93.8463%
V95-3F-2C	93.0595%	94.9707%
V95-3F-3C	93.7159%	95.8515%
V95-3F-4C	92.9239%	94.9967%
S90-3F	88.6703%	91.3006%
S90-3F-1C	86.2295%	87.9609%
S90-3F-2C	90.8850%	93.1715%
S90-3F-3C	93.6029%	95.7346%
S90-3F-4C	93.7337%	95.8318%

The best performances in terms of solar-weighted reflectance are achieved by the samples B, 2F, 3F, 4F and 3M for what concerns the V95 substrate, whereas by the sample 8G for the S90 substrate.

Let's observe that the best among all the performances are yielded by the sample 3M. Unfortunately, this has a peculiar composition which has not been disclosed by the company creating it.

The 3F and 4F samples are coated by respectively one and two coats of Thermoshield paint, which is a commercial solvent-based cooling paint and for more details one can refer to Chapter (5). Whilst the 8G sample consists of a double

hand of a mix of 3M paints with SiO_2 microparticles, specifically 25% of IM30K type and 25% of IM16K type.

Based on these results, the best features of the three aforementioned samples have been combined together for trying to achieve an optimized structure, extensively described in Chapter (5). Moreover, as one can observe from the results obtained on the NPF layer, reported in Figure (6.14), this film strongly reflects light in the UV-Vis part of the solar spectrum. Hence, it can be exploited for increasing the reflectance of the coatings. In fact, by putting the NPF on top of the optimized coating composition would hinder the useless absorption of UV radiation caused by the anti-aging molecules present in the paint composition. Furthermore, the Celgard is a polyethylene layer, hence it is transparent in the IR part of the spectrum. This implies that the sample can spread out the thermal radiation through the NPF. Finally, it is also beneficial for insulating the sample from the surrounding environment, i.e. from convection phenomena.

In Figure (6.15) and (6.16) the reflectances of the optimized samples is displayed. One can observe that increasing the amount of coats of paint is beneficial for the reflectance in the UV-Vis part of the spectrum and lowering it in the NIR region. An interesting result, that can be observed from the experimental data reported in Table (6.3). The latter are graphically represented in Figure (6.1) and one can immediately observe that above the third paint layer, the performances of the PDRC coating become highly independent of the choice of the substrate.

In a second moment, to complete the characterization of the samples in the IR
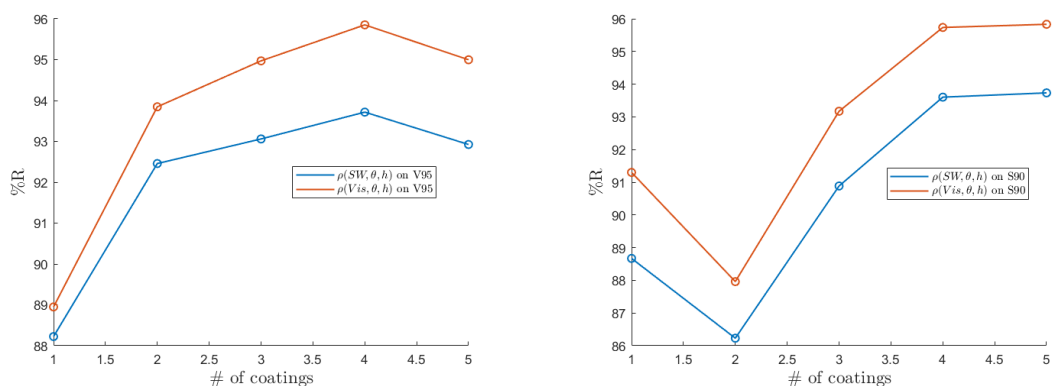
Figure 6.1: Average hemispherical reflectance in the solar spectrum and in the visible part of the solar spectrum as function of the number of hands of paint. On the left the coatings deposited on the V95 substrate and on the right the ones deposited on the S90.

part of the spectrum, FTIR-ATR measurements were performed. This allowed to better understand the behaviour of the coatings in the LWIR region of the spectrum, fundamental for a complete discussion about RC performances of the samples.

Infrared spectroscopy is used to study the molecular structure and the specific composition of the materials. Namely, ATR spectroscopy is a powerful tool for analysing the surfaces of the samples. Such characterization yields absorption peaks related to the specific composition of the materials under study. In fact, when IR light interacts with the material, it may meet resonance conditions, i.e. the molecule absorbs the incoming light and excites the vibrational mode of a molecule, further details in Section (4.1). In IR spectroscopy, there is a one to one correspondence between resonances and absorption peaks, allowing to identify functional groups and chemical structures of the material [62].

As one can observe from figure (6.2), resonances associated to specific molecu-
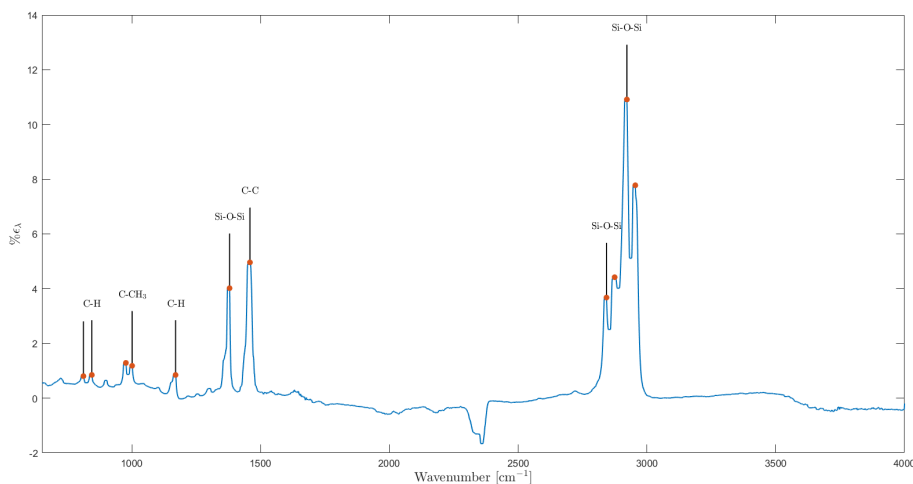
Figure 6.2: FTIR-ATR analysis and individualisation of characteristic chemical bonds of the sample.

lar structures can be observed. The functional groups identifying the NPF are C-CH$_3$, C-C and C-H bonds.

Moreover, in Figure (6.28) one can observe that the Celgard layer displays an overall absorbance (emissivity (2.55)) of less than 10%. Therefore, one can conclude that the use of a NPF as an additional coating would be beneficial for increasing the cooling performances of the sample. In fact, as aforementioned, the NPF layer enhances the reflectance in the UV part of the spectrum, addition-

ally, given its behaviour in the IR, this thin layer would not hinder the material RC performances.

Moreover, in the following pages, the characterizations related to each sample are reported, grouping together the ones that share the same substrates and having correlation in the properties of the coatings painted on top. The first set of images, from Figure (6.3) to Figure (6.16), represent the optical characterization of the samples from the UV-Vis to the NIR, whereas, the second set of images, from Figure (6.17) to Figure (6.28), display their characterization in the IR range.
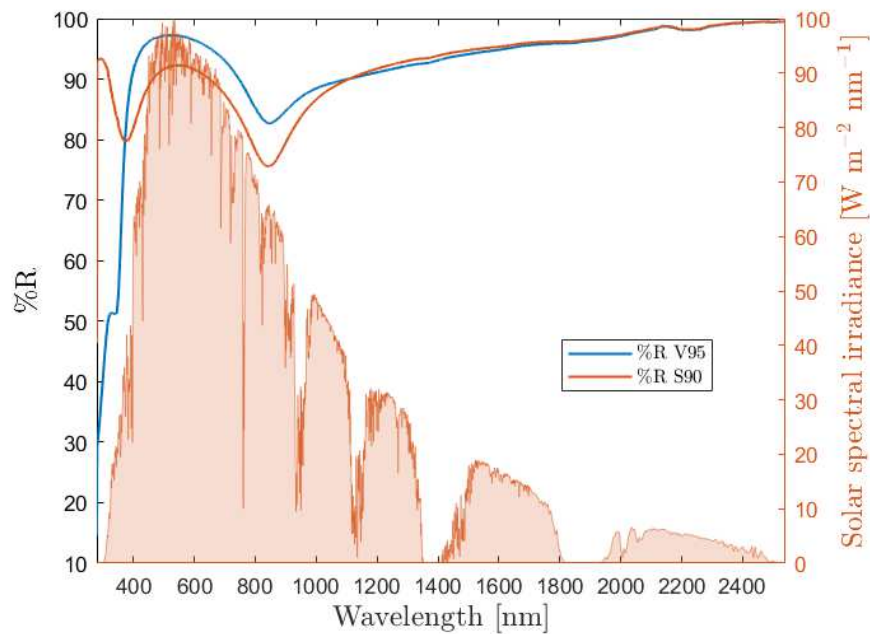
Figure 6.3: Reflectance curves of the substrates V95 and S90.
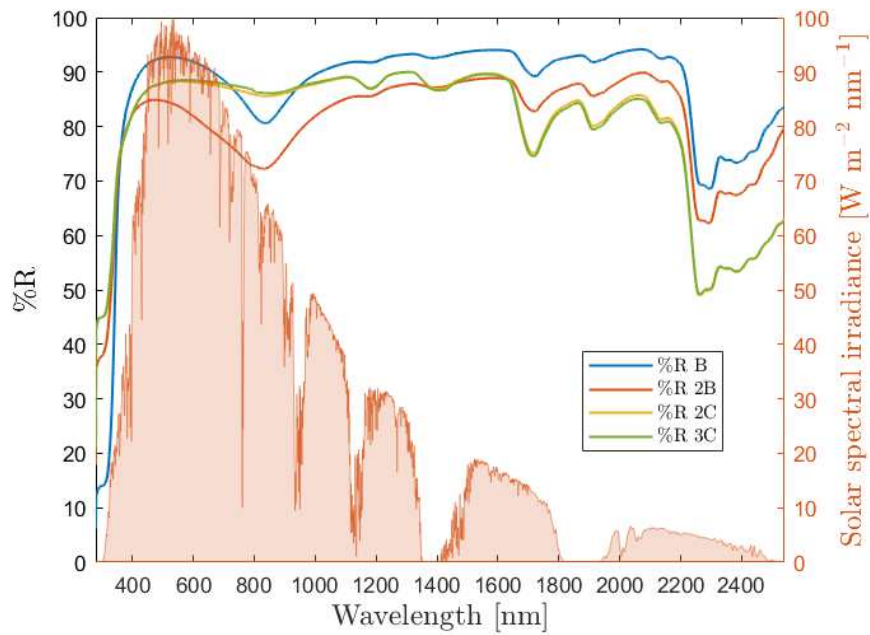
Figure 6.4: Reflectance curves of the samples B, 2B, 2C and 3C.
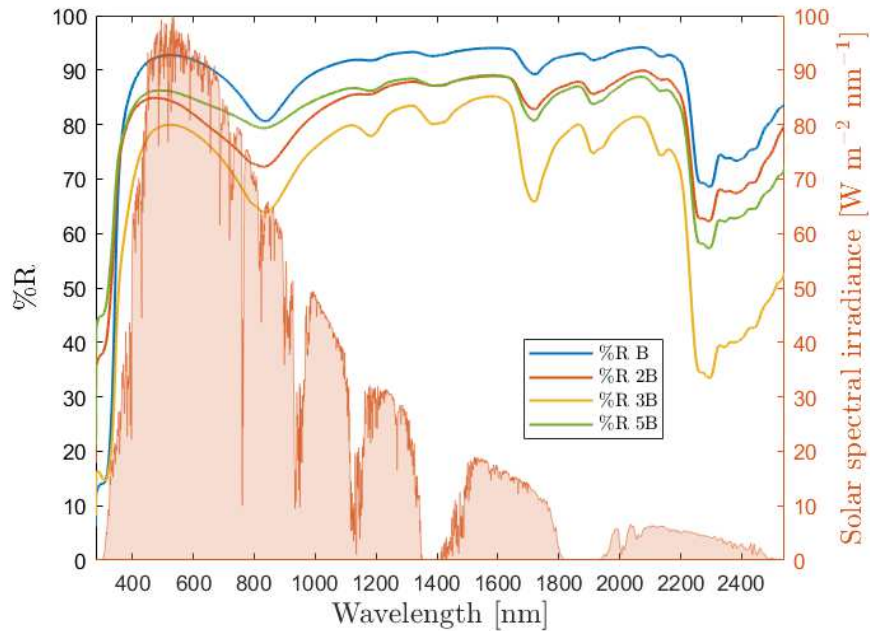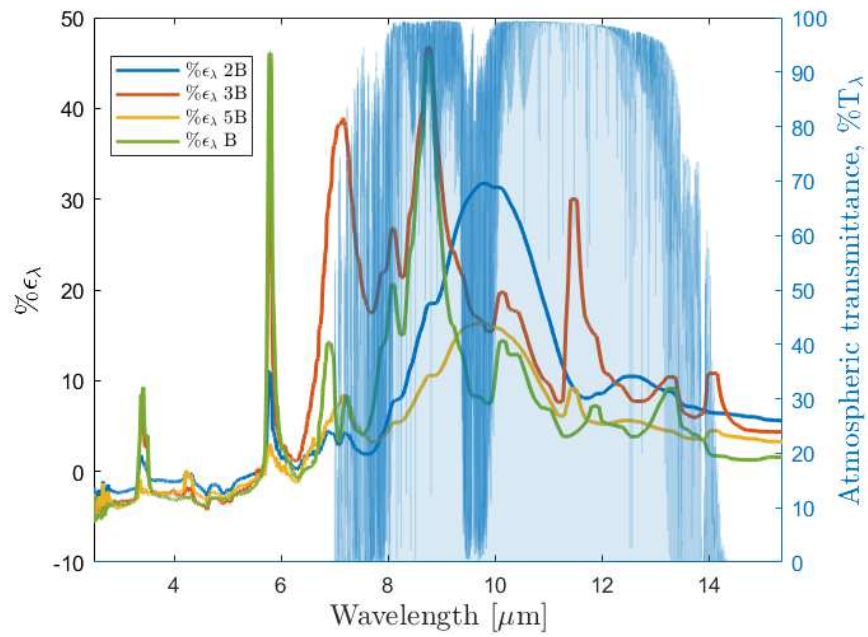

Figure 6.5: Reflectance curves of the samples B, 2B, 3B and 5B.
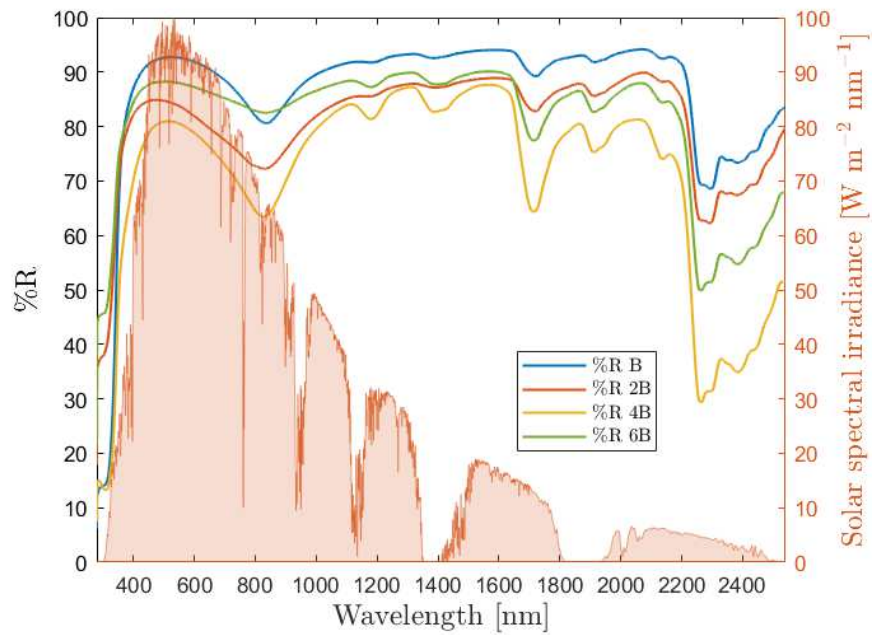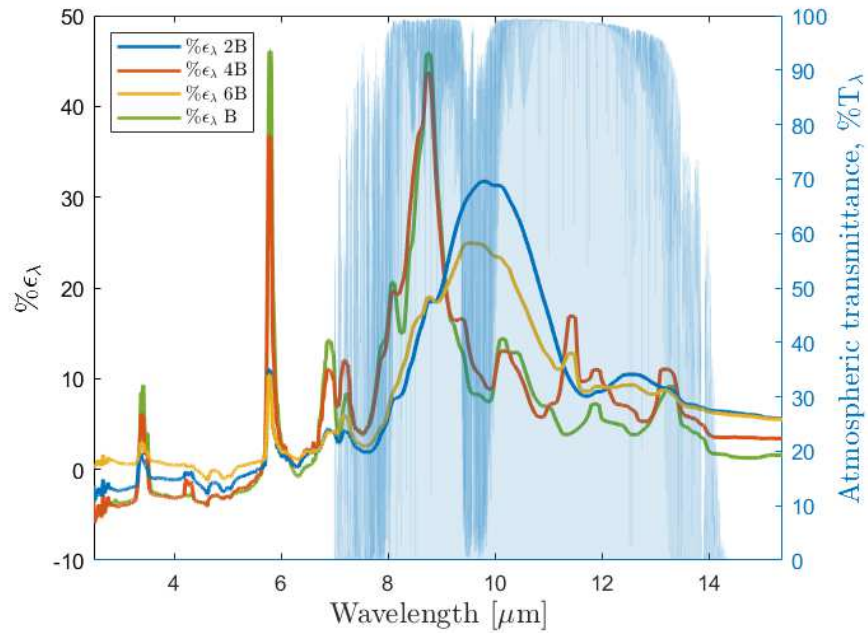
Figure 6.6: Reflectance curves of the samples B, 2B, 4B and 6B.
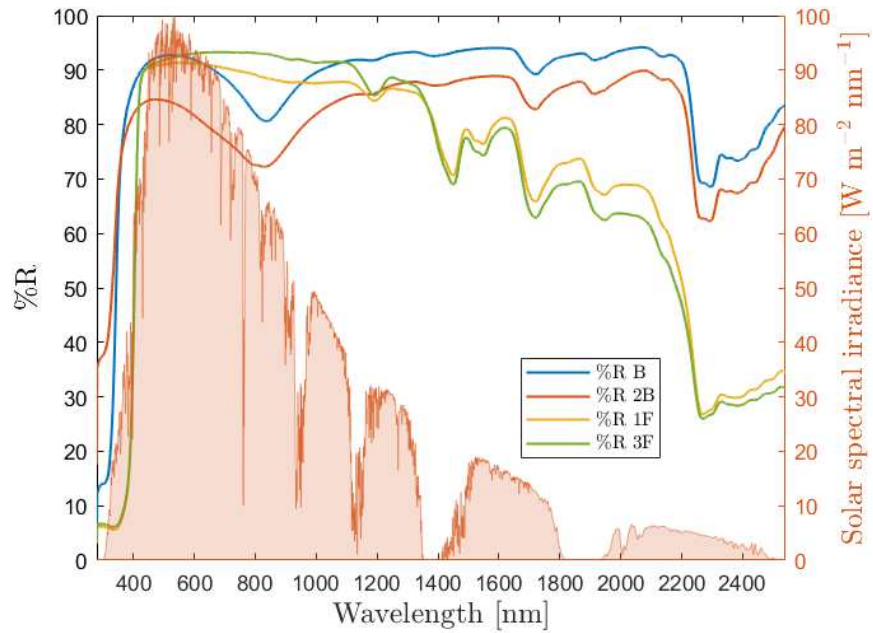
Figure 6.7: Reflectance curves of the samples B, 2B, 1F and 2F.
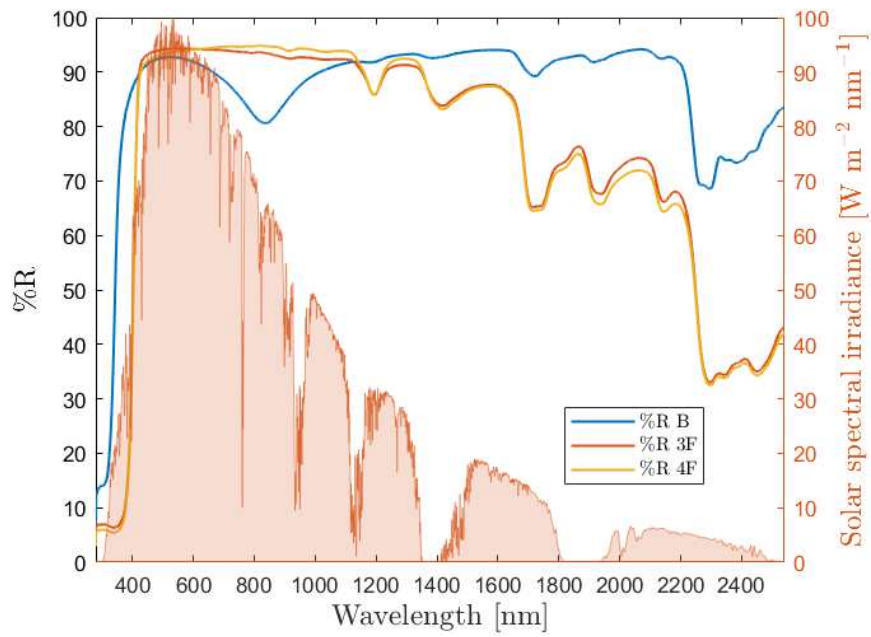
Figure 6.8: Reflectance curves of the samples B, 3F and 4F.
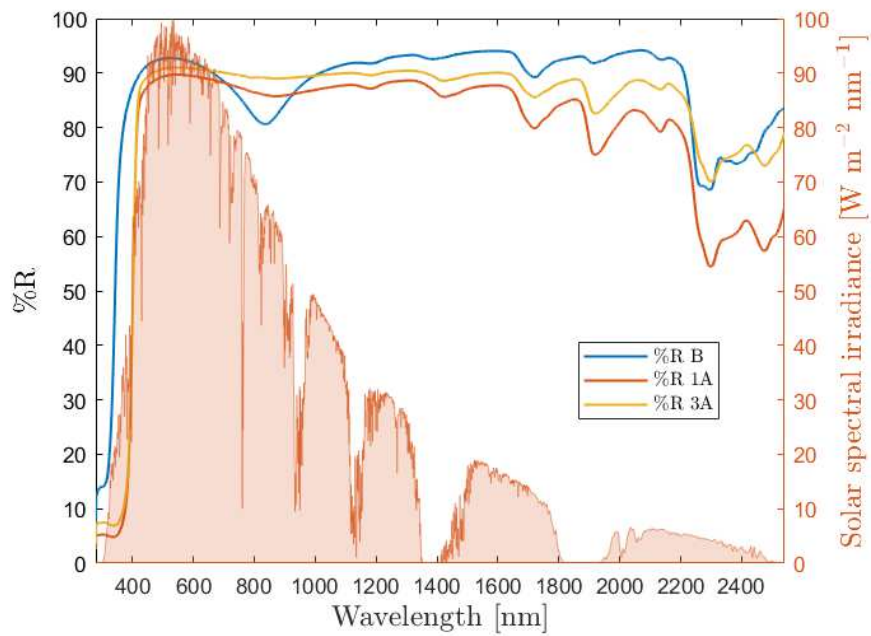
Figure 6.9: Reflectance curves of the samples B, 1A and 3A.
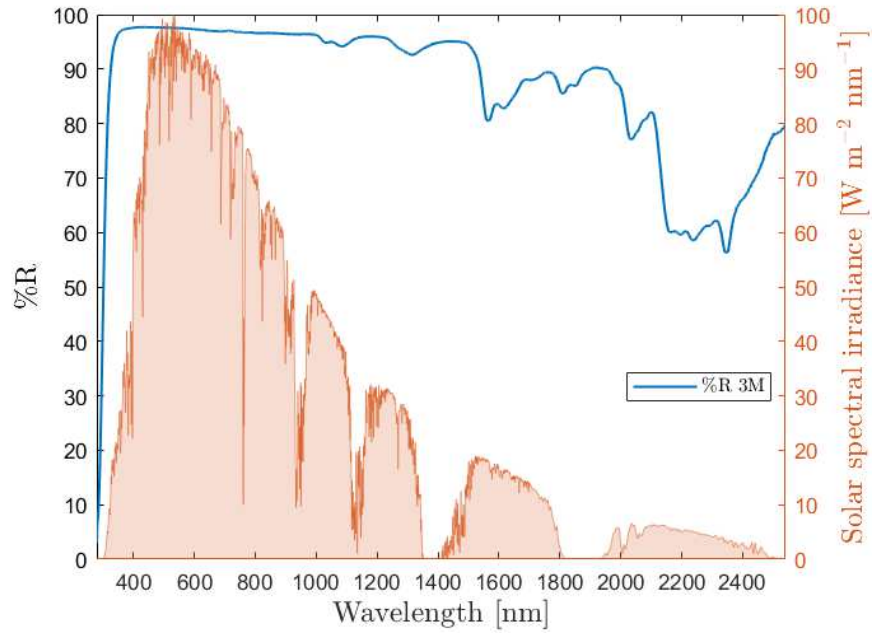
Figure 6.10: Reflectance curves of the sample 3M.
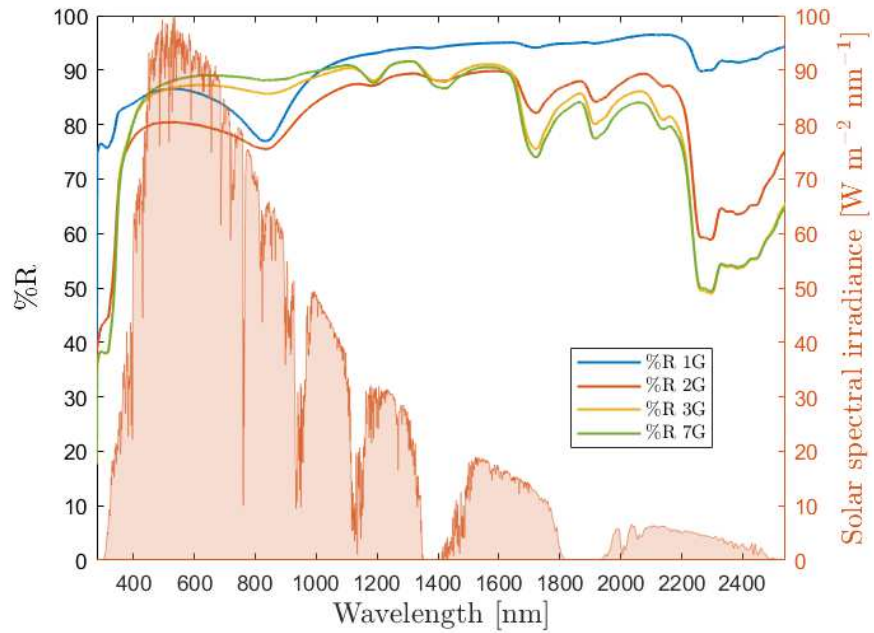
Figure 6.11: Reflectance curves of the samples 1G, 2G, 3G and 7G.
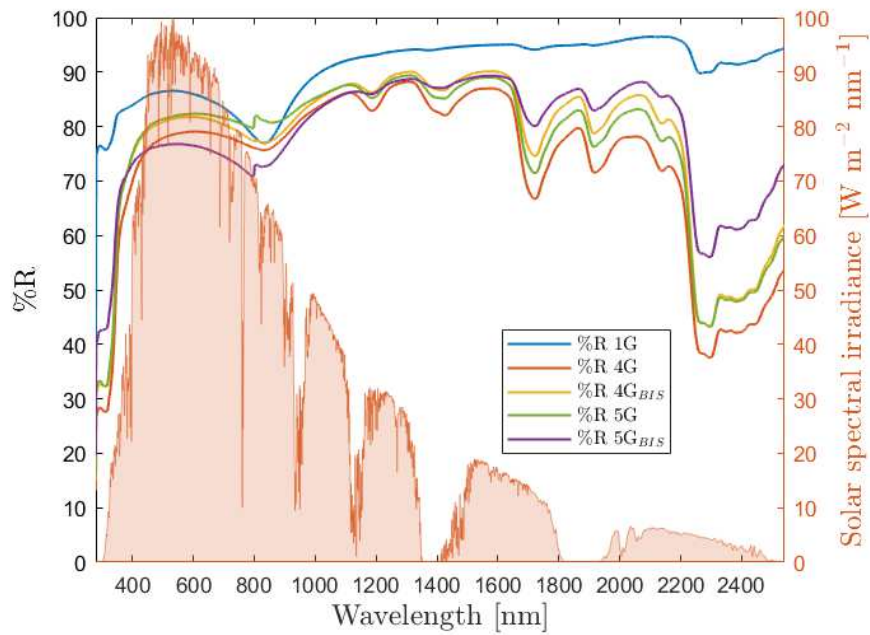
Figure 6.12: Reflectance curves of the samples 1G, 4G and 5G.
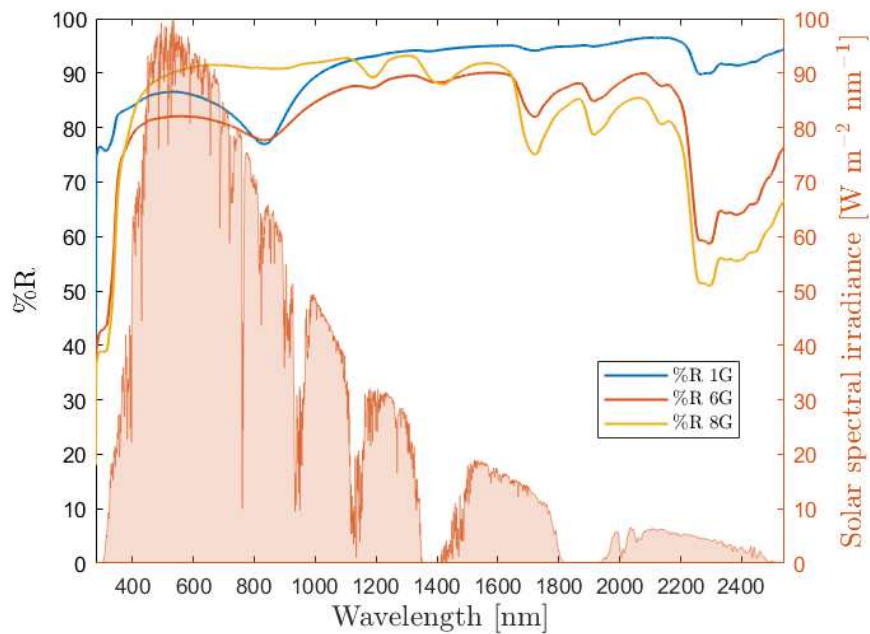
Figure 6.13: Reflectance curves of the samples 1G, 6G and 8G.
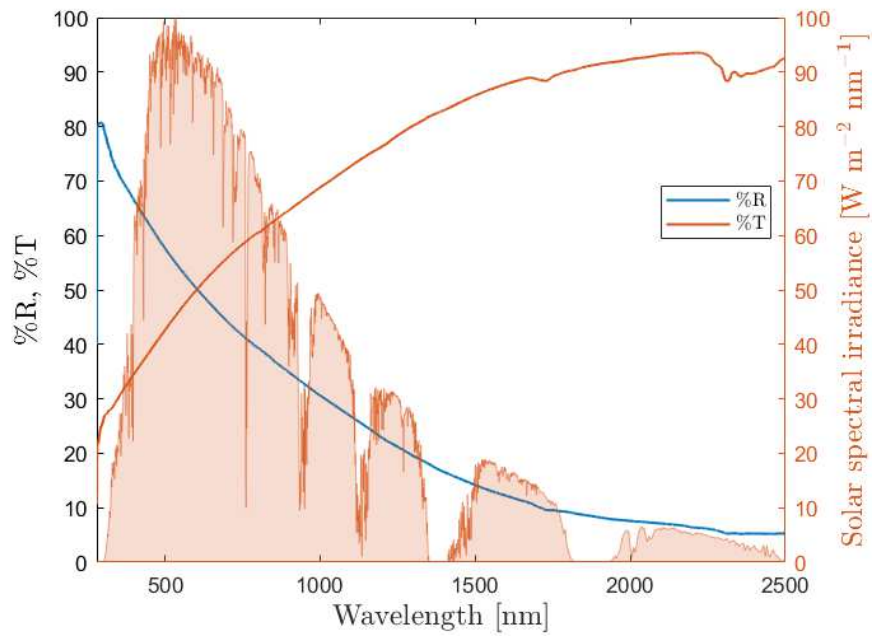
Figure 6.14: Reflectance and transmittance curves of a freestanding Celgard layer.
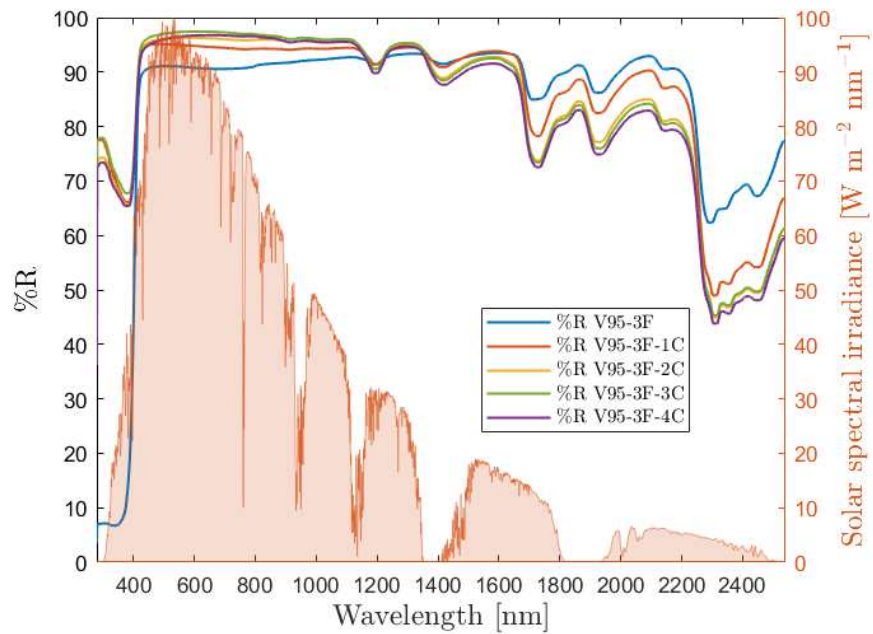
Figure 6.15: Reflectance curves of the samples V95-3F, V95-3F-1C, V95-3F-2C, V95-3F-3C, V95-3F-4C.
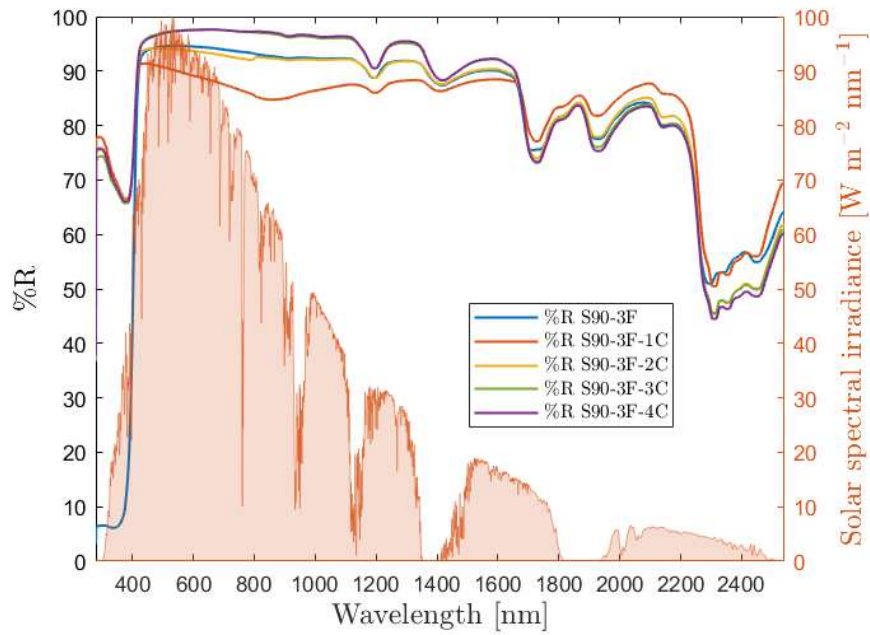
Figure 6.16: Reflectance curves of the samples S90-3F, S90-3F-1C, S90-3F-2C, S90-3F-3C, S90-3F-4C.
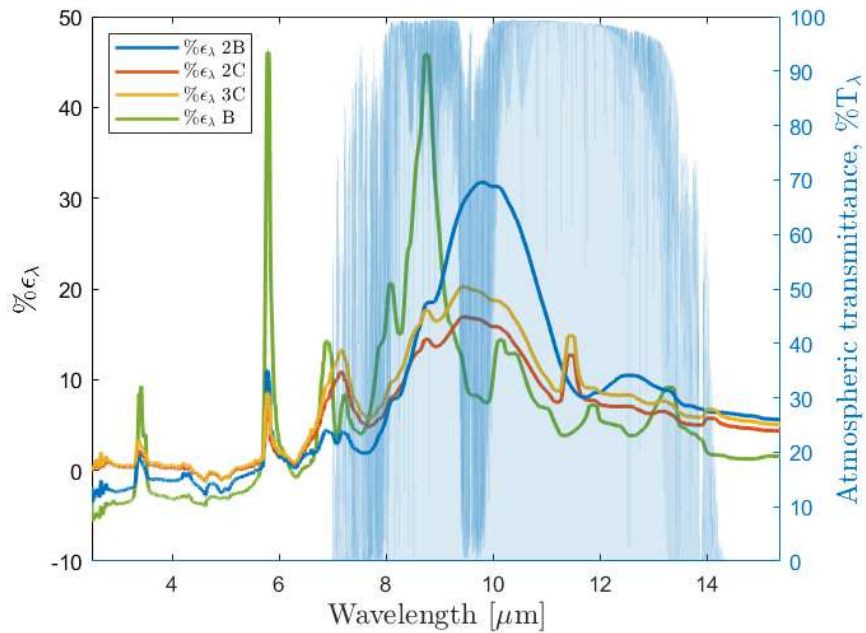
Figure 6.17: Emittance curves of the samples B, 2B, 2C and 3C.

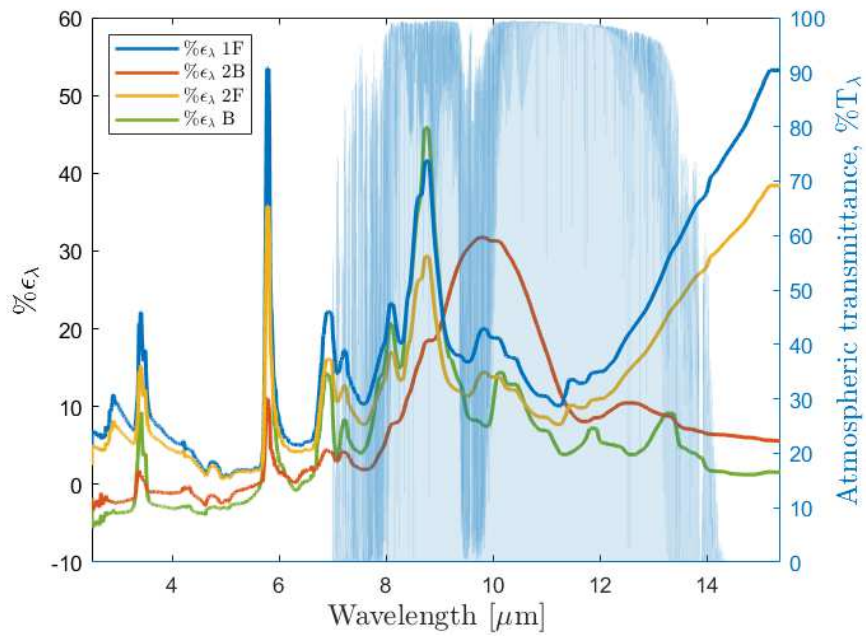Figure 6.18: Emittance curves of the samples B, 2B, 3B and 5B.

Figure 6.19: Emittance curves of the samples B, 2B, 4B and 6B.

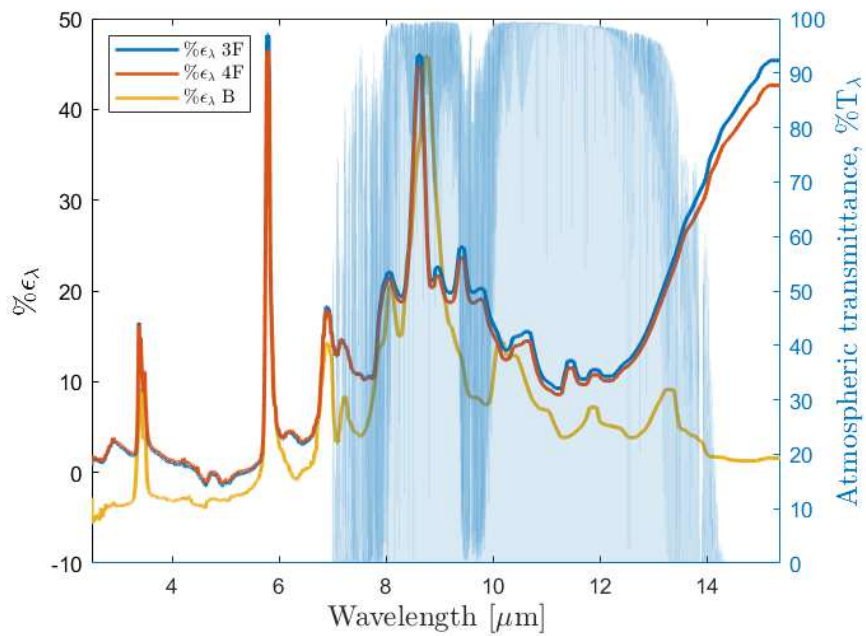Figure 6.20: Emittance curves of the samples B, 2B, 1F and 2F.

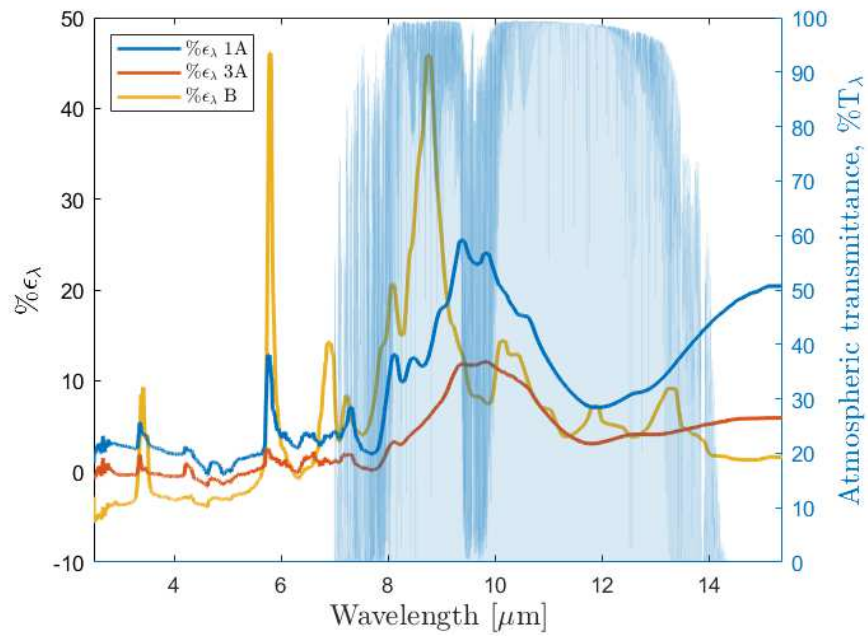Figure 6.21: Emittance curves of the samples B, 3F and 4F.

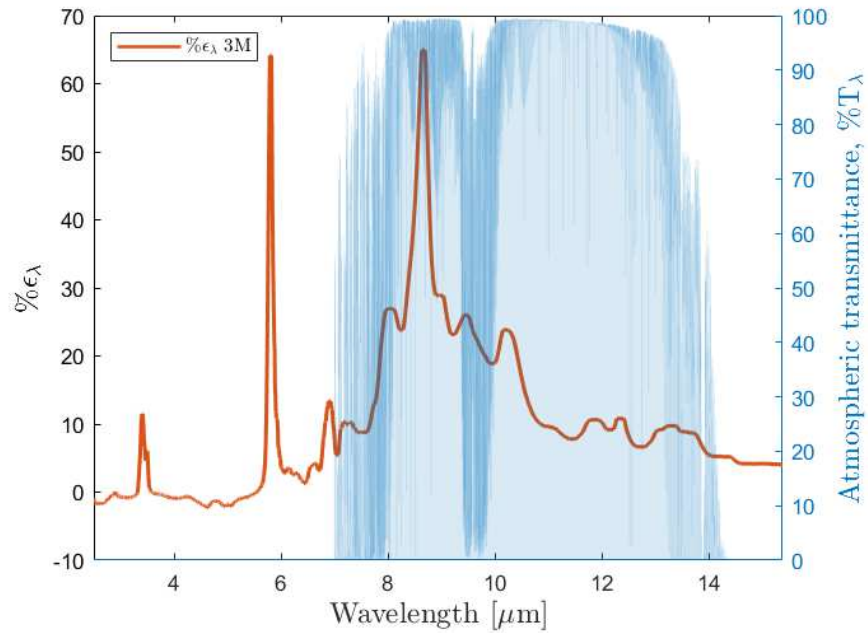Figure 6.22: Emittance curves of the samples B, 1A and 3A.
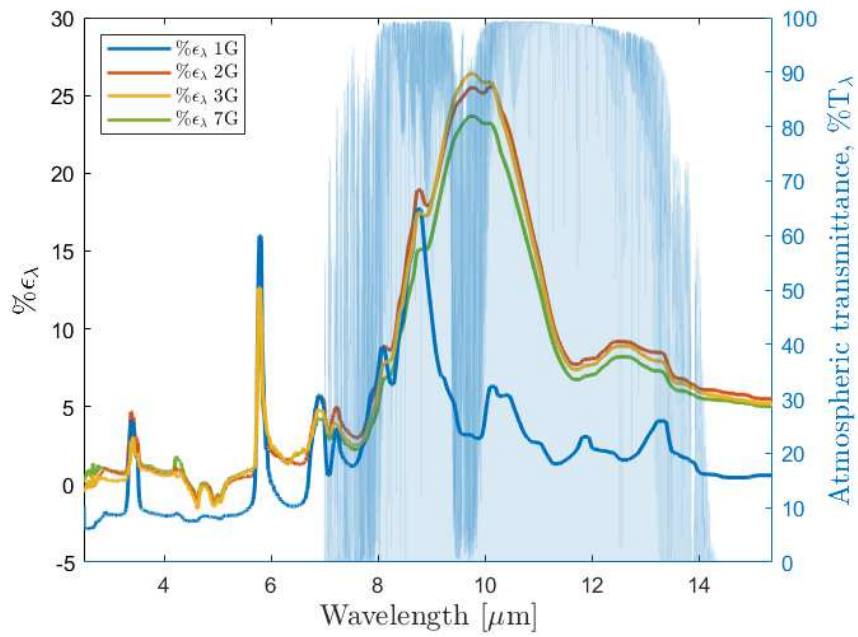

Figure 6.23: Emittance curves of the sample 3M.

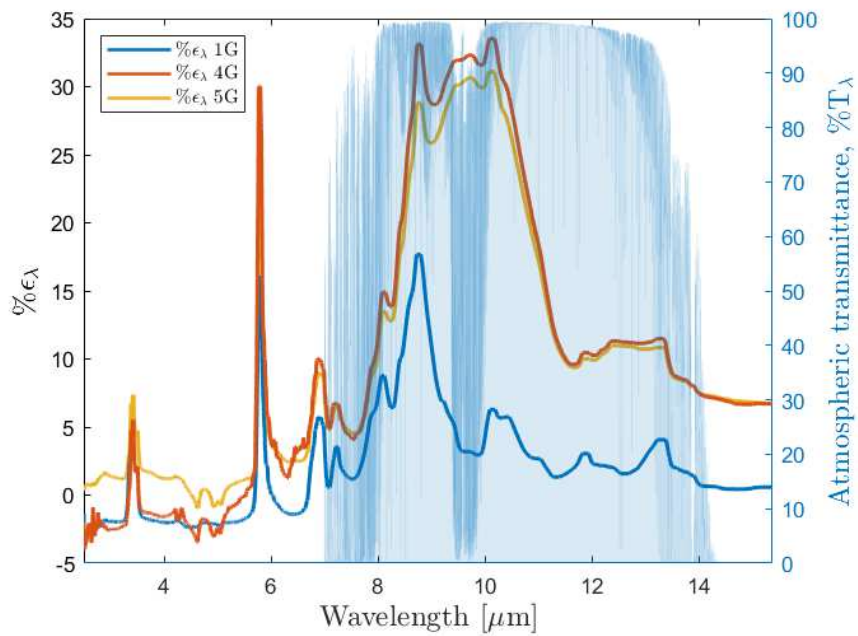Figure 6.24: Emittance curves of the samples 1G, 2G, 3G and 7G.

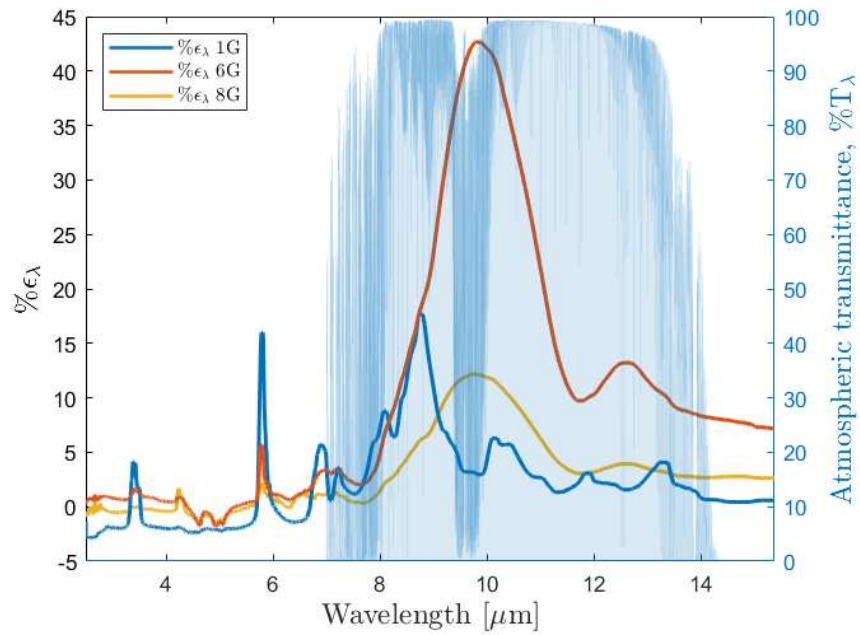Figure 6.25: Emittance curves of the samples 1G, 4G and 5G.

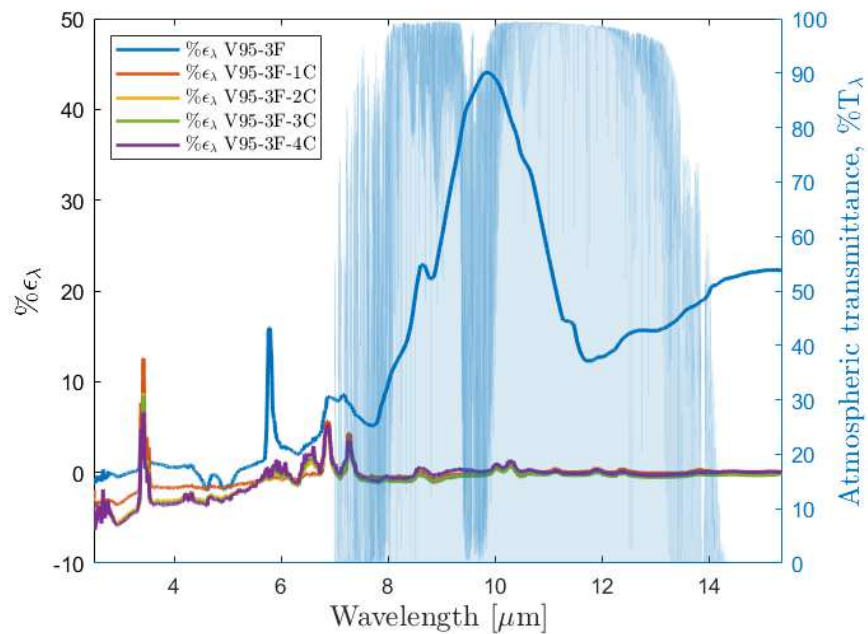Figure 6.26: Emittance curves of the samples 1G, 6G and 8G.

Figure 6.27: Emittance curves of the samples V95-3F, V95-3F-1C, V95-3F-2C, V95-3F-3C, V95-3F-4C.
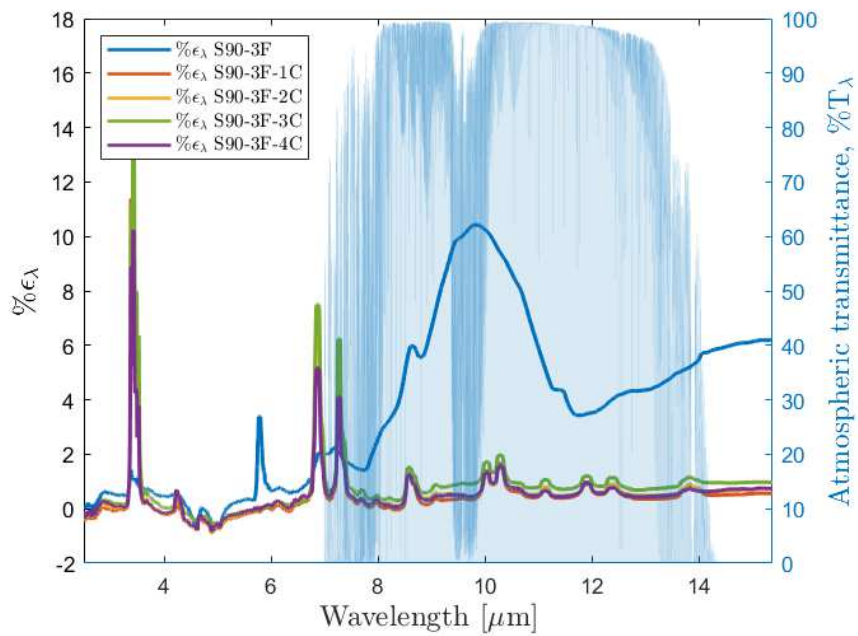
Figure 6.28: Emittance curves of the samples S90-3F, S90-3F-1C, S90-3F-2C, S90-3F-3C, S90-3F-4C.

6.2 MORPHOLOGICAL CHARACTERIZATION

The thicknesses of the PDRC samples were measured with the caliper presented in Section (5.3.3).

Table 6.4: Thicknesses of the optimized samples.

Samples thicknesses				
Sample	d_1[mm]	d_2[mm]	d_3[mm]	d_{avg}[mm]
V95	0.56	0.50	0.54	0.53
3F	0.77	0.84	0.79	0.8
4F	0.88	0.95	0.93	0.92
V95-3F	0.71	0.68	0.64	0.68
V95-3F-1C	0.66	0.67	0.68	0.67
V95-3F-2C	0.87	0.89	0.79	0.85
V95-3F-3C	1.13	0.93	0.95	1
V95-3F-4C	1.27	1.34	1.19	1.27
S90	0.47	0.43	0.44	0.45
S90-3F	0.68	0.63	0.67	0.66
S90-3F-1C	0.65	0.56	0.59	0.6
S90-3F-2C	0.6	0.54	0.66	0.6
S90-3F-3C	1.1	1.16	1.07	1.11
S90-3F-4C	1.40	1.38	1.46	1.41

The morphological characterization was performed using AFM NX-10, presented in Section (5.3.2), and the Zeiss microscope, described in Section (5.3.1). A first attempt to depict the morphology of the coating surface was made by using the atomic force microscope (AFM) and in Figure (6.29) the result is shown. The post-processing made obvious the high irregularity of the coating surface, yielding an RMS value of about 1.31μm.

 Given the big variations on the morphology of the surface, a better overview was provided by the optical microscope. The images of the surfaces of the samples were acquired with the Zeiss optical microscope (50x/0.75 and 100x/0.8) at different focus depths and they are displayed in Figure (6.31), Figure (6.32), Figure (6.33) and Figure (6.34). The images are eight for each sample (four for each magnification power): for the sample V95-3F with the optimized coating and no Celgard layer on top and the sample S90-3F with the optimized coating
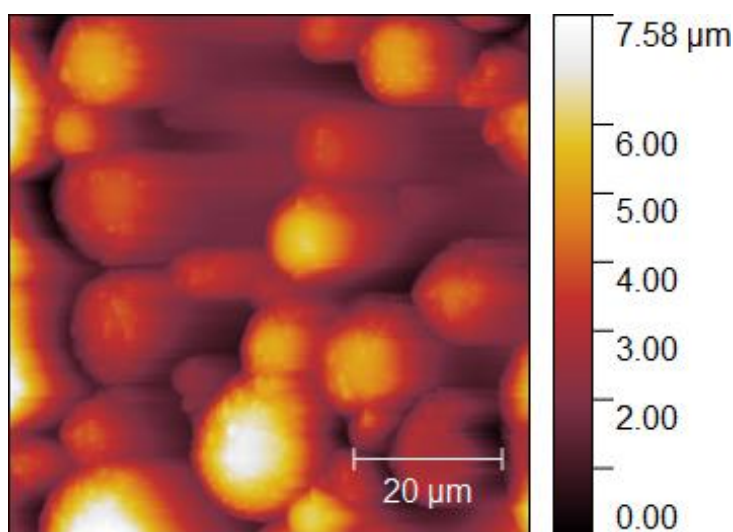
Figure 6.29: Surface topography measured by AFM.

and no Celgard layer on top.

Finally, an image of the sample V95-3F-1C was taken and it is reported in Figure (6.30). One can observe that different features of the sample come to focus at different depth levels, this is related to the different sizes of the silica microparticles and to the non-uniform nature of the coating possibly linked to the deposition technique used to apply the coating.

Figure 6.30: Morphology of sample V95-3F-1C acquired with Zeiss optical microscope at focus depth of 50x/0.75.

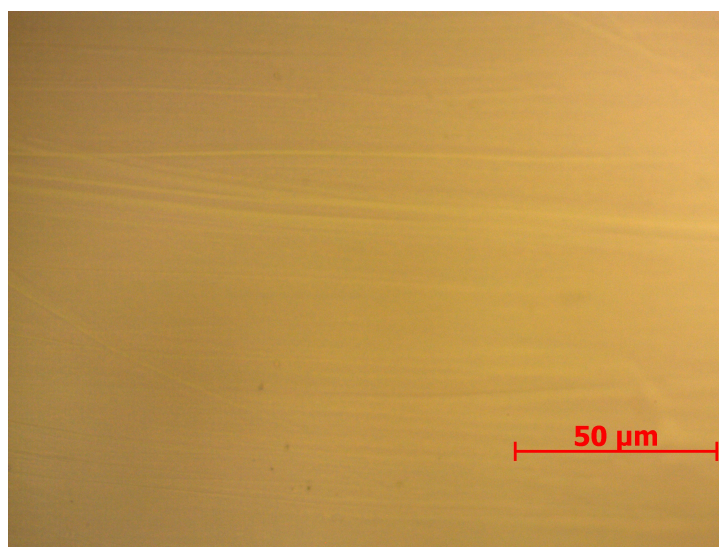Figure 6.31: Morphology of sample V95-3F acquired with Zeiss optical microscope at focus depth of 50x/0.75.

Figure 6.32: Morphology of sample V95-3F acquired with Zeiss optical microscope at focus depth of 100x/0.8.
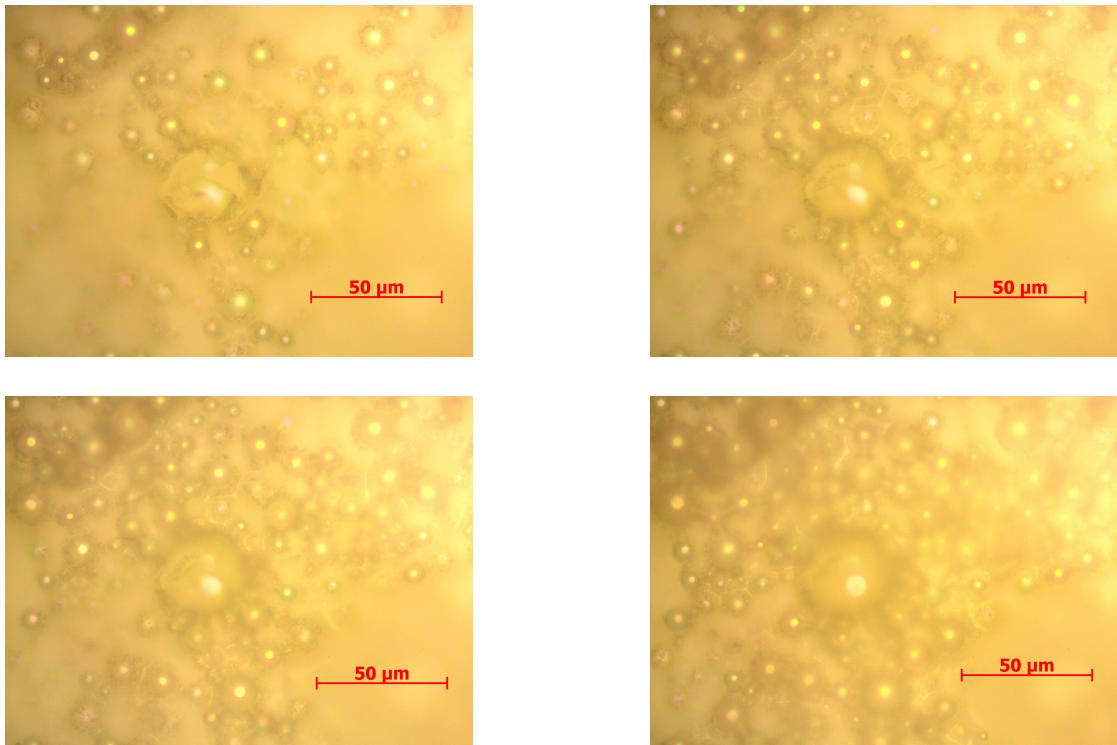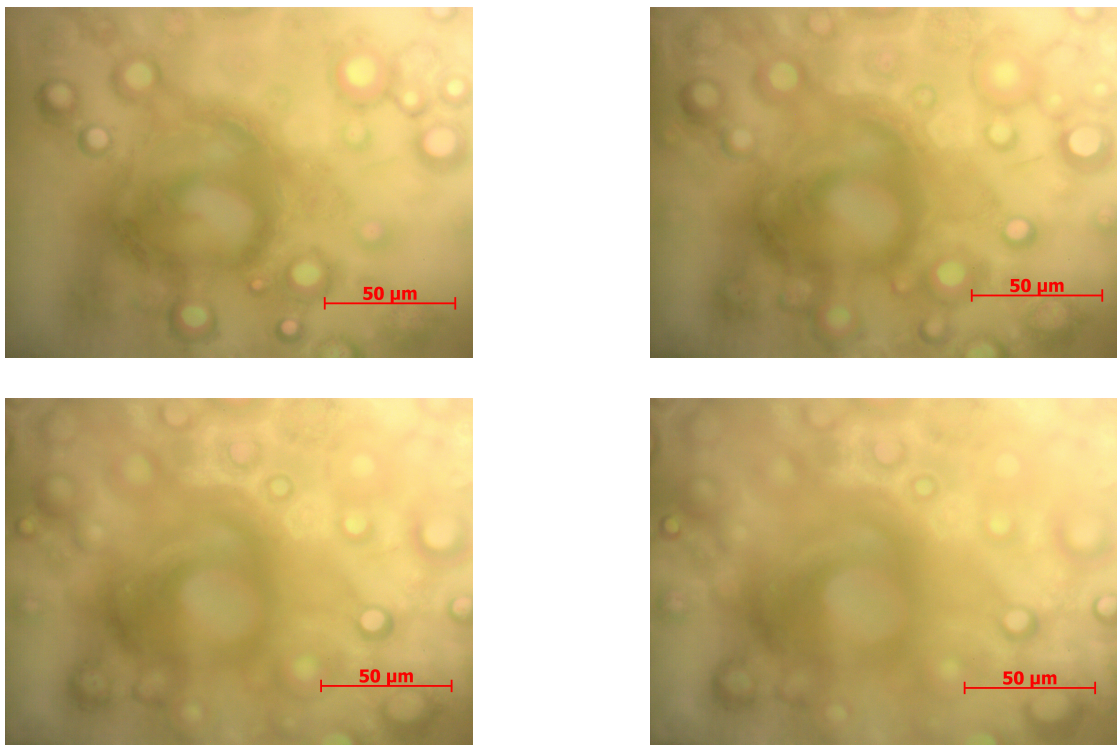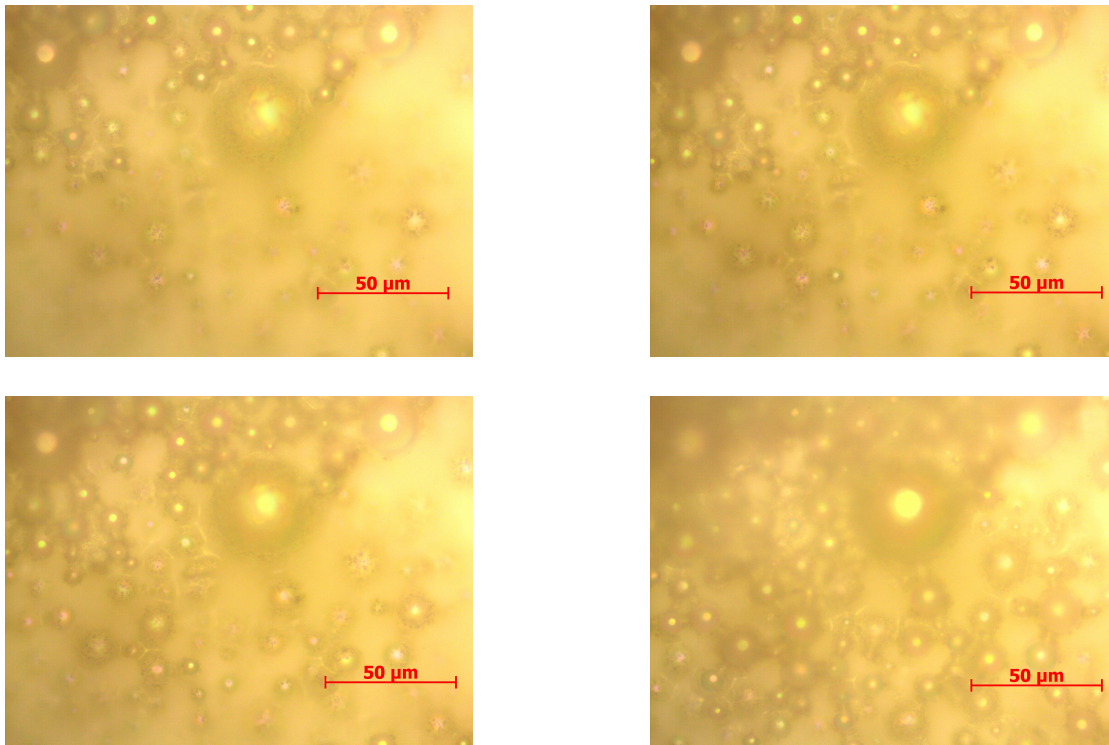
Figure 6.33: Morphology of sample S90-3F acquired with Zeiss optical microscope at focus depth of 50x/0.75.
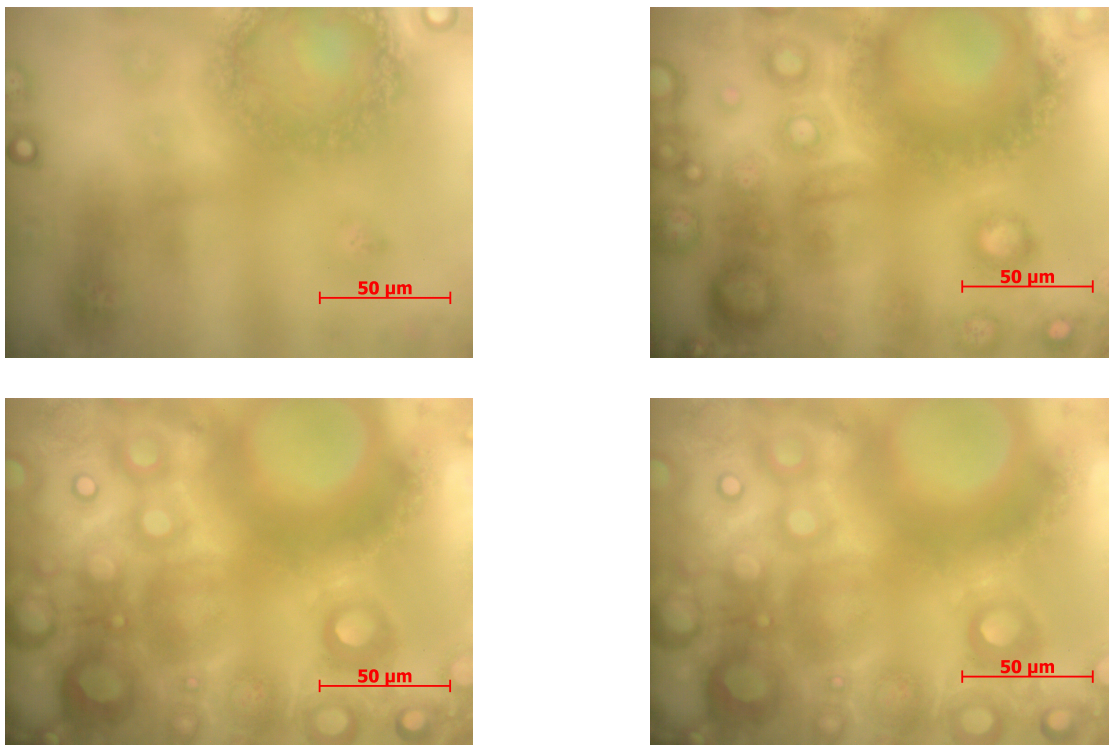

Figure 6.34: Morphology of sample S90-3F acquired with Zeiss optical microscope at focus depth of 100x/0.8.

6.3 EXPERIMENTAL MEASUREMENTS FOR COOLING PERFORMANCES

As previously mentioned, thanks to the preliminar optical characterization and analysis, the samples with better optical performances in terms of reflectance get selected. The samples belonging to the second set, reported in Table (5.3), are the ones that will be subject to the outdoor experiments.

Figure (6.35) presents the measurements collected over three consecutive days using the setup shown in Figure (5.11).

Figure (6.35.a) displays the ambient temperature T_{amb} measured by the Stevenson Shield, alongside with the temperature of the sample shielded by the NPF (S1 configuration), of the sample with NPF as the top layer (S2 configuration), of the air gap below S1, labeled as *U.S1* and below S2, labeled *U.S2*, and of the gap between the EPS lid and the EPS base block (TLid).

Figure (6.35.b) illustrates the environmental data, including relative humidity, solar irradiance, and the temperature of the sky T_{sky}.

Figure (6.35.c) shows, on the left axis, the temperature differences ΔT for configurations S1 and S2, while Figure (6.35.d) shows the ΔT values for U.S1, U.S2, and under the lid, all calculated relative to the external ambient temperature T_{amb}. The right axis in these plots corresponds to solar irradiance. The plot shows that sub-ambient temperatures for S1 and S2 are achieved when solar irradiance falls below 600W/m^2, while the sensors below the samples reach this condition only below 430W/m^2.

Let's notice that, during peak irradiance, the S1 configuration reaches a significantly higher temperatures than the S2, where the NPF is directly applied to the paint.

Figure (6.35.e) tracks sample temperatures during P_{cool} measurements, while Figure (6.35.f) shows the net cooling power for both configurations. Despite the lower nighttime temperatures in the enclosed setup, its corresponding cooling power is also slightly lower due to the better heat retention within the enclosed air pocket. When the sky temperature T_{sky} decreases below 5°C, cooling power is found to exceed 100W/m^2. An overview of the data can be obtained from the violin plots reported in Figure (6.36). The ΔT of the enclosed (S1) and open (S2) configurations are represented and compared in Figure (6.36.a), with reference to morning (from 5am to 11am), midday (from 11am to 5pm), afternoon (from
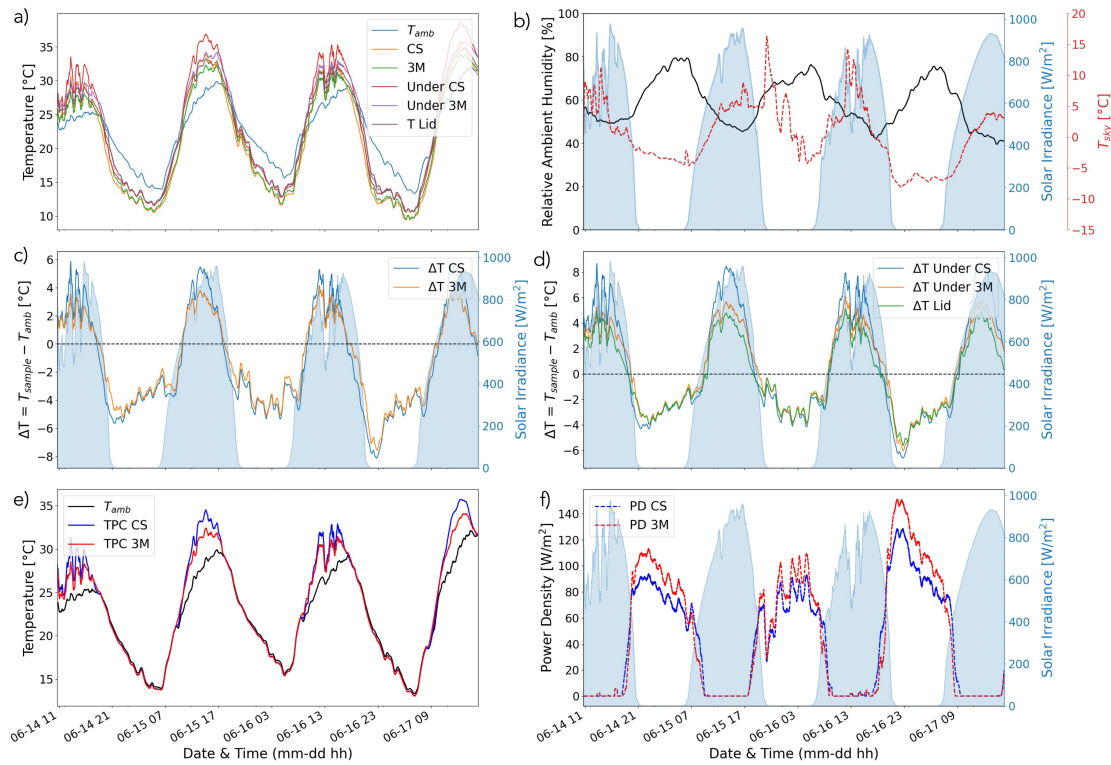
Figure 6.35: a) Ambient temperature and sample temperatures for the enclosed (S1) and open (S2) conditions, including temperatures under both samples and the lid that covers the EPS sample holder. b) Relative ambient humidity, solar irradiance, and sky temperature as a proxy to the presence of clouds. c) Temperature difference ΔT calculated as the difference between the S1 and S2 temperature and ambient. d) Temperature difference ΔT calculated as the difference between the temperature under S1, S2 and lid and ambient. e) Sample temperature for enclosed and open conditions monitored during the P_{cool} measurement, using external ambient temperature as the set point; f) Net cooling power measured for both configurations.

5pm to 11pm), and night (from 11pm to 5am) hours.

As one can note, in all the periods except midday, the two configurations show similar behavior, with a larger spread of ΔT during the afternoon. At midday, the two configurations show the most significant ΔT, yet with a different spread. Within this time window, the S1 (enclosed) sample experiences overheating peaks up to 6°C above ambient temperature, more than 2°C larger than the S2 (open) configuration. Similar conclusions can be drawn from the temperature difference ΔT U.S1 (enclosed) and U.S2 (open) measured below the samples and represented in Figure (6.36.b). In particular, a temperature difference peak of more than 8°C is reached at midday for U.S1 (enclosed), which is more than 3°C

larger than that the maximum U.S2 (open) reading.

In conclusion, the median temperature for each configuration over the three
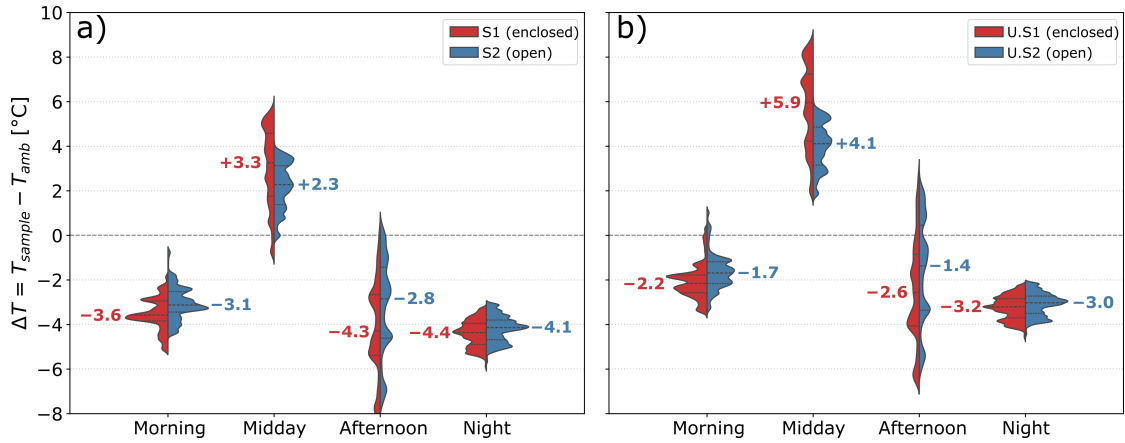
Figure 6.36: Split violin plot comparing the temperature difference ΔT for the following conditions: a) enclosed (S1) versus open (S2) sample and b) under the S1 and S2 samples. The values reported next to each distribution represent the median calculated for each time window over the three-day observation period.

days of measurements is reported in the violin plots (Figure (6.36)) showing the marked difference observed during the day, and the opposite trend registered in the evening, where the cooled air pocket helps maintaining a sub-ambient temperature in the enclosed configuration.

7

Conclusions

The focus of this master thesis revolves around the potential of passive daytime radiative cooling, being a key contributor to the opening of a path towards a greener future. Its various sustainable applications have the power to significantly reduce the overall environmental impact, namely aiding in heat dissipation, which is becoming a deeply critical problem due to the increasing energy demands.

The solution proposed in this work has the non-trivial feature of being a cost-effective solution, addressing one of the most challenging characteristics faced by the previous radiative cooling structures. In fact, in the recent years lots of different designs were proposed, but many of them did lack of scalability and affordability. Hence, this work tries to build a bridge between offering a scalable and viable solution.

The characterized samples have been fabricated with commercially available products: low-VOCs paint, SiO_2 microparticles and a thin PP-PE-PP layer. Moreover, thanks to the use of a water-based paint formulation, the resulting coatings has zero VOCs emissions, according to the European Union regulations about the target to reduce the amount of VOCs in paint coatings. Hence, apart from being a cost-effective solution, this RC architecture being based on a photonic disordered material, yields a lower environmental impact with respect to other paints that are solvent-based.

The results obtained in this work state that the PDRC coating, realized starting from an Al substrate and depositing three hands of paint on top, reaches a solar weighted reflectance of 94%. Moreover, the inclusion of an IR transparent thin

foil of PP-PE-PP was game-changing: enhancing the reflecting performances not absorbing a big part of the UV region of the solar spectrum, protecting the coating from degradation and contamination and offering the benefits of a convection shield.

The temperature drop achieved by the proposed structure is of about $-3°C$ in daytime hours, whereas during nighttime the maximum temperature drop reaches $-7°C$. An higher cooling power is achieved by the sample with the NPF deposited on top, the net cooling power is of about 140W m^{-2}.

Extra care must be addressed for the measurement of the cooling performances of the PDRC samples. In fact, the main downside of the usage of an NPF acting as convective shield can cause an overestimation of the temperature drop of the RC architecture, introducing a systematic bias in the calculation of the ambient temperature set point.

As a conclusion to this master thesis, I hope this project was able to successfully highlight the significance of this technology, which has the potential to transform the global energy consumption and serve a key stepping stone towards a greener future.

Appendix

Time independent Schrödinger equation (2.2)

Starting from the general form of the *Schrödinger equation*

$$-\frac{\hbar^2}{2m}\nabla^2\Psi(\vec{r},t) + \mathbf{V}(\vec{r},t)\cdot\Psi(\vec{r},t) = -j\hbar\frac{\partial\Psi(\vec{r},t)}{\partial t} \tag{7.1}$$

let's consider a time independent potential $\mathbf{V}(\vec{r},t) = \mathbf{V}(\vec{r})$, then by exploiting variable separation, $\Psi(\vec{r},t) = \psi(\vec{r})\cdot f(t)$, then

$$\frac{1}{\psi(\vec{r})}\left(-\frac{\hbar^2}{2m}\nabla^2 + \mathbf{V}(\vec{r})\right)\cdot\psi(\vec{r}) = \frac{j\hbar}{f(t)}\frac{\partial f(t)}{\partial t} \tag{7.2}$$

let's define the right term of the equation E the total energy of the non-relativistic particle, finally obtaining

$$-\frac{\hbar^2}{2m}\nabla^2\psi(\vec{r}) + \mathbf{V}(\vec{r})\cdot\psi(\vec{r}) = E\cdot\psi(\vec{r}) \tag{7.3}$$

Density of Modes for a 3D resonant cavity (2.19)

For a calculating the spectral energy density of the blackbody, i.e. the energy per unit of volume per unit of frequency, one has to consider the blackbody as a cavity [10], [7]. The radiation inside it reflects on its walls interfering, establishing a three dimensional stationary wave

$$E = E_0 sin(k_1 x)sin(k_2 y)sin(k_3 z)cos(\omega t) \tag{7.4}$$

therefore the cavity is a resonant one, which will be assumed to be a cube for considering the most generic case. Hence, let's consider three pairs of parallel

mirrors forming a cube of dimension $d_x = d_y = d_z = d$ in the *k-space*, therefore its nodes are in positions

$$k_x = q_x \frac{\pi}{d} \qquad\qquad k_y = q_y \frac{\pi}{d} \qquad\qquad k_z = q_z \frac{\pi}{d} \qquad (7.5)$$

with q_x, q_y and q_z equal to $1, 2, \dots$ the mode number.

Since k_x, k_y and k_z are defined as positive and knowing that $k^2 = k_x^2 + k_y^2 + k_z^2 = \left(\frac{2\pi\nu}{c}\right)^2$, let's consider in the *k-space*, as surface of constant frequency, the positive octante of a sphere of radius $k = 2\pi\nu/c$ and volume

$$V = \frac{1}{8}\left(\frac{4}{3}\pi k^3\right) \qquad (7.6)$$

Therefore the resenonance frequencies are $\nu_q = \sqrt{q_x^2 \nu_{Fx}^2 + q_y^2 \nu_{Fy}^2 + q_z^2 \nu_{Fz}^2}$ where $\nu_{Fi} = c/2nd_i$ wit $i = x, y, z$ the frequency spacings.

If $d \gg \lambda$ the exact number of modes is difficult to enumerate, then a continuous approximation is performed introducing the *density of modes* which states that the number of modes in a frequency interval $\Delta\nu$ is equal to the number of points in the positive octante of the sphere in the *k-space*, mathematically

$$2\left(\frac{1}{8}\right)\left(\frac{4}{3}\pi k^3\right) / (\pi/d)^3 = \left(\frac{k^3}{3\pi^2}\right) d^3 \qquad (7.7)$$

then between ν and $\nu + \Delta\nu$, the left term is

$$\frac{d}{d\nu}\left(\frac{8\pi\nu^3}{3c^3} d^3\right)\Delta\nu = \frac{8\pi\nu^2}{c^3} d^3 \Delta\nu \qquad (7.8)$$

hence the number of modes per unit of volume per unit of bandwidth surrounding ν is

$$M(\nu) = \frac{8\pi\nu^2}{c^3} \qquad (7.9)$$

References

[1] International Energy Agency. *World Energy Outlook 2023*. Paris: IEA, 2023. URL: https://www.iea.org/reports/world-energy-outlook-2023.

[2] Pengfei Liu et al. "Functional radiative cooling: basic concepts, materials, and best practices in measurements". In: *ACS Applied Electronic Materials* 5.11 (2023), pp. 5755–5776.

[3] Morna Isaac and Detlef P. van Vuuren. "Modeling global residential sector energy demand for heating and air conditioning in the context of climate change". In: *Energy Policy* 37.2 (2009), pp. 507–521. URL: https://www.sciencedirect.com/science/article/pii/S0301421508005168.

[4] Dongliang Zhao et al. "Radiative sky cooling: Fundamental principles, materials, and applications". In: *Applied Physics Reviews* 6.2 (2019), p. 021306.

[5] IEA (International Energy Agency). *Electricity Market Report*. https://www.iea.org/reports/electricity-market-report-2023. 2023.

[6] Xing Lu et al. "Cooling potential and applications prospects of passive radiative cooling in buildings: The current state-of-the-art". In: *Renewable and Sustainable Energy Reviews* 65 (2016), pp. 1079–1097.

[7] Bahaa EA Saleh and Malvin Carl Teich. *Fundamentals of photonics*. john Wiley & sons, 2019.

[8] Paul Anthony Cox. *Introduction to quantum theory and atomic structure*. Oxford University Press, 1996.

[9] Maria-Guglielmina Pelizzo. *Molecular Photonics: Lecture notes*. Università degli Studi di Padova. 2022.

[10] Pierluigi Zotto, Sergio Lo Russo, and Paolo Sartori. *Fisica Generale. Elettromagnetismo-Ottica*. Società Editrice Esculapio, 2022.

[11] Meg Noah. *Blackbody Radiance Calculations.* `https://www.mathworks.com/matlabcentral/fileexchange/69520-blackbody-radiance-calculations`. 2024.

[12] Luca Schenato. *Visible Light and Metasurfaces Communication: Lecture notes.* Università degli Studi di Padova. 2022.

[13] Pierluigi Zotto, Sergio Lo Russo, and Paolo Sartori. *Fisica Generale. Meccanica e Termodinamica.* Società Editrice Esculapio, 2022.

[14] C Balaji. *Essentials of radiation heat transfer.* Springer, 2014.

[15] Marco Santagiustina. *Nanophotonics: Lecture notes.* Università degli Studi di Padova. 2022.

[16] John R Howell et al. *Thermal radiation heat transfer.* CRC press, 2020.

[17] S. D. Lord. *IR Spectral Transmission of the Earth's Atmosphere from Gemini Observatory in Mauna Kea.* Tech. rep. NASA Technical Memorandum 103957. National Aeronautics and Space Administration, 1992. URL: `https://www.gemini.edu/observing/telescopes-and-sites/sites#Transmission`.

[18] Dongliang Zhao et al. "Radiative sky cooling: Fundamental principles, materials, and applications". In: *Applied Physics Reviews* 6.2 (Apr. 2019), p. 021306.

[19] Jyotirmoy Mandal et al. "Radiative cooling and thermoregulation in the earth's glow". In: *Cell Reports Physical Science* 5.7 (2024).

[20] ASTM International. *Standard Tables for Reference Solar Spectral Irradiances: Direct Normal and Hemispherical on 37° Tilted Surface.* `https://www.astm.org/g0173-23.html`. 2023.

[21] Antonio Gagliano et al. "A procedure for the characterization of the solar-weighted reflectance of mirrored reflectors". In: *IREC 2014 - 5th International Renewable Energy Congress* (Mar. 2014), pp. 1–6.

[22] T. S. Eriksson and C. G. Granqvist. "Radiative cooling computed for model atmospheres". In: *Appl. Opt.* 21.23 (1982), pp. 4381–4388.

[23] David Bainbridge and Ken Haggard. *Passive solar architecture: heating, cooling, ventilation, daylighting and more using natural flows.* Chelsea green publishing, 2011.

[24] Alan K Head. *Method and means for producing refrigeration by selective radiation.* US Patent 3,043,112. 1962.

[25] Junyu Sun et al. "Daytime passive radiative cooling materials based on disordered media: A review". In: *Solar Energy Materials and Solar Cells* 236 (2022), p. 111492.

[26] Aaswath P Raman et al. "Passive radiative cooling below ambient air temperature under direct sunlight". In: *Nature* 515.7528 (2014), pp. 540–544.

[27] Cunhai Wang, Hao Chen, and Fuqiang Wang. "Passive daytime radiative cooling materials toward real-world applications". In: *Progress in Materials Science* (2024), p. 101276.

[28] Meijie Chen et al. "Passive daytime radiative cooling: Fundamentals, material designs, and applications". In: *EcoMat* 4.1 (2022), e12153.

[29] Gil Ju Lee et al. "Colored, daytime radiative coolers with thin-film resonators for aesthetic purposes". In: *Advanced Optical Materials* 6.22 (2018), p. 1800707.

[30] Saichao Dang, Xiaojia Wang, and Hong Ye. "An ultrathin transparent radiative cooling photonic structure with a high NIR reflection". In: *Advanced Materials Interfaces* 9.30 (2022), p. 2201050.

[31] Kechao Tang et al. "Temperature-adaptive radiative coating for all-season household thermal regulation". In: *Science* 374.6574 (2021), pp. 1504–1509.

[32] Xiaojie Liu et al. "Continuously variable emission for mechanical deformation induced radiative cooling". In: *Communications Materials* 1.1 (2020), p. 95.

[33] Zhen Tong et al. "Atomistic metrics of BaSO _4 as an ultra-efficient radiative cooling material: a first-principles prediction". In: *arXiv preprint arXiv:2101.05053* (2021).

[34] Pengli Li et al. "Thermo-optically designed scalable photonic films with high thermal conductivity for subambient and above-ambient radiative cooling". In: *Advanced Functional Materials* 32.5 (2022), p. 2109542.

[35] Angus R Gentle and Geoffrey B Smith. "Radiative heat pumping from the earth using surface phonon resonant nanoparticles". In: *Nano letters* 10.2 (2010), pp. 373–379.

[36] William H Streyer. "Reststrahlen band optics for the advancement of far-infrared optical architecture". PhD thesis. University of Illinois at Urbana-Champaign, 2016.

[37] Jyotirmoy Mandal et al. "Hierarchically porous polymer coatings for highly efficient passive daytime radiative cooling". In: *Science* 362.6412 (2018), pp. 315–319. DOI: `10.1126/science.aat9513`. URL: `https://www.science.org/doi/abs/10.1126/science.aat9513`.

[38] Giuseppe Emanuele Lio et al. "Radiative Cooling Potential of a Water-Based Paint Formulation under Realistic Application Conditions". In: *ACS Applied Optical Materials* (2024).

[39] A Aili et al. "Selection of polymers with functional groups for daytime radiative cooling". In: *Materials Today Physics* 10 (2019), p. 100127.

[40] Wenlong Huang et al. "Scalable aqueous processing-based passive daytime radiative cooling coatings". In: *Advanced Functional Materials* 31.19 (2021), p. 2010334.

[41] Jaeman Song et al. "Ultrahigh emissivity of grating-patterned PDMS film from 8 to 13 μm wavelength regime". In: *Applied Physics Letters* 117.9 (2020).

[42] Xiao Nie et al. "Cool white polymer coatings based on glass bubbles for buildings". In: *Scientific reports* 10.1 (2020), p. 6661.

[43] Jianrong Song et al. "The effects of particle size distribution on the optical properties of titanium dioxide rutile pigments and their applications in cool non-white coatings". In: *Solar energy materials and solar cells* 130 (2014), pp. 42–50.

[44] *ThermoShield Paint datasheet*. `https://img1.wsimg.com/blobby/go/0a057b5a-cb5c-4931-aafe-4d5394f11f27/downloads/TB-TS-Exterieur.pdf?ver=1705925819259`.

[45] 3M Advanced Materials Division. *3M Glass Bubbles iM30K datasheet*. `https://www.3m.com/3M/en_US/p/d/b40064617/`.

[46] 3M Advanced Materials Division. *3M Glass Bubbles iM16K datasheet*. `https://multimedia.3m.com/mws/media/7884870/3m-glass-bubbles-im16k.pdf`.

[47] POLYPORE Company. *Celgard C210*. `http://sinerosz.com/product-50.html`.

[48]   *UV-VIS-NIR Cary 4000, 5000, 6000i Spectrophotometers: Preliminary Performance Data*. URL: https://www.science.unitn.it/~semicon/members/pavesi/Technical%20Spec_87-1942.pdf.

[49]   Kunlang Bu et al. "Consistent assessment of the cooling performance of radiative cooling materials". In: *Advanced Functional Materials* 33.51 (2023), p. 2307191.

[50]   Agilent. *Agilent Cary 4000/5000/6000i Series, UV-VIS-NIR Spectrophotometers*. 2022. URL: https://www.agilent.com/cs/library/brochures/5990-7786EN_Cary-4000-5000-6000i-UV-Vis-NIR_Brochure.pdf.

[51]   Molecular Materials Resource Center (MMRC) of California Institute of Technology. *User Guide for Cary 5000 spectrometer with external DRA 1800 attachment*. 2021. URL: https://mmrc.caltech.edu/Cary%20UV-Vis%20Int.Sphere/manuals/Cary5000_User_Guide.pdf.

[52]   Francis M. Mirabella Jr. "Strength of interaction and penetration of infrared radiation for polymer films in internal reflection spectroscopy". In: *Journal of Polymer Science: Polymer Physics Edition* 21.11 (1983), pp. 2403–2417.

[53]   Kermit S Kwan. "The role of penetrant structure in the transport and mechanical properties of a thermoset adhesive". PhD thesis. Virginia Polytechnic Institute and State University, 1998.

[54]   Park Systems. *Park AFM NX10*. URL: https://www.parksystems.com/en/products/research-afm/small-sample-afm/nx10?utm_source=google&utm_medium=cpc&utm_campaign=smallafm-eu-0923&utm_content=nx10&gad_source=1&gclid=Cj0KCQjwrp-3BhDgARIsAEWJ6SwyDh2x5AE_F-2AT78C19ANjo084xQJ0M0paBQgc1MZAXb8F7tfCcQaAoP-EALw_wcB.

[55]   Tewa temperature Sensors Ltd. *Negative Temperature Coefficient (NTC) thermistors, model: 103JT-025. DataSheet*. https://www.tme.eu/Document/85c74588be813b44821ab28dae36c629/TT6-10KC8-9-25.pdf.

[56]   Max Detect Technology Co. *DHT22 - Ambient temperature and relative humidity sensor - DataSheet*. http://cdn.sparkfun.com/datasheets/Sensors/Weather/RHT03.pdf.

[57]   Rohm Semiconductor. *BH1750 Light sensor DataSheet*. https://mm.digikey.com/Volume0/opasdata/d220001/medias/docus/6165/bh1750fvi-e.pdf.

[58] Melexis. *Melexis MLX90614 DataSheet*. `https://www.melexis.com/-/media/files/documents/datasheets/mlx90614-datasheet-melexis.pdf`.

[59] Davis Instruments. URL: `https://www.davisinstruments.com/products/radiation-shield`.

[60] Giuseppe Emanuele Lio. *FRESCO-Board*. 2024. URL: `https://github.com/GiuseppeELio/FRESCO-Board?tab=readme-ov-file`.

[61] *LaMMA Webpage*. `https://www.lamma.toscana.it/meteo/osservazioni-e-dati/dati-stazioni`.

[62] Janina Zieba-Palus. "The usefulness of infrared spectroscopy in examinations of adhesive tapes for forensic purposes". In: *Forensic Science and Criminology* 2 (Jan. 2017). DOI: `10.15761/FSC.1000112`.

Acknowledgments